

ABSTRACT

HU, ZUSHOU. Atomic Simulation of Nanoparticles and Polyethylene-Nanodiamond Composites. (Under the direction of Donald W. Brenner).

We examine the size and surface orientation/principal axis dependent stability of nanodiamonds and nanorods. We find that the nanodiamonds and nanorods are thermally stable at nanoscale; however, the (001) surface will tend to form dimers, and the (111) surface will buckify to reduce system energy when diameter is less than 2 nm. We also notice that the octahedra is the most stable morphology in all the carbon particles we studied, and the nanorods with the combination of $\langle 001 \rangle$ and (011), $\langle 011 \rangle$ and (111), and $\langle 011 \rangle$ and (001)/(111) are the stable nanorod structures. The MD simulation on glass transition and elastic properties of polyethylene-nanodiamond composites are also carried out in our studies. The results on glass transition show that the transition is a second order phase transition mainly associated with the change in torsional and non-bond interactions. The results on elastic properties indicate that the effect of nanoparticles on polymer composites is mainly determined by the equivalent time scale movement of nanoparticles and polymer chains, which can be improved by either equivalent size scale of nanoparticles and polymer chains or increasing interface interaction, such as chemical bonds at surface. The addition of nanoparticles usually increases the composite density; however, it doesn't necessarily increase the density of polymer matrix.

Atomic Simulation of Nanoparticles and Polyethylene-Nanodiamond Composites

by
Zushou Hu

A dissertation submitted to the Graduate Faculty of
North Carolina State University
in partial fulfillment of the
requirements for the degree of
Doctor of Philosophy

Materials Science and Engineering

Raleigh, North Carolina

2009

APPROVED BY:

Prof. Donald W. Brenner
Committee Chair

Prof. Maurice Balik

Prof. Ron O. Scattergood

Prof. Zhilin Li

DEDICATION

献给我的父母

和我的夫人杨海鸥

*To my parents,
and my wife Haiou Yang*

BIOGRAPHY

Zushou Hu was born in an honest farmer family having traditional rattan weaving on May 2nd, 1975 in Shichuan, a small village in Yongkang County, Zhejiang province, east of China. He was the naughtiest one in his family and spent almost all his childhood in the farm fields except the school time. After a family visit at his 8th grade, he began to study hard and developed his interest in science and mathematics. He entered Yongkang 1st High School in 1990, where he built solid background in mathematics and other science subjects. In 1993, he graduated for the second best from high school and was enrolled in the Department of Chemical Engineering at Tsinghua University for some reasons though he had the strong desire to study Electrical Engineering or Computer Science because he likes math, logic and reasoning. However, he kept to teach himself the subjects on psychology, mathematics, control theory and computer science besides his major. After graduation, he continued his study on systems engineering in the Department of Automation, obtaining his master degree in 2002 under the direction of professor Dazhong, Zheng. In the same year, he joined the Department of Chemical Engineering at the University of Tennessee at Knoxville and later transferred to North Carolina State University in 2003. He will get a Ph.D degree in Computational Materials Science with a minor in Mathematics at May 2009 and continue his post-doctoral research on Life Cycle Study at the Department of Chemical and Biomolecular Engineering at Georgia Institute of Technology.

Mr. Hu met his wife Haiou Yang at Tsinghua University and got married after they both graduated from their Master programs. They have two children, Yang Forest Hu (胡杨) and Hairui Harris Hu (胡海睿).

ACKNOWLEDGMENTS

I would like to express my gratitude to those who positively affected my life with their support, wisdom, love, and care.

I would like to thank my advisor Prof. Donald W. Brenner for his guidance, support and inspiration. His passion for the science and technology has fostered and fortified mine, which will be lasting for the rest of my life. I would like to thank my committee members, Prof. Ronald O. Scattergood, Prof. C. Maurice Balik and Prof Zhilin Li for their guidance and suggestion.

I would like to thank the members of the Computational Materials Science group members for their kindness, friendship, generous help, invaluable discussion, and the happy collaborative working environment they provided. Special thanks go to Olga Shenderova, Yanhong Hu, Douglas L. Irving and Cliff Padgett for their help in conducting some of the experiments included in this project. In addition, I wish to thank J. Wesley Crill to help me review my dissertation and Ms. Edna Deas for her help in administrative matters.

Finally, I would like to give my deep thanks to my close family members, my parents, my brothers and sisters, and my wife for their endless support, care, and unconditional love. A little special thank-you note should be given to my lovely sons, Yang Forest Hu and Hairui Harris Hu, who extend my life and expand my happiness.

TABLE OF CONTENTS

LIST OF TABLES	vii
LIST OF FIGURES	ix
CHAPTER 1. INTRODUCTION.....	1
1.1 NANODIAMONDS AND NANORODS	1
1.2 NANOCOMPOSITES	4
1.3 REFERENCES.....	11
CHAPTER 2. COMPUTATIONAL METHODS	17
2.1 REACTIVE EMPIRICAL BOND-ORDER (REBO) POTENTIAL.....	17
2.2 MOLECULAR DYNAMICS.....	20
2.3 LOCAL STRESS ANALYSIS	26
2.4 REFERENCES.....	28
CHAPTER 3. STABILITY OF NANODIAMONDS	30
3.1 INTRODUCTION.....	30
3.1.1 NANODIAMOND APPLICATION	31
3.1.2 CHARACTERIZATION AND STRUCTURE OF NANODIAMONDS	31
3.2 STABILITY OF NANODIAMONDS	32
3.3 SUMMARY	39
3.4 REFERENCES.....	40
CHAPTER 4. STABILITY OF NANORODS	48
4.1 INTRODUCTION.....	48
4.2 STABILITY OF NANORODS.....	50
4.3 SUMMARY	52
4.4 REFERENCES.....	53
CHAPTER 5. GLASS TRANSITION OF POLYETHYLENE-NANODIAMOND COMPOSITES	57
5.1 INTRODUCTION.....	57
5.1.1 SURVEY OF GLASS TRANSITION THEORY AND COMPUTATIONAL APPROACHES	58
5.1.2 MEASUREMENT OF FREE VOLUME	62
5.2 SIMULATION DETAILS AND SAMPLE PREPARATION	64
5.2.1 POTENTIALS	64
5.2.2 SAMPLE PREPARATION	68
5.2.3 SIMULATION DETAILS	71
5.3 RESULTS AND DISCUSSIONS	73
5.4 SUMMARY	82
5.5 REFERENCES.....	83
CHAPTER 6. ELASTIC PROPERTIES OF POLYETHYLENE-NANODIAMOND COMPOSITES.....	115
6.1 INTRODUCTION.....	115

6.2	SIMULATION DETAILS AND SAMPLE PREPARATION	118
6.2.1	POTENTIALS	118
6.2.2	SAMPLE PREPARATION	121
6.2.3	SIMULATION DETAILS	122
6.3	LINEAR ELASTIC STRESS-STRAIN RELATION.....	124
6.4	RESULTS AND DISCUSSIONS	128
6.5	SUMMARY	131
6.6	REFERENCES.....	132
CHAPTER 7. CONCLUSIONS AND FUTURE WORK.....		145

LIST OF TABLES

Table 5.1 Samples used in our studies	112
Table 5.2 Parameters obtained from fitting the specific volume v vs T (see Figure 5.6) for the NPT ensemble cooling data at 1 bar.	112
Table 5.3 Parameters obtained from fitting the specific volume v vs T (see Figure 5.7) for the NPT ensemble cooling data at 100 bar.	112
Table 5.4 Parameters obtained from fitting the specific volume v vs T (see Figure 5.8) for the NPT ensemble cooling data at 100 bar.	113
Table 5.5 Parameters obtained from fitting the specific volume v vs T (see Figure 5.9) for the NPT ensemble cooling data at 1bar.	113
Table 5.6 Parameters obtained from fitting the specific volume v vs T (see Figure 5.10) for the NPT ensemble cooling data at 1bar.	113
Table 5.7 Parameters obtained from fitting the specific volume v vs T (see Figure 5.11) for the NPT ensemble cooling data at 1bar.	114
Table 5.8 The effect of nanodiamond on the diffusion coefficient of long/short chain polymer at 600 K (unit: $10^{-9}m^2/s$).....	114
Table 6.1 Functional form and parameters for force field model of polyethylene and nanodiamond.....	142
Table 6.2 Characteristics of polyethylene chains in various nanocomposites and neat systems	143
Table 6.3 The Young's modulus (GPa) for the sample group containing 14 NDs and 97x40 polyethylene (SG-I).	143
Table 6.4 The Young's modulus (GPa) for the sample group containing 14 NDs and 97x200 polyethylene (SG-II).	143
Table 6.5 The Young's modulus (GPa) for the sample group containing 3 NDs and 97x40 polyethylene (SG-III).....	143

Table 6.6 The Young's modulus (GPa) for the sample group containing 14 NDs and 40x200 polyethylene (SG-IV).....	143
Table 6.7 Bulk densities of polyethylene in neat PE and in nanocomposites (g/cm ³).....	143
Table 6.8 Radius of gyration of polyethylene chains (unit Å)	144

LIST OF FIGURES

Figure 2.1 In the full expression the bonds are counted to the extent they cross the area of interest. Dark segments of bonds contribute; dotted segments do not.....	27
Figure 3.1 The Surface transformation of cubooctahedra to fullerence like structure	42
Figure 3.2 Representative structures from the set of ND morphologies simulated.....	42
Figure 3.3 Schematic diagram of dimers – top view and side view.	42
Figure 3.4 Number of under-coordinated surface atoms of different types for a spherical particle as a function of the number of atoms along the diameter.....	43
Figure 3.5 Histograms of atomic energies of carbon atoms for three octahedral particles (top) (C10H16 (N=2), C35H36 (N=3), C1330H400 (N=10)) and two cubo-octahedral particles (bottom) (C436H208 (N=8), C1550H432 (N=12)). Arrows from the bottoms of the pictures mark energies of carbon atoms in bulk diamond (-7.37eV) and at the (111) hydrogenated (-7.8 eV) and (100) 2x1 reconstructed (-7.5 for C2+1H, -7eV for C4-2d row and -6.9eV for the C4-3drow) macroscopic surfaces.	44
Figure 3.6 Cohesive energy from simulations with the bond-order potential (open symbols) and predicted analytically (solid symbols).	45
Figure 3.7 Heats of formation for hydrogenated octahedra and cubooctahedra.....	46
Figure 3.8 Heats of formation for hydrogenated octahedra, (001)2x1 reconstructed cubo-octahedra, spherical clusters and pentagonal clusters.....	47
Figure 4.1 Representative structures from the set of DNR morphologies simulated. The top structures correspond to $\langle 001 \rangle$ orientation along the DNR axis; the bottom structures correspond to $\langle 011 \rangle$ orientations. Surface orientations for the top structures, left to right: (011), (011), and (001), (001). Surface orientation for the bottom structures, left to right (011) and (001), (001) and (111), (111).....	55
Figure 4.2 Atomic enthalpy of formation versus the hydrogen-to-carbon ratio for DNRs of infinite length (via a periodic boundary) corresponding to the different morphologies represented in Figure 4.1.....	56
Figure 5.1 Individual chain model. The spherical “segment” simulates a CH ₂ or CH ₃ unit. A harmonic force constrains the bond length l around the equilibrium length l_0 . The bond angle θ is likewise constrained around the tetrahedral angle. The torsional	

angle ϕ , given by the angle between the plane containing segments $i-2$, $i-1$ and i and that contains segments $i-1$, i , and $i+1$, is subject to a threefold potential having *trans* and *gauche* minima. Segments separated by more than three bonds along the chain (for example $i-3$ and $i+1$), as well as segments which belong to different chains, interact according to a truncated Lennard-Jones potential. 85

Figure 5.2 Two dimensional illustration of a free volume calculation. 85

Figure 5.3 Composite samples at 1 bar and 600 K used in our studies (a) 12 NDs and 97x40 polyethylenes, (b) 6 NDs and 720x80 polyethylenes, (c) 12 NDs and 97x200 polyethylenes, and (d) 5 NDs 1440x40 polyethylenes. 86

Figure 5.4 Radial distribution function $g(r)$ for (a) system with 12 NDs and 97x200 polyethylene and (b) system with 12 NDs and 97x40 polyethylene. 87

Figure 5.5 Temperature tracking for cooling procedure – polyethylene-NDs systems without linkages between polyethylene and NDs. 88

Figure 5.6 Average unit cell volume versus dynamics temperature for isobaric cooling at atmospheric pressure (1 bar) for the sample with 12 NDs and 97x200 polyethylenes. The symbols represent the simulation data, the solid lines represent the best linear fits (see Table 5.2) and the long red lines are extrapolations of the high temperature solid lines to below the glass transition. The black lines indicate T_g for each system. 89

Figure 5.7 Average unit cell volume versus dynamics temperature for isobaric cooling at 100 bar for sample with 12 NDs and 97x200 polyethylenes. The symbols represent the simulation data, the solid lines represent the best linear fits (see Table 5.3) and the long red lines are extrapolations of the high temperature solid lines to below the glass transition. The black lines indicate T_g for each system. 90

Figure 5.8 Average unit cell volume versus dynamics temperature for isobaric cooling at 1 bar for the sample with 5 NDs and 720x80 polyethylenes. The symbols represent the simulation data, the solid lines represent the best linear fits (see Table 5.4) and the long red lines are extrapolations of the high temperature solid lines to below the glass transition. The black lines indicate T_g for each system. 91

Figure 5.9 Average unit cell volume versus dynamics temperature for isobaric cooling at 1 bar for the sample with 5 NDs and 1440x40 polyethylenes. The symbols represent the simulation data, the solid lines represent the best linear fits (see Table 5.5) and the long red lines are extrapolations of the high temperature solid lines to below the glass transition. The black lines indicate T_g for each system. 92

Figure 5.10 Average unit cell volume versus dynamics temperature for isobaric cooling at 100 bar for the sample with 6 NDs and 1440x40 polyethylenes. The symbols represent the simulation data, the solid lines represent the best linear fits (see Table 5.6) and the long red lines are extrapolations of the high temperature solid lines to below the glass transition. The black lines indicate T_g for each system.....	93
Figure 5.11 Average unit cell volume versus dynamics temperature for isobaric cooling at 1 bar for sample with 12 NDs and 97x40 polyethylenes. The symbols represent the simulation data, the solid lines represent the best linear fits (see Table 5.7) and the long red lines are extrapolations of the high temperature solid lines to below the glass transition. The black lines indicate T_g for each system.....	94
Figure 5.12 The relative size of nanodiamond and polymer chain.....	94
Figure 5.13 Pristine unit cell volume versus dynamics time	95
Figure 5.14 Standard deviation of the unit cell volume versus dynamics temperature for pure polyethylene.....	99
Figure 5.15 Standard deviation of the unit cell volume versus dynamics temperature for composites without crosslinks	100
Figure 5.16 Standard deviation of the unit cell volume versus dynamics temperature for composites with crosslinks	101
Figure 5.17 Compressibility versus temperature for pure sample with short/long chain.....	101
Figure 5.18 End-end distance versus dynamics temperature for the sample group with 12 NDs and 97x200 polyethylenes	102
Figure 5.19 Gyration radius for the sample group with 12 NDs and 97x200 polyethylenes	102
Figure 5.20 Plots of some energy components versus temperature for pure polyethylene: (a) bond energy; (b) angle energy; (c) torsion energy; (d) non-bond energy.....	103
Figure 5.21 Plots of some energy components versus temperature for composites without bonds: (a) bond energy; (b) angle energy; (c) torsion energy; (d) non-bond energy	104
Figure 5.22 Plots of some energy components versus temperature for composites with bonds: (a) bond energy; (b) angle energy; (c) torsion energy; (d) non-bond energy	105
Figure 5.23 The illustration of the transition state and the conformational state. Minimum of the energy curve is the T , G^+ , and G^- conformational state. The shaded domains are the transition state areas.....	106

Figure 5.24 The occurrences of transition versus temperature	106
Figure 5.25 Activation energy of torsional rotation.....	107
Figure 5.26 Available free volume in three samples at 1 bar.	108
Figure 5.27 Difference hole volume ΔV_{free} as a function of the temperature.	109
Figure 5.28 Number of cavities versus volume for composites w/o bonds at 100 bar and 600 K; (a) pure; (b) composites w/o bonds; (c) composite with bonds.	109
Figure 5.29 Snapshot of 1 nm slice of composites without bonds at 6 different temperatures.	110
Figure 5.30 Radial distribution function of CH ₂ units in a composite without crosslinks. ..	111
Figure 5.31 Mean square displacement versus temperature	111
Figure 6.1 Individual chain model. The spherical “segment” simulates a CH ₂ or CH ₃ unit. A harmonic force constrains the bond length l around the equilibrium length l_0 . The bond angle θ is likewise constrained around the tetrahedral angle. The torsional angle ϕ , given by the angle between the plane containing segments $i-2$, $i-1$ and i and that containing segments $i-1$, i , and $i+1$, is subject to a threefold potential having <i>trans</i> and <i>gauche</i> minima. Segments separated by more than three bonds along the chain (for example $i-3$ and $i+1$), as well as segments which belong to different chains, interact according to a truncated Lennard-Jones potential.	135
Figure 6.2 Periodic box of different neat and nanocomposite models (see Table 6.2) used in the simulations. Note the size of the box obtained after complete equilibration. (a) neat polyethylene; (b) composites w/o chemical bonds; (b) composites w/ chemical bonds.	136
Figure 6.3 Schematic diagram of deformed (dashed line) and un-deformed (solid line) shape of the unit showing unidirectional tension (NST approach).	137
Figure 6.4 In the full expression, the bonds are counted to the extent that they cross the area of interest. Dark segments of bonds contribute; dotted segments do not.	137
Figure 6.5 Measured tension ($-\sigma_{xx}$) as a function of percentage extension $\gamma_L \times 100$ for tension applied at 1 bar/ps under 100 K for the sample group containing 14 NDs and 97x40 polyethylene.	138

Figure 6.6 Measured tension ($-\sigma_{xx}$) as a function of percentage extension $\gamma_L \times 100$ for tension applied at 1 bar/ps under 100 K for the sample group containing 14 NDs and 97x200 polyethylene.....	138
Figure 6.7 Measured tension ($-\sigma_{xx}$) as a function of percentage extension $\gamma_L \times 100$ for tension applied at 1 bar/ps under 300 K for the sample group containing 14 NDs and 97x200 polyethylene.....	139
Figure 6.8 Free volume vs. external pressure for (a) SG-I and (b) SG-II at 300 K.....	139
Figure 6.9 Radial density distribution of various for (a) SG-I and (b) SG-III at 300 K and atmospheric pressure.....	140
Figure 6.10 PE-C radial distribution function (RDF) of (a) SG-I and (b) SG-III at 300 K and atmospheric pressure.....	140
Figure 6.11 The distribution of the local stress (σ_{11}) and the distribution of the local stress $\bar{\sigma}_{11}$ with respect to the distance r from the center of the NDs for the system 14 NDs and 40x200 polyethylene with crosslinks at 300 K and external stress a) 0 and b) 0.2 GPa.	141

CHAPTER 1. INTRODUCTION

1.1 NANODIAMONDS AND NANORODS

Nanoscale diamonds are widely existed in interstellar dusts and meteorites[1-4]. On earth, nanodiamonds can be produced by detonation[5]. These nanodiamonds are often called ‘Ultra Dispersed Diamond’ (UDD) because of their very narrow size distribution peaked, e.g. around ~4 nm. Recently nanodiamonds were synthesized by Chemical Vapor Deposition (CVD) techniques[6]. The characterization of nanodiamonds produced by detonation and CVD has revealed interesting, common features, nanodimensions (~4 nm), chemical stability of their core and activity of their peripheral shell.

The shape of ND particles is often assumed to be spherical based on transmission electron microscopy (TEM) pictures obtained without high enough magnification or without isolation of the nanoparticles from one another from the amorphous matrix. More comprehensive studies of HRTEM images revealed that ND particles rarely have a spherical shape[7]. The high-resolution transmission electron microscopy (HRTEM) images[7] also showed that the ND clusters consisted typically of regularly shaped cubo-octahedral and twinned crystals.

Each ND particle is coated by a shell of differently sp hybridized carbon atoms[8, 9] with a narrow size distribution in the region of ~ 4 nm, which was reported more once. The reason for this lies in that for such sizes it is the diamond rather than the graphite that turns

out a thermodynamically stable form of nano-carbon. This hypothesis was confirmed by ab initio modeling of the stable form of nanocrystalline diamond morphologies[10, 11]. However, as the size of diamond is reduced to about 3 nm, it is energetically favorable for this particle to have bare, reconstructed surface, such as the transformation to fullerene like structures. These suggested that the phase stability of carbon particle is size dependent.

Because of its extreme hardness, outstanding wear resistance, wide optical transparency, and other unique properties, nanodiamond has been used widely in many fields. The remarkable mechanical properties of NDs suggest immediately their application in abrasive materials or components of coatings[12-14]. The rich surface chemistry of NDs, the absence of toxic impurities and their small size make nanodiamonds very convenient for biomedical applications. By creating specific sites on NDs for selective molecular attachment, nanodiamond can be used for example in nanofabrication, self assembly, nanosensors, bioprobes, drug delivery, and pigments[15]. The typical diameter of NDs is about 5 nm, and about 10% of carbon atoms are at the surface. NDs can have significant π bonding which gives rise to unique electronic and magnetic features due to the lower energy gap of $\pi - \pi^*$ transitions relative to $\sigma - \sigma^*$ transitions. The investigation of field electrons from ND-based structures [16-18] has shown their potential for electrochemical electrodes and field emission structure, where high conductivities are required[17].

Diamond nanorod (DNR) is yet another one-dimensional carbon nanostructure. DNRs have been fabricated by several methods, including top-down approaches in which diamond films are etched[19, 20], bottom-up growth using CVD with templates[21, 22] and growth

without spatial confinement[23, 24]. The range of diameters of both polycrystalline and single-crystal DNRs span several tens of nanometers[25]. Their energetic stability compared to CNTs has been confirmed by both molecular modeling and first principle methods[26, 27].

Compared to the vast majority of research on another one-dimensional carbon nanostructure – nanotubes (CNTs), DNRs, which also hold promise for several important applications, are less studied. Aggregated DNRs have superior wear resistance[28], which is up to 300% in comparison with commercially available polycrystalline diamonds (PCDS). The relatively inert chemistry, the high mechanical strength and the high thermal conductivity of bulk diamond suggest that DNRs may find important applications as fillers in nanocomposites for structural and thermal management applications. DNRs may also be insulating, semi-metallic, or semiconducting depending on doping status, diameter, surface morphology and the degree of hydrogenation, suggesting that DNRs may have unique niche applications in nanoelectronics[29].

Though it is confirmed that the nanodiamonds and nanorods are energetically and mechanically viable structures at diameters about 4 nm, the studies by Barnard et al[10] showed that the stability was also dependent on both the surface morphology and the crystallographic direction of the principal axis of the nanowire. These studies have motivated a number of researchers to re-examine the phase stability of diamond at the nanometer scale. In our studies, we will expand the research on the stability of nanodiamonds and nanorods on the surface morphology and the crystallographic direction of the principal axis of the nanowire.

1.2 NANOCOMPOSITES

Over the past few decades, polymers have replaced many of the conventional metals/materials in various applications due to the advantages polymers offer over conventional materials, such as the ease of processing, productivity, and cost reduction. However, polymers have lower moduli and strengths compared to metals and ceramics. One way to improve their mechanical and thermal properties is to modify them using fillers, such as fibers, whiskers, platelets, or particles, to form polymer composites to get desirable materials properties not achieved by either phase alone or to reduce cost further. Actually, the idea of using filler as reinforcement is nothing new: straw has been used in China to reinforce mud bricks since about 4000 BC.

In conventional polymer composites, many inorganic types of filler with dimensions in the micrometer range, e.g. calcium carbonate, glass beads, clay and natural fibers, have been extensively used to enhance the mechanical properties of polymers[30, 31]. Such properties can be achieved by changing the volume fraction, shape and size of filler particle [3-5]. The success in the application of the Nylon6-clay hybrid developed by the research group in the Toyota Central Research and Development Laboratories, Inc., Japan in 1986 revealed the possibility of achieving remarkable improvements in thermal and mechanical properties of polymeric composites by incorporating a very low loading of nano clay filler[32]. This achievement attracted further investigations and revelations in polymer systems that contain dispersed nanoparticles, such as layered silicates, nano-CaCO₃ and carbon nanotubes, which represent a new class of materials with a combination of interesting

properties generally not obtainable in conventional polymer composites [4-7]. A big improvement, even at relatively low filler content, of the mechanical properties is achieved by using filler materials with a larger aspect ratio such as short glass fibers[4-6]. It is logical to anticipate that with a dispersion of fillers of nanometer-level dimensions, having larger aspect ratio and stiffness in a polymer matrix could lead to even higher mechanical performances. This leads to the pervasiveness of carbon nanotubes (CNTs), including single-wall and multi-wall nanotubes, in most areas of science and engineering due to their remarkable physical and mechanical properties[33-40].

Even though it has been shown that the CNTs have the potential to have excellent mechanical properties, the relatively high costs of development and manufacturing of nanotube/polymer composites has been prohibitive. An alternative way is the use of nanoparticles. Nanoparticles, sized between 1 and 100 nanometers, usually have a smaller aspect ratio than CNTs; they are also promising reinforcing and/or toughening materials for polymers. In the past few years, polymeric composites reinforced with nanoparticles, including Calcium carbonate (CaCO_3) and silica, have generated considerable attention among materials scientists and engineers due to their potential for superior physical, chemical, and mechanical properties in composite structures[12-14, 41-44]. These improvements, which are difficult to predict with current micromechanics theories, depend on a set of factors that include nanoparticle size, shape, volume fraction, degree of dispersion, nanofiller chemistry, characteristics of the polymer matrix, and interactions between filler and matrix at their interface[45]. The size and the shape are two important

contributions to the overall nanocomposite properties: surface-to-volume ratio of the fillers and excluded volume interactions. They are the heart of the ‘nano’ effect on mechanical properties in nanocomposites. The surface-to-volume ratio of the filler is the primary reason to develop nanocomposites because high interface region means high efficient transfer of stress across the composite components. The excluded volume interactions determine the dispersing of fillers in the polymer matrix. High-aspect ratio objects, such as long cylinders, are increasingly difficult to disperse isotropically as the aspect ratio, L/r , increases. One way to maximize the probability of isotropic dispersion is to modify the surface of the nanoscale filler to increase favorable interactions with polymer matrix and minimize inter-filler interactions, which also plays an important role in the efficiency of stress across the nanofiller/polymer interface.

Detonation nanodiamonds (NDs) were first synthesized by Russian scientists through the process of explosion-induced decomposition of highly explosive mixtures with a negative oxygen balance in a nonoxidizing atmosphere[12]. Research on the synthesis and applications of diamond nanoparticles has continued to the present. Nanodiamonds combine nano-dimensions (4-6 nm), chemical stability of their core and potential for chemical reactivity of their peripheral shell. The extremely hard core makes them an attractive additive to toughen polymers, and the chemical reactivity of the peripheral shell promotes the formation of cross-links to polymer chains during nanocomposite curing[12, 13, 42, 46]. These superior intrinsic properties make NDs particularly attractive for the fabrication of advanced materials and devices suited for critical applications. The addition of NDs to

structural polymers results in an increase in mechanical strength, wear-resistance, and head-aging resistance [12-14, 41, 42]. Highly effective coatings based on the incorporation of NDs in fluoroelastomers and polysiloxanes have been developed, and the elastic modulus and strength of rubbers based on poly-isoprene, butadiene-styrene, butadiene-nitrile, as well as natural rubbers, have been considerably improved[12, 13, 42]. Though remarkable efforts have been paid to polymer nanocomposites, and nanodiamonds are widely used in many fields, the research on diamond-filled polymer composites is still very limited [12, 13, 41, 42, 47].

Experimentally, it is challenging to make good samples of nanoparticles and polymer composites because of the chemical activity of nano-scale particles. A variety of methods[43, 48-52] have been tried to prepare nano-scale particles and to make polymer matrix nanocomposites. These include inert gas condensation, chemical vapor deposition, ball milling, sol-gel, and flame spraying. No universal technique for making polymer nanocomposites is available because of the physical and chemical differences between systems and equipment available to researchers. Each polymer system needs a special set of processing conditions, which are usually demanding and expensive, based on desired properties. In addition, current theories usually cannot correlate the experimental results with thermal and mechanics properties of nanocomposite systems. To this end, computer simulation, which allows for parametric studies of the influence of filler on material properties, has become a powerful tool to facilitate the development of nanocomposites. In particular, first-principles techniques[53], semi-empirical schemes[54], empirical potential

methods[35], and coarse graining models[55] have been applied successfully to study nanostructures. Especially for large systems with hundreds of atoms to millions of atoms or more, molecular dynamics is a powerful tool to understand the properties of polymer-nanoparticle composites at the atomic level, which greatly enhances the understanding realized from experiments.

In several earlier works, ab-initio[10], density-functional theory (DFT)[11, 27, 56], and Monte Carlo methods[57] have been successfully applied to predict the thermal stability of nanodiamonds (NDs), such as nanowires, bucky-diamonds, carbon-onions, and fullerenes, in various size regimes. This work has been further extended in our study to include four classes of nanodiamonds with different surface orientations and the size dependent thermal stability of cuboctahedral ND with a second-generation reactive empirical bond order (REBO) potential. The glass transition and strain-stress properties of nanocomposites containing polyethylene and the stable nanodiamonds were further studied. Glass transition phenomena in composites have been of paramount interest to polymer scientists[58-65]. However, no simulations have been performed to date on the composites containing polyhedral nanoparticles. Furthermore, the effects of polyhedral surfaces on the distribution of free volume and the behavior of nanoparticles during the glass transition have not been explored in previous simulation studies. In our study, we performed a series of molecular dynamics (MD) simulations in which samples with different polymer chain lengths and nanoparticle densities were cooled through T_g under atmospheric pressure to explore the effect of polymer chain length and nanoparticle density on the distribution of free

volume and particle movement. Mechanical properties are another interesting aspect of the new materials to polymer scientists[39, 44, 55, 66-70]. We computed stress-strain curves for a series of nanocomposites with different polymer chain lengths and nanoparticle densities conical (NPT) ensembles.

The remainder of this dissertation is organized as follows: In Chapter 2, we give a discussion of the second generation Reactive Empirical Bond Order (REBO) potential, molecular dynamics (MD) simulation, a description of algorithms used in our computation, and a description of free volume and local stress calculations. This background will be helpful to understand the following chapters. In Chapter 3, the heats of formation for octahedral, cuboctahedral and their sub-series with partially or fully restricted surface are investigated using second-generation REBO potentials[71]. In addition to cuboctahedral and octahedral clusters, the relative thermal stability of spherical particles and pentaparticles is also explored. To extend our studies on diamond clusters, the heats of formation for six different morphologies of diamond nanorods were examined. These simulations revealed the size dependent thermal stability of the carbon clusters. In Chapter 4, the heats of formation for nanorods with different principle axes and surface orientations are investigated using the second-generation REBO potential[71]. These simulations explored the size dependent thermal stability of six series of nanorods. In Chapter 5, glass transitions of polyethylene and corresponding nanocomposites containing cuboctahedral nanodiamonds with or without crosslinks at the interface are investigated. We also explore the distribution of free volume, the transition of torsional energy and VDW energy, and conformational transitions when

cooling the samples through the glass transition temperature T_g under isobaric conditions. Four groups of samples with different chain lengths and ND densities are examined. These simulations show the effect of nanoparticle, chain length and crosslinks on glass transition temperatures. In Chapter 6, NPT ensembles were used to investigate the stress-strain behavior of four groups of samples with different ND densities and polyethylene chain lengths within an NPT ensemble at 100 K and 300 K, respectively. Local stress and strain distributions were also calculated during the molecular dynamics under an applied unidirectional tensile strain. These simulations showed the effect of nanodiamond and the chemical bonds at the interface on elastic properties.

1.3 REFERENCES

1. Lewis, R.S., E. Anders, and B.T. Draine, *PROPERTIES, DETECTABILITY AND ORIGIN OF INTERSTELLAR DIAMONDS IN METEORITES*. Nature, 1989. **339**(6220): p. 117-121.
2. Lewis, R.S., et al., *INTERSTELLAR DIAMONDS IN METEORITES*. Nature, 1987. **326**(6109): p. 160-162.
3. Daulton, T.L., et al., *Genesis of presolar diamonds: Comparative high-resolution transmission electron microscopy study of meteoritic and terrestrial nano-diamonds*. Geochimica Et Cosmochimica Acta, 1996. **60**(23): p. 4853-4872.
4. Hill, H.G.M., A.P. Jones, and L.B. d'Hendecourt, *Diamonds in carbon-rich proto-planetary nebulae*. Astronomy & Astrophysics, 1998. **336**(3): p. L41-L44.
5. Volkov, K.V., V.V. Danilenko, and V.I. Elin, *SYNTHESIS OF DIAMOND FROM THE CARBON IN THE DETONATION PRODUCTS OF EXPLOSIVES*. Combustion Explosion and Shock Waves, 1990. **26**(3): p. 366-368.
6. Jiao, S., et al., *Microstructure of ultrananocrystalline diamond films grown by microwave Ar-CH₄ plasma chemical vapor deposition with or without added H₂*. Journal of Applied Physics, 2001. **90**(1): p. 118-122.
7. Kuznetsov, V.L., et al., *Theoretical study of the formation of closed curved graphite-like structures during annealing of diamond surface*. Journal of Applied Physics, 1999. **86**(2): p. 863-870.
8. Baidakova, M.V., V.I. Siklitsky, and A.Y. Vul, *Ultradisperse-diamond nanoclusters. Fractal structure and diamond-graphite phase transition*. Chaos Solitons & Fractals, 1999. **10**(12): p. 2153-2163.
9. Baidakova, M.V., et al., *Fractal structure of ultradisperse-diamond clusters*. Physics of the Solid State, 1998. **40**(4): p. 715-718.
10. Barnard, A.S., S.P. Russo, and I.K. Snook, *Ab initio modelling of the stability of nanocrystalline diamond morphologies*. Philosophical Magazine Letters, 2003. **83**(1): p. 39-45.
11. Barnard, A.S., S.P. Russo, and I.K. Snook, *First Principles Investigations of Diamond Ultrananocrystals*. International Journal of Modern Physics B: Condensed Matter Physics; Statistical Physics; Applied Physics, 2003. **17**(21): p. 3865.

12. Dolmatov, V.Y., *Polymer-diamond composites from detonation-derived nanodiamonds. Part 1*. Sverkhtverdye Materialy, 2007. **1**: p. 15.
13. Dolmatov, V.Y., *Polymer-diamond composites based on detonation nanodiamonds. Part 2*. Sverkhtverdye Materialy, 2007. **2**: p. 15.
14. Zhang, Q., et al., *Polyimide/Diamond nanocomposites: Microstructure and indentation Behavior*. Macromolecular Rapid Communications, 2007. **28**(21): p. 2069-2073.
15. Roy, R.R., *Biomedical applications of diamond-like carbon coatings: a review*. Journal of biomedical materials research. Part B, Applied biomaterials, 2007. **83B**(1): p. 72.
16. Okotrub, A.V., et al., *Field emission from products of nanodiamond annealing*. Carbon, 2004. **42**(5-6): p. 1099-1102.
17. Williams, O.A., *Ultrananocrystalline diamond for electronic applications*. Semiconductor Science and Technology, 2006. **21**(8): p. R49-R56.
18. Lee, Y.C., et al., *Synthesis and electron field emission properties of nanodiamond films*. Diamond and Related Materials, 2004. **13**(11-12): p. 2100-2104.
19. Baik, E.S., Y.J. Baik, and D. Jeon, *Aligned diamond nanowhiskers*. Journal of Materials Research, 2000. **15**(4): p. 923-926.
20. Zhang, W.J., et al., *Structuring nanodiamond cone arrays for improved field emission*. Applied Physics Letters, 2003. **83**(16): p. 3365-3367.
21. Yanagishita, T., et al., *Synthesis of diamond cylinders with triangular and square cross sections using anodic porous alumina templates*. Chemistry Letters, 2002(10): p. 976-977.
22. Masuda, H., et al., *Synthesis of well-aligned diamond nanocylinders*. Advanced Materials, 2001. **13**(4): p. 247-+.
23. Kobashi, K., et al., *Fibrous structures on diamond and carbon surfaces formed by hydrogen plasma under direct current bias and field electron-emission properties*. Journal of Materials Research, 2003. **18**(2): p. 305-326.
24. Chih, Y.K., et al., *Formation of nano-scale tubular structure of single crystal diamond*. Diamond and Related Materials, 2004. **13**(9): p. 1614-1617.
25. Dubrovinskaia, N., et al., *Aggregated diamond nanorods, the densest and least compressible form of carbon*. Applied Physics Letters, 2005. **87**(8): p. 3.

26. Shenderova, O.A., V.V. Zhirnov, and D.W. Brenner, *Carbon nanostructures*. Critical Reviews in Solid State and Materials Sciences, 2002. **27**(3-4): p. 227-356.
27. Barnard, A.S., *Structural properties of diamond nanowires: Theoretical predictions and experimental progress*. Reviews on Advanced Materials Science, 2004. **6**(2): p. 94-119.
28. Dubrovinskaia, N., S. Dub, and L. Dubrovinsky, *Superior wear resistance of aggregated diamond nanorods*. Nano Letters, 2006. **6**(4): p. 824-826.
29. Shenderova, O.A., D.M. Gruen, and Knovel. *Ultrananocrystalline diamond synthesis, properties, and applications*. 2006.
30. Powell, C.E. and G.W. Beall, *Physical properties of polymer/clay nanocomposites*. Current Opinion in Solid State & Materials Science, 2006. **10**(2): p. 73-80.
31. Schneider, J.P., et al., *BIOFIBRES AS REINFORCING FILLERS IN THERMOPLASTIC COMPOSITES*. Engineering Plastics, 1995. **8**(3): p. 207-222.
32. Kawasumi, M., *The discovery of polymer-clay hybrids*. Journal of Polymer Science Part a-Polymer Chemistry, 2004. **42**(4): p. 819-824.
33. Andrews, R. and M.C. Weisenberger, *Carbon nanotube polymer composites*. Current Opinion in Solid State & Materials Science, 2004. **8**(1): p. 31-37.
34. Dondero, W.E. and R.E. Gorga, *Morphological and mechanical properties of carbon nanotube/polymer composites via melt compounding*. Journal of Polymer Science Part B-Polymer Physics, 2006. **44**(5): p. 864-878.
35. Frankland, S.J.V., et al., *The stress-strain behavior of polymer-nanotube composites from molecular dynamics simulation*. Composites Science and Technology, 2003. **63**(11): p. 1655-1661.
36. Haggenueller, R., et al., *Aligned single-wall carbon nanotubes in composites by melt processing methods*. Chemical Physics Letters, 2000. **330**(3-4): p. 219-225.
37. Shenderova, O., D. Brenner, and R.S. Ruoff, *Would diamond nanorods be stronger than fullerene nanotubes?* Nano Letters, 2003. **3**(6): p. 805-809.
38. Wei, C.Y., D. Srivastava, and K.J. Cho, *Thermal expansion and diffusion coefficients of carbon nanotube-polymer composites*. Nano Letters, 2002. **2**(6): p. 647-650.
39. Yu, M.F., et al., *Tensile loading of ropes of single wall carbon nanotubes and their mechanical properties*. Physical Review Letters, 2000. **84**(24): p. 5552-5555.

40. Yu, M.F., et al., *Strength and breaking mechanism of multiwalled carbon nanotubes under tensile load*. Science, 2000. **287**(5453): p. 637-640.
41. Shenderova, O., et al., *Nanodiamond and onion-like carbon polymer nanocomposites*. Diamond and Related Materials, 2007. **16**(4-7): p. 1213-1217.
42. Dolmatov, V.Y., *Polymer-diamond composites based on detonation nanodiamonds. Report 3*. Sverkhтвердые Materialy, 2007. **4**: p. 10.
43. Chan, C.M., et al., *Polypropylene/calcium carbonate nanocomposites*. Polymer, 2002. **43**(10): p. 2981-2992.
44. Yang, K., et al., *Morphology and mechanical properties of polypropylene/calcium carbonate nanocomposites*. Materials Letters, 2006. **60**(6): p. 805-809.
45. Jordan, J., et al., *Experimental trends in polymer nanocomposites - a review*. Materials Science and Engineering a-Structural Materials Properties Microstructure and Processing, 2005. **393**(1-2): p. 1-11.
46. Hu, Y.H., et al., *Carbon nanostructures for advanced composites*. Reports on Progress in Physics, 2006. **69**(6): p. 1847-1895.
47. d'Almeida, J.R.M., et al., *Diamond-epoxy composites*. Journal of Reinforced Plastics and Composites, 2007. **26**(3): p. 321-330.
48. Vollenberg, P.H.T. and D. Heikens, *PARTICLE-SIZE DEPENDENCE OF THE YOUNG MODULUS OF FILLED POLYMERS .1. PRELIMINARY EXPERIMENTS*. Polymer, 1989. **30**(9): p. 1656-1662.
49. Petrovic, Z.S., et al., *Structure and properties of polyurethane-silica nanocomposites*. Journal of applied polymer science, 2000. **76**(2): p. 133-151.
50. Rong, M.Z., et al., *Structure-property relationships of irradiation grafted nano-inorganic particle filled polypropylene composites*. Polymer, 2001. **42**(1): p. 167-183.
51. Yang, F., Y.C. Ou, and Z.Z. Yu, *Polyamide 6 silica nanocomposites prepared by in situ polymerization*. Journal of applied polymer science, 1998. **69**(2): p. 355-361.
52. Ou, Y., F. Yang, and Z. Yu, *A New Conception on the Toughness of Nylon 6/Silica Nanocomposite Prepared via In Situ Polymerization*. Journal of Polymer Science Part B-Polymer Physics, 1998. **36**: p. 7.
53. Robertson, D.H., D.W. Brenner, and J.W. Mintmire, *ENERGETICS OF NANOSCALE GRAPHITIC TUBULES*. Physical Review B, 1992. **45**(21): p. 12592-12595.

54. Hernandez, E., et al., *Elastic properties of C and BxCyNz composite nanotubes*. Physical Review Letters, 1998. **80**(20): p. 4502-4505.
55. Oberdisse, J., et al., *Mechanical properties of end-crosslinked entangled polymer networks using sliplink Brownian dynamics simulations*. Rheologica Acta, 2006. **46**(1): p. 95-109.
56. Barnard, A.S., S.P. Russo, and I.K. Snook, *Size dependent phase stability of carbon nanoparticles: Nanodiamond versus fullerenes*. Journal of Chemical Physics, 2003. **118**(11): p. 5094-5097.
57. Barnard, A.S., et al., *A Monte Carlo Study of Surface Reconstruction in (100) and (111) Diamond Surfaces and Nanodiamond*. Molecular Simulation, 2004. **30**(1): p. 1-8.
58. Ash, B.J., L.S. Schadler, and R.W. Siegel, *Glass transition behavior of alumina/polymethylmethacrylate nanocomposites*. Materials Letters, 2002. **55**(1-2): p. 83-87.
59. Colucci, D.M., et al., *Isochoric and isobaric glass formation: Similarities and differences*. Journal of Polymer Science Part B-Polymer Physics, 1997. **35**(10): p. 1561-1573.
60. Fried, J.R. and P. Ren, *Molecular simulation of the glass transition of polyphosphazenes*. Computational and Theoretical Polymer Science, 1999. **9**(2): p. 111-116.
61. Liang, T.N., et al., *Conformational transition behavior around glass transition temperature*. Journal of Chemical Physics, 2000. **112**(4): p. 2016-2020.
62. Rigby, D. and R.J. Roe, *MOLECULAR-DYNAMICS SIMULATION OF POLYMER LIQUID AND GLASS .I. GLASS-TRANSITION*. Journal of Chemical Physics, 1987. **87**(12): p. 7285-7292.
63. Soldera, A., *Comparison between the glass transition temperatures of the two PMMA tacticities: A molecular dynamics simulation point of view*. Macromolecular Symposia, 1998. **133**: p. 21-32.
64. Sun, Y.Y., et al., *Glass transition and relaxation behavior of epoxy nanocomposites*. Journal of Polymer Science Part B-Polymer Physics, 2004. **42**(21): p. 3849-3858.
65. Yang, L., D.J. Srolovitz, and A.F. Yee, *Molecular dynamics study of isobaric and isochoric glass transitions in a model amorphous polymer*. Journal of Chemical Physics, 1999. **110**(14): p. 7058-7069.

66. Akovali, G. and M.A. Akman, *Mechanical properties of plasma surface-modified calcium carbonate-polypropylene composites*. Polymer International, 1997. **42**(2): p. 195-202.
67. Crosby, A.J. and J.Y. Lee, *Polymer nanocomposites: The "nano" effect on mechanical properties*. Polymer Reviews, 2007. **47**(2): p. 217-229.
68. Demczyk, B.G., et al., *Direct mechanical measurement of the tensile strength and elastic modulus of multiwalled carbon nanotubes*. Materials Science and Engineering a-Structural Materials Properties Microstructure and Processing, 2002. **334**(1-2): p. 173-178.
69. Unal, H., A. Mimaroglu, and M. Alkan, *Mechanical properties and morphology of nylon-6 hybrid composites*. Polymer International, 2004. **53**(1): p. 56-60.
70. Williams, M.L., R.F. Landel, and J.D. Ferry, *MECHANICAL PROPERTIES OF SUBSTANCES OF HIGH MOLECULAR WEIGHT .19. THE TEMPERATURE DEPENDENCE OF RELAXATION MECHANISMS IN AMORPHOUS POLYMERS AND OTHER GLASS-FORMING LIQUIDS*. Journal of the American Chemical Society, 1955. **77**(14): p. 3701-3707.
71. Brenner, D.W., et al., *A second-generation reactive empirical bond order (REBO) potential energy expression for hydrocarbons*. Journal of Physics-Condensed Matter, 2002. **14**(4): p. 783-802.

CHAPTER 2. COMPUTATIONAL METHODS

2.1 REACTIVE EMPIRICAL BOND-ORDER (REBO) POTENTIAL

Abell[1] firstly introduced the general analytic bond-order potential energy formalism, which states that the chemical binding energy U_b can be simply expressed as a sum over nearest neighbors:

$$U_b = \sum_i \sum_{j(>i)} [V_R(r_{ij}) - b_{ij}V_A(r_{ij})] \quad (2.1.1)$$

The function $V_R(r)$ and $V_A(r)$ are pair-additive terms that describe the interatomic repulsions and attractions, respectively. The term b_{ij} is bond-order term between atoms i and j . A practical implementation of Abell's bond-order formalism was first developed by Tersoff for group IV elements[2, 3]. By introducing analytic parameterized forms for the bond order term, the Tersoff potential can accurately treat silicon, germanium and their alloys, but is less reliable for carbon[4, 5].

Carbon is unique in that it forms a variety of different types of C-C bonds with different bond lengths and energies, which results in a large variety of polymorphic forms, such as graphite, nanotubes, fullerenes, diamond and various amorphous phases[6]. The Tersoff potential cannot deal properly with the processes involving a change of bonding characteristics, such as surface reconstruction and chemical reactions, because it doesn't distinguish the chemical character of the bond[4, 5]. This potential was further developed by

Brenner[7], under the name reactive empirical bond-order (REBO) potential, to describe solid-state carbon and hydrocarbon molecules. In this potential, non-local terms, which properly account for the chemical bonding changes according to the local environments, are added to the Tersoff potential. Consequently, the REBO potential allows for bond formation and breaking with appropriate changes in atomic hybridization, which is extremely important for the realistic treatment of such processes as chemical reactions. However, in the first generation REBO potential, the terms describing the pair interaction in Eqn (2.1.1) effectively describe equilibrium distances, bond energies, and force constants simultaneously. Therefore, the second-generation REBO potential, using improved analytic function and fitting more experimental/*first principle* data, was developed[8]. The forces associated with rotation about dihedral angles for carbon-carbon double bonds, as well as angular interactions associated with hydrogen centers, have also been included. In our study, the second generation REBO potential[8] is used.

The analytic terms describing the pair interactions in (2.1.1) in the second-generation REBO potential are written as

$$V_R(r) = f^c(r) \left(1 + Q/r\right) A e^{-\alpha r} \quad (2.1.2)$$

$$V_A(r) = f^c(r) \sum_n B_n e^{\beta_n r} \quad (2.1.3)$$

The repulsive term (Eqn (2.1.2)) goes to infinity as the interatomic distance r approaches zero, however, the attractive term (Eqn (2.1.3)) is flexible enough to fit the bond properties

simultaneously. The variables Q , A , α , B , and β are parameters fit to experimental or *ab initio* data for both hydrocarbon molecules and solid-state carbon with a standard fitting routine. The function $f^c(r)$ limits the range of the covalent interactions, for example, the value of $f^c(r)$ for carbon-carbon interactions will be one for nearest neighbors and zero for all other interatomic distances.

In the second-generation REBO potential, the bond-order term is written as

$$b_{ij} = \frac{1}{2} [b_{ij}^{\sigma-\pi} + b_{ji}^{\sigma-\pi}] + b_{ij}^{\pi} \quad (2.1.4)$$

where the values of $b_{ij}^{\sigma-\pi}$ and $b_{ji}^{\sigma-\pi}$ depend on the local coordination and bond angle between atoms i and j , and the values of b_{ij}^{π} is evaluated using the formula

$$b_{ij} = \prod_{ij}^{RC} + b_{ij}^{DH} \quad (2.1.5)$$

where the value of the first term depends on whether a bond between atoms i and j has radical character and is part of a conjugated system, and the value of the second term depends on the dihedral angle for carbon-carbon double bonds.

This revised second-generation REBO potential accurately reflects the bond energies, bond length and force constant for carbon-carbon bonds with a single expression (Eqn (2.1.1)). It also improves the fit to radical energies, conjugated π bonding properties, and diamond surface properties and gives a reasonable description of diamond, graphite, and hybrid diamond-graphite structures[9]. In order to describe the long-range van der Waals interaction,

Lennard-Jones (LJ) 6-12 potential is introduced into Eqn (2.1.1). Thus the combined expression to evaluate the binding energy of the whole system is

$$U = \sum_i \sum_{j(>i)} [V_R(r_{ij}) - b_{ij}V_A(r_{ij}) + V_{vdw}(r_{ij})] \quad (2.1.6)$$

where V_{vdw} is the contribution from the van der Waals interactions, which are expressed as

$$V_{vdw}(r) = 4\varepsilon \left[\left(\frac{\sigma}{r} \right)^{12} - \left(\frac{\sigma}{r} \right)^6 \right] \quad (2.1.7)$$

where ε and σ are Lennard-Jones parameters [10].

2.2 MOLECULAR DYNAMICS

Molecular dynamics simulations consist of the numerical, step by step solution of the classical equations of motion governed by the Newton's second law, which states that in order to make a body of mass m undergo an acceleration a , a force F is required that is equal to the product of the mass times the acceleration:

$$F = ma \quad (2.2.1)$$

This equation can also be expressed in term of the position r of the body as

$$F = m \frac{d^2r}{dt^2} \quad (2.2.2)$$

This is the basis of molecular dynamics (MD). Knowing the force, F , on each body based

on the Eqn (2.2.2), we can then study the trajectory of each body in space and investigate the time-dependent properties. The key point is to calculate the force F acting on each body, according to the conservation of energy, which states that the sum of the kinetic energy ($\frac{1}{2}mv^2$) and the potential energy (U) is constant (ε) for certain system, this is

$$\frac{1}{2}mv^2 + U = \varepsilon \quad (2.2.3)$$

By differentiating both sides of Eqn (2.2.3) with respect to time, we can get

$$m \frac{d^2r}{dt^2} = -\nabla U \quad (2.2.4)$$

Comparing the Eqn (2.2.4) with the Newton's second law (Eqn (2.2.1)). It is easy to know the force can be calculated from the potential energy

$$F = -\nabla U \quad (2.2.5)$$

The potential energy can be calculated using an empirical potential, a semi-empirical potential or first-principle approaches.

The potential energy in the molecular dynamics can be calculated using empirical potentials derived from experimental data or first-principle approaches. The calculations of potential energy and force are the most time consuming part in the MD simulation. Once the forces are obtained, Eqn (2.2.2) can be integrated to follow the time evolution of the atoms under the applied force.

In practice, the equations of motions for all the atoms should be solved numerically since there is no analytical solution available. There are several numerical methods to integrate Newton's equations, including the Verlet algorithm, the Verlet Leapfrog (LF) algorithm, and the predictor-corrector algorithm[11]. In our MD simulation, the Verlet Leapfrog integration algorithm, which is time reversible, simple and generates trajectories in the microcanonical (NVE) ensemble having conserved total energy, is applied. The LF algorithm requires values of position and force as the time, while the velocities are half a timestep behind. The first step is to advance the velocities by integration of the force:

$$v(t + \frac{1}{2}\Delta t) \leftarrow v(t - \Delta t) + \Delta t \frac{f(t)}{m} \quad (2.2.6)$$

where m is the mass of an atom and t is the timestep.

The positions are then advanced using the new velocities:

$$r(t + \Delta t) \leftarrow r(t) + \Delta t \cdot v(t + \frac{1}{2}\Delta t) \quad (2.2.7)$$

Molecular dynamics normally requires properties that depend on position and velocity at the same time (such as the sum of potential and kinetic energy). In the LF algorithm the velocity at time t is obtained from the average of the velocities v half a timestep either side of time t :

$$v(t) \leftarrow \frac{1}{2} \left[v(t - \frac{1}{2}\Delta t) + v(t + \frac{1}{2}\Delta t) \right] \quad (2.2.8)$$

In MD simulations, short time steps are required to yield reliable results. There are at

least two reasons for this. One is due to the high frequency motion of the atoms (for example, the time scale of atomic vibration is typically $\sim 10^{-13}$ s). In order to capture atomic motion as accurately as MD simulations desire to do, the timestep must be much smaller than the time-scale of the atomic motions. The second reason is that, from the integration point of view, a small Δt is necessary to achieve the predictions calculated in LF algorithm as accurately as possible. Usually, a timestep on the order of a femtosecond (10^{-15} s) is used. Unfortunately, such short a timestep precludes the modeling of processes that occur on time-scale larger than a few nanoseconds with present-day computational power.

The instantaneous kinetic temperature in the molecular dynamics simulations can be calculated from the atomic velocities if the system has no net momentum:

$$T = \frac{\sum \frac{1}{2}mv^2(t)}{k_B f} \quad (2.2.9)$$

where k_B is Boltzmann's constant and f is the number of degrees of freedom in the system. It is impossible to track the kinetic temperature of a system to the set temperature exactly in molecular dynamics. Various types of thermostat methods, such as Berendsen[12], Langevin[13] and Nose-Hoover[14-16], have been introduced to control the atomic motions. The Langevin thermostats[13] follow the Langevin equation of motion instead of Newton's equation of motion. In the Langevin equation of motion, a frictional force added to the conservative force is proportional to the velocity, and it adjusts the kinetic energy of the particle so that the temperature matches the set temperature. Nosé-Hoover thermostat[14-16] is an integral type of thermostat, and it introduces additional degrees of freedom (momentum)

into the Hamiltonian of a system. The Berendsen thermostat[12] was used in the simulations discussed below. The Berendsen thermostat[12] maintains the simulation temperature close to the set temperature, T_{ext} , by re-scaling the velocities of the atoms at each step:

$$\chi(t) \leftarrow \left[1 + \frac{\Delta t}{\tau_T} \left(\frac{T_{ext}}{T(t)} - 1 \right) \right]^{1/2} \quad (2.2.10)$$

where τ_T is the thermostat relaxation time. LF algorithm implements this thermostat as follows.

$$\begin{aligned} r(t + \Delta t) &\leftarrow r(t) + \Delta t v(t + \frac{1}{2}\Delta t) \\ v(t) &\leftarrow \left[v(t - \frac{1}{2}\Delta t) + \Delta t \frac{f(t)}{m} \right] \chi(t) \\ v(t) &\leftarrow \frac{1}{2} \left[v(t - \frac{1}{2}\Delta t) + v(t + \frac{1}{2}\Delta t) \right] \end{aligned} \quad (2.2.11)$$

Tracking the system pressure to the set pressure P or stress σ is even harder in molecular dynamics. The pressure tensor P can be calculated using Clausius virial theorem as

$$P = \frac{2}{V} (E_{kin} - \Xi) \quad (2.2.12)$$

with the box volume V , the kinetic energy E_{kin} and the inner virial tensor

$$\Xi = -\frac{1}{2} \sum_{i < j} r_{ij} \cdot F_{ij} \quad (2.2.13)$$

Correcting the pressure in a simulation can be achieved through a change in the inner virial Ξ by scaling the inter-particle distances. This correction usually takes several iterations to obtain self-consistency in computations because of the interdependence of r_{ij} and F_{ij} . The

first barostat was developed by Andersen[17] to adjust the pressure in a simulation of interacting particles. Parinello and Rahman[18] later extended Anderson's method to allow the simulation box to change in shape. This method was further developed by Hoover, which is known as a Hoover barostat. Another approach is the Berendsen barostat, which is used in our studies. In the Berendsen method[12], the system is weakly coupled to an external bath using the principle of least local perturbation. Similar to the temperature coupling, an extra term is added to the equations of motions that effects a pressure change

$$\left(\frac{dP}{dt}\right)_{bath} = \frac{P_{ext} - P}{\tau_P} \quad (2.2.14)$$

where τ_P is the time constant for the coupling. A simple proportional coordinate scaling, concomitant with volume scaling, minimizes local disturbances. For anisotropic cell variation, a tensor is defined by

$$\eta = 1 - \frac{\beta \Delta t}{\tau_P} (P_{ext} - \sigma) \quad (2.2.15)$$

where β is a specified constant. In our simulation, it is taken to be the isothermal compressibility of liquid water. The new position for each atom is given by

$$r_i(t + \Delta t) = \eta r_i(t) \quad (2.2.16)$$

2.3 LOCAL STRESS ANALYSIS

The local stress analysis was introduced to obtain the stress information associated with each atom. The local stress calculation during the molecular dynamics in our study is based on the unpublished paper by Falk[19]. The derivation of the stress tensor was based on the microscopic momentum field. The final expression in most treatments of the stress tensor for the purpose of MD is

$$\sigma^{\alpha\beta}(R, t) = \sum_i \left\{ -\frac{p_i^\alpha p_i^\beta}{m_i} \delta(R - r_i) + \frac{1}{2} \sum_{i \neq j} r_{ij}^\alpha F_{ij}^\beta \delta(R - r_i) \right\} + \sigma_0^{\alpha\beta} \quad (2.3.1)$$

where the term $\sigma_0^{\alpha\beta}$ is an integration constant which must be defined to insure that the expression is translationally and rotationally invariant, R represents the point of interest, p_i , r_i and m_i are the momentum, position and mass of the atom i , $r_{ij} = r_i - r_j$ and $F_{ij} = F_i - F_j$ denote the distance and force vector between atoms i and j .

To evaluate the average local stress over a region, we need to sum the local stress (Eqn (2.3.1)) of atoms and coarse-grain it over the region. According to the Hardy[20] rules, the kinetic contribution (first term in Eqn (2.3.1)) of local stress over a uniform symmetrical region of radius R_0 can be expressed as

$$\bar{\sigma}_K^{\alpha\beta}(R) = -\frac{1}{V(R_0)} \sum_{i \in R} m_i \dot{r}_i^\alpha \dot{r}_i^\beta + \frac{1}{MV(R_0)} \sum_{i \in R} m_i \dot{r}_i^\alpha \sum_{j \in R} m_j \dot{r}_j^\beta \quad (2.3.2)$$

where $M = \sum_{i \in R} m_i$ represents the total mass in spatial region of radius R_0 . By applying the same rules, the potential contribution (second term in Eqn (2.3.1)) of local stress can be expressed as

$$\bar{\sigma}_P^{\alpha\beta} = \frac{1}{2} \sum_{j \neq i} r_{ij}^\alpha F_{ij}^\beta B(r_i, r_j, R) \quad (2.3.3)$$

$$B(r_i, r_j, R) = w(|r_j - R|) \quad (2.3.4)$$

$$w(r) = \frac{\Theta(R_0 - r)}{V(R_0)} \quad (2.3.5)$$

where w is the envelope function, Θ is the heavy-side step function and $V(R_0)$ is the volume inside of radius R_0 . In our study, we consider the uniform envelope function $w(r)$ which has a value equal to a weighted contribution proportional to the fraction of the bond that falls inside the area (dark portion of each bond in Figure 2.1).

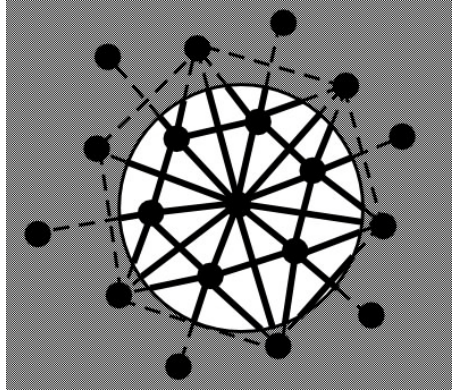


Figure 2.1 In the full expression the bonds are counted to the extent they cross the area of interest. Dark segments of bonds contribute; dotted segments do not.

2.4 REFERENCES

1. Abell, G.C., *EMPIRICAL CHEMICAL PSEUDOPOTENTIAL THEORY OF MOLECULAR AND METALLIC BONDING*. Physical Review B, 1985. **31**(10): p. 6184-6196.
2. Tersoff, J., *EMPIRICAL INTERATOMIC POTENTIAL FOR SILICON WITH IMPROVED ELASTIC PROPERTIES*. Physical Review B, 1988. **38**(14): p. 9902-9905.
3. Tersoff, J., *EMPIRICAL INTERATOMIC POTENTIAL FOR CARBON, WITH APPLICATIONS TO AMORPHOUS-CARBON*. Physical Review Letters, 1988. **61**(25): p. 2879-2882.
4. Petukhov, A.V. and A. Fasolino, *Reconstructions of diamond (100) and (111) surfaces: Accuracy of the Brenner potential*. Physica Status Solidi a-Applied Research, 2000. **181**(1): p. 109-114.
5. Petukhov, A.V., et al., *(Meta)stable reconstructions of the diamond (111) surface: Interplay between diamond and graphitelike bonding*. Physical Review B, 2000. **61**(16): p. 10590-10593.
6. Shenderova, O.A., D.M. Gruen, and Knovel. *Ultrananocrystalline diamond synthesis, properties, and applications*. 2006.
7. Brenner, D.W., *ATOMISTIC COMPUTER-SIMULATIONS OF THE REACTIVE DYNAMICS OF DIAMOND SURFACES*. Carbon, 1990. **28**(6): p. 769-770.
8. Brenner, D.W., et al., *A second-generation reactive empirical bond order (REBO) potential energy expression for hydrocarbons*. Journal of Physics-Condensed Matter, 2002. **14**(4): p. 783-802.
9. Brenner, D.W., et al., *Atomic modeling of carbon-based nanostructures as a tool for developing new materials and technologies*. Cmes-Computer Modeling in Engineering & Sciences, 2002. **3**(5): p. 643-673.
10. Allen, M.P. and D.J. Tildesley, *Computer simulation of liquids*. 1987, Oxford [England]; New York: Clarendon Press ; Oxford University Press.
11. Frenkel, D., B. Smit, and M.A. Ratner, *Understanding Molecular Simulation: From Algorithms to Applications*. Physics today., 1997. **50**(7): p. 61.

12. Berendsen, H.J.C., et al., *MOLECULAR-DYNAMICS WITH COUPLING TO AN EXTERNAL BATH*. Journal of Chemical Physics, 1984. **81**(8): p. 3684-3690.
13. Adelman, S.A. and J.D. Doll, *GENERALIZED LANGEVIN EQUATION APPROACH FOR ATOM-SOLID-SURFACE SCATTERING - GENERAL FORMULATION FOR CLASSICAL SCATTERING OFF HARMONIC SOLIDS*. Journal of Chemical Physics, 1976. **64**(6): p. 2375-2388.
14. Nose, S., *A MOLECULAR-DYNAMICS METHOD FOR SIMULATIONS IN THE CANONICAL ENSEMBLE*. Molecular Physics, 1984. **52**(2): p. 255-268.
15. Nose, S., *A UNIFIED FORMULATION OF THE CONSTANT TEMPERATURE MOLECULAR-DYNAMICS METHODS*. Journal of Chemical Physics, 1984. **81**(1): p. 511-519.
16. Hoover, W.G., *CANONICAL DYNAMICS - EQUILIBRIUM PHASE-SPACE DISTRIBUTIONS*. Physical Review A, 1985. **31**(3): p. 1695-1697.
17. Andersen, H.C., *MOLECULAR-DYNAMICS SIMULATIONS AT CONSTANT PRESSURE AND-OR TEMPERATURE*. Journal of Chemical Physics, 1980. **72**(4): p. 2384-2393.
18. Parrinello, M. and A. Rahman, *CRYSTAL-STRUCTURE AND PAIR POTENTIALS - A MOLECULAR-DYNAMICS STUDY*. Physical Review Letters, 1980. **45**(14): p. 1196-1199.
19. Falk, M., *Local stress calculations in molecular dynamics*. 1999, Harvard University: Cambridge. p. 8.
20. Hardy, R.J., *FORMULAS FOR DETERMINING LOCAL PROPERTIES IN MOLECULAR-DYNAMICS SIMULATIONS - SHOCK-WAVES*. Journal of Chemical Physics, 1982. **76**(1): p. 622-628.

CHAPTER 3. STABILITY OF NANODIAMONDS

3.1 INTRODUCTION

For decades, it has been known that graphite is the most stable form in the carbon family at atmospheric pressure, and that diamond, while harder, denser, and more durable, was merely metastable. With the discovery of fullerenes, nanotubes, nanorods, and nanocrystalline diamond by means of detonation synthesis, the door was opened for a new era in carbon science. Many studies were carried out to understand the formation of carbon clusters, and the dynamic phase changes and stability between graphite and nanocrystalline diamond (nanodiamond (ND)) clusters. Barnard[1, 2] explored the relative stability of nanocrystalline diamonds, fullerenes, onions and graphite at the nanoscale and defined size regions and found that the most stable carbon form at the nanoscale progresses from fullerene \rightarrow onions \rightarrow bucky diamond \rightarrow nanodiamond \rightarrow graphite as the system size for all carbon-carbon structures is increased. Fugaciu et al[3] simulated the transition of nanocrystalline diamond to carbon onions using density-functional-theory (DFT) based tight-binding (TB) methods. This transformation of nanodiamond to carbon-onions has also been observed experimentally[3, 4] with a transformation temperature that is dependent on the size of the particle. Barnard et al[1] showed that the stability, characterized by the variation in these structural properties from that of bulk diamond, was dependent on both the surface morphology and the crystallographic direction of the principal axis of the nanowire. These

studies have motivated a number of researchers to re-examine the phase stability of diamond at the nanometer scale.

In our studies, atomistic simulations were performed using the REBO potential[4] to calculate formation energies and preferred morphologies of hydrogenated nanodiamonds.

3.1.1 NANODIAMOND APPLICATION

Because of its extreme hardness, outstanding wear resistance, wide optical transparency, and other unique properties, nanodiamond has been used widely in many fields. The remarkable mechanical properties of NDs suggest immediately their application in abrasive materials or components of coatings[5-7]. The rich surface chemistry of NDs, the absence of toxic impurities and their small size make nanodiamonds very convenient for biomedical applications. By creating specific sites on NDs for selective molecular attachment, nanodiamond can be used for example in nanofabrication, self assembly, nanosensors, bioprobes, drug delivery, and pigments[8]. The typical diameter of NDs is about 5 nm, and about 10% of carbon atoms are at the surface. NDs can have significant π bonding which gives rise to unique electronic and magnetic features due to the lower energy gap of $\pi - \pi^*$ transitions relative to $\sigma - \sigma^*$ transitions. The investigation of field electrons from ND-based structures [9-11] has shown their potential for electrochemical electrodes and field emission structure, where high conductivities are required[10].

3.1.2 CHARACTERIZATION AND STRUCTURE OF NANODIAMONDS

Usually the term ‘nanodiamond’ (ND) refers to the nanodiamond crystal found in

meteorites, crystalline grains in polycrystalline diamond films and nanodiamond powders and suspensions prepared by detonation synthesis. Nanodiamonds usually are produced by chemical treatment of diamond-containing mixtures, which are synthesized at high pressure and high temperature with a shock wave during detonation of carbon-containing explosives with a negative oxygen balance. More details on the synthesis and processing of ND can be found in [12]. The NDs produced by means of detonation are complex materials that have at least a three-layer structure[5]:

- A diamond core with a characteristic size of about 5 nm[13-15];
- An intermediate carbon shell around the core, which is comprised of an amorphous carbon structure with a thickness of 0.4 – 1.0 nm containing 10-30% carbon atoms;
- A surface layer which contains, in addition to carbon atoms, other heteroatoms (N, H, O) forming a great variety of functional groups.

3.2 STABILITY OF NANODIAMONDS

Until recently, most of the experimental work described the shape of detonation nanodiamond as being spherical based on the transmission electron microscopy (TEM) images. Part of the reason is that the surface of nanodiamond is usually graphitic because of its high surface energy associated with unterminated sp³ bonds as demonstrated in Figure 3.1. The partially graphitized structure (right structure in Figure 3.1) was generated starting with

the cuboctahedral morphology C66 (left structure in Figure 3.1) using a semi-empirical potential PM3. However, high-resolution TEM (HRTEM) studies revealed that ND particles rarely have a spherical shape[16, 17]. The controlled annealing of ND at temperatures of 1150-2140 K with simultaneous imaging by HRTEM also showed the transformation of the surface of NDs from carbon sp²/sp³ nanocomposites, onion-like carbon (OLC) to hollow graphite polyhedrons[18]. HRTEM micrographs of original ND particles of different sizes and shapes can also be found in [17]. These clusters consisted typically of regularly shaped cuboctahedral and twinned crystals.

The size distribution of nanodiamond is 4-6 nm which was reported more than once[13-15]. The reason for this lies in that nanodiamond and not graphite is the most thermodynamically stable form of nanocarbon cluster. This view is also supported by the results from computer simulation of the stability of carbon clusters[1, 13, 19]. In this study, this work was extended to include three hydrogenated morphologies of nanodiamond clusters. The calculation of formation energies and preferred morphologies was performed using atomic simulations with the second-generation REBO potential interaction for hydrocarbons[4].

The three hydrogenated morphologies of nanodiamond clusters considered in our studies are octahedral, cuboctahedral and spherical as shown in Figure 3.2. However, the sp² on the (100) surface of nanodiamond usually forms single/double bonded dimers, as illustrated in Figure 3.3, via surface reconstruction[20]. Therefore, a (001)2x1 reconstructed cuboctahedral structure is also considered in our calculation.

For the analysis of particle energies, surface reconstructions, and interactions with specific functional groups, it is good to know the dependence of the number of under-coordinated surface atoms on particle size. After examining the structure of octahedral nanodiamond, a ‘nanodiamond formula’ for octahedral particles was derived:

$$\begin{aligned}
 N_{C2} &= 6 \\
 N_{C3} &= 4N^2 - 12 \\
 N_{surface} &= N_{C2} + N_{C3} = 4N^2 - 6 \\
 N_{total} &= N(4N^2 - 1)/3
 \end{aligned} \tag{3.2.1}$$

where N is the number of atoms along an octahedral edge, and N_{C2} and N_{C3} are the number of 2- and 3-coordinated atoms, respectively. By truncating the six vertices of octahedral nanodiamond, a cubo-octahedral nanodiamond is formed. However, the formulas are different for N odd and even.

$$\begin{aligned}
 N_{C2} &= \begin{cases} \frac{3(N^2-1)}{2} & N \text{ is odd} \\ \frac{3N^2}{2} & N \text{ is even} \end{cases} \\
 N_{C3} &= \begin{cases} N^2 & N \text{ is odd} \\ N^2 + 3 & N \text{ is even} \end{cases} \\
 N_{total} &= \begin{cases} \frac{1}{12}N(2N+1)(5N+2) & N \text{ is odd} \\ \frac{1}{12}(10N^3+9N^2+2N+9) & N \text{ is even} \end{cases}
 \end{aligned} \tag{3.2.2}$$

where N is the number of atoms along the edge of a corresponding octahedral structure. Unfortunately, there is no such formula for spherical NDs. Statistics on under-coordinated atoms for a series of spherical nanodiamond, obtained from atomistic modeling, are illustrated in Figure 3.4.

In NDs with diameters less than 5 nm, close to 20% of the total number of atoms are at the surface. This fraction grows dramatically as the particles decrease in size, so that the

properties of NDs become dominated by their surface. In other words, the shape of a ND is closely related to its stability, which in turn depends on the sp^2/sp^3 ratio of hybridized carbon atoms at the surface, and the presence and type of defects in the bulk (for example, twins in particles of pentagonal shape). The stability of nanodiamond particles will also depend on the presence of a specific functional group on the surface, impurities in the bulk, and the interface energy between the nanodiamond and the surrounding matrix if a particle is embedded in the matrix.

The molar heat of formation of a compound (ΔH_f), a key property in thermochemistry, is the change of enthalpy that accompanies the formation of 1 mole of a substance in its standard state from its constituent elements in their standard states (the most stable form of the element at 101.325 kPa of pressure and the specified temperature, usually 298 K). It is also a key property to determine the relative stability of isomeric systems. For notional compounds, significant resources could be expended in synthesizing the material, only to discover upon measuring its ΔH_f that it is an unsuitable candidate for use. Therefore, computational tools have been developed as an alternative to predict this key property.

To establish an analytic expression for the heats of formation associated with the under-coordinated surface atoms of a certain type, histograms of energy distributions within hydrogenated octahedra and reconstructed (001)2x1 cubo-octahedra structures have been generated (Figure 3.5). The possibility of analyzing the distribution of atomic energies within clusters is an advantage of an analytic potential in comparison with more sophisticated methods that typically provide total energies of systems. As illustrated in Figure 3.5 (top),

specific groups of atoms (on vertices, (111) faces and 4-coordinated atoms in the bulk) have very similar binding energies with each group that is essentially independent of particle sizes. In contrast the local atomic energies are more markedly size-dependent for cubo-octahedra clusters, as illustrated at Figure 3.5 (bottom), although specific groups of atoms (on vertices, edges, (111) and (001) faces) can clearly be distinguished.

Cohesive energies of series of octahedra and reconstructed cubo-octahedra structures having the carbon atom number for each carbon type as expressed in Eqn (3.2.1) and (3.2.2) have been calculated, and some values for specific surface atoms are provided in the caption of Figure 3.5. Based on known local atomic energies for specific surface atoms, cohesive energies can generally be described as:

$$E_{ND} = E_{C4} \cdot N_{C4} + E_{C3} \cdot N_{C3} + E_{C2} \cdot N_{C2} + E_{H(C3)} \cdot N_{H(C3)} + E_{H(C2)} \cdot N_{H(C2)} \quad (3.3.1)$$

or, similarly:

$$\frac{E_{ND}}{N_C} = E_{C4} + (E_{C3} - E_{C4}) \frac{N_{C3}}{N_C} + (E_{C2} - E_{C4}) \frac{N_{C2}}{N_C} + E_{H(C3)} \frac{N_{H(C3)}}{N_C} + E_{H(C2)} \frac{N_{H(C2)}}{N_C} \quad (3.3.2)$$

The latter formula provides more details regarding the contribution to the cohesive energy of particular types of under-coordinated atoms and their fraction in the particle as compared to the ‘traditional’ equation:

$$\frac{E_{ND}}{N_C} = E_C + E_H \cdot \frac{N_H}{N_C} \quad (3.3.3)$$

Results of predictions are illustrated in Figure 3.6. For comparison, the energies for the same clusters relaxed using the REBO potential are also shown in Figure 3.6. While for octahedra both analytic and atomic simulation approaches show similar results, for small cubo-octahedra structures there is a difference in the results of the two approaches. Also, the intersections with the energy axis, which can be referred as the ‘nanodiamond’ energy, are the same, although the slopes for these two curves are different. The energy is -7.37 eV, which is the cohesive energy of bulk diamond.

From the comparison of cluster energies calculated with an empirical interatomic potential and REBO potential, we can conclude the following: (1) it is not recommended to use a small cluster to fit parameters for an empirical interatomic potential; (2) it is recommended fitting to data from the same cluster series. It would be interesting to calculate nanodiamond energies for all-carbon clusters to re-examine the relative stability taking into account the above considerations. Obviously, corresponding atomic energies for macroscopic surfaces obtained from first principle calculations can be used to predict particle energies, and any functional group can be analyzed similarly.

In our studies, formation energies and preferred morphologies are calculated using the second-generation REBO, a bond-order potential for hydrocarbons:

$$\Delta H_f^\circ(ND) = N_C \cdot \Delta H_f^\circ(C) + N_H \cdot \Delta H_f^\circ(H) - (E^{at} - E_{zpe}) \quad (3.3.4)$$

Dividing by N_C , Eqn (3.3.4) becomes

$$\frac{\Delta H_f^\circ(ND)}{N_C} = \Delta H_f^\circ(C) + \frac{N_H}{N_C} \cdot \Delta H_f^\circ(H) - \frac{(E^{at} - E_{zpe})}{N_C} \quad (3.3.5)$$

where E^{at} is the atomization energy obtained from the simulation, E_{zpe} is the zero point energy[4], which is accounted for only for small clusters, $\Delta H_f^\circ(C)=7.40$ eV is the experimental atomic enthalpy of formation at 0 K for carbon gaseous atom from carbon standard state (graphite)[21] and $\Delta H_f^\circ(H)=2.239$ eV is the atomic enthalpy for the formation of gaseous hydrogen atoms from the hydrogen standard state (H₂ molecule)[4].

Results of the calculations for octahedral and several sub-series of cubo-octahedral NDs are shown in Figure 3.7. It is also worthwhile to note that the unreconstructed octahedral diamond becomes structurally unstable for $N \geq 15$ in the simulation with the REBO. From Figure 3.7, the stability of nanodiamond depends on its size and shape; some series become more stable and some series become less stable with increasing size. However, all series are bounded by curves corresponding to hydrogenated octahedra and (001) 2x1 reconstructed cubo-octahedra. When linearly fitting these two curves, the intercept represents the heats of formation of a particle with $N_H/N_C \rightarrow 0$, that is bulk diamond (~ 0.5 Kcal/mole).

In addition to the cubo-octahedra and octahedra clusters, we also calculated the heats of formation for spherical clusters. Two series of pentagonal particles from Shenderova et al.[22] are also included for comparison. The results are shown on Figure 3.8. From this figure, it can be concluded that hydrogenated octahedra has the most stable morphology considered in our simulation. Barnard also demonstrated that nanodiamond is more stable in the size between ~ 1.9 nm and ~ 5.2 nm[13] than fullerene and graphite. Although there may

be many more morphologies of nanodiamond, the octahedra structure is the most stable structure at the nanoscale.

3.3 SUMMARY

The predicted stabilities of ND particles are carried in our studies. The results showed that the stabilities are not only size dependent but also surface orientation dependent. Taken together synthetic methods for making NDs, NDs are more energetically favorable particles than graphite at nanoscale. However, the surface of NDs will transform to fullerenes or onion like structures when their size decreases to less than 2 nm due to surface transformation to fullerene like structure or dimer formation. The heats of formation for 6 ND particle clusters predicted by REBO suggested that octahedra structure is the most stable structure at nanoscale although there may be many more morphologies of nanodiamond.

3.4 REFERENCES

1. Barnard, A.S., S.P. Russo, and I.K. Snook, *Ab initio modelling of the stability of nanocrystalline diamond morphologies*. Philosophical Magazine Letters, 2003. **83**(1): p. 39-45.
2. Barnard, A.S., S.P. Russo, and I.K. Snook, *Coexistence of bucky diamond with nanodiamond and fullerene carbon phases*. Physical Review B, 2003. **68**(7): p. 4.
3. Fugaciu, F., H. Hermann, and G. Seifert, *Concentric-shell fullerenes and diamond particles: A molecular-dynamics study*. Physical Review B, 1999. **60**(15): p. 10711-10714.
4. Brenner, D.W., et al., *A second-generation reactive empirical bond order (REBO) potential energy expression for hydrocarbons*. Journal of Physics-Condensed Matter, 2002. **14**(4): p. 783-802.
5. Dolmatov, V.Y., *Polymer-diamond composites from detonation-derived nanodiamonds. Part 1*. Sverkhтвердые Materialy, 2007. **1**: p. 15.
6. Dolmatov, V.Y., *Polymer-diamond composites based on detonation nanodiamonds. Part 2*. Sverkhтвердые Materialy, 2007. **2**: p. 15.
7. Zhang, Q., et al., *Polyimide/Diamond nanocomposites: Microstructure and indentation Behavior*. Macromolecular Rapid Communications, 2007. **28**(21): p. 2069-2073.
8. Roy, R.R., *Biomedical applications of diamond-like carbon coatings: a review*. Journal of biomedical materials research. Part B, Applied biomaterials, 2007. **83B**(1): p. 72.
9. Okotrub, A.V., et al., *Field emission from products of nanodiamond annealing*. Carbon, 2004. **42**(5-6): p. 1099-1102.
10. Williams, O.A., *Ultrananocrystalline diamond for electronic applications*. Semiconductor Science and Technology, 2006. **21**(8): p. R49-R56.
11. Lee, Y.C., et al., *Synthesis and electron field emission properties of nanodiamond films*. Diamond and Related Materials, 2004. **13**(11-12): p. 2100-2104.

12. Baidakova, M. and A. Vul, *New prospects and frontiers of nanodiamond clusters*. Journal of Physics D-Applied Physics, 2007. **40**(20): p. 6300-6311.
13. Barnard, A.S., S.P. Russo, and I.K. Snook, *Size dependent phase stability of carbon nanoparticles: Nanodiamond versus fullerenes*. Journal of Chemical Physics, 2003. **118**(11): p. 5094-5097.
14. Badziag, P., et al., *NANOMETRE-SIZED DIAMONDS ARE MORE STABLE THAN GRAPHITE*. Nature, 1990. **343**(6255): p. 244-245.
15. Hwang, N.M., J.H. Hahn, and D.Y. Yoon, *Chemical potential of carbon in the low pressure synthesis of diamond*. Journal of Crystal Growth, 1996. **160**(1-2): p. 87-97.
16. Tyler, T., et al., *Electron emission from diamond nanoparticles on metal tips*. Applied Physics Letters, 2003. **82**(17): p. 2904-2906.
17. Shenderova, O.A., D.M. Gruen, and Knovel. *Ultrananocrystalline diamond synthesis, properties, and applications*. 2006.
18. Butenko, Y.V., et al., *Kinetics of the graphitization of dispersed diamonds at "low" temperatures*. Journal of Applied Physics, 2000. **88**(7): p. 4380-4388.
19. Raty, J.Y., et al., *Quantum confinement and fullerene-like surface reconstructions in nanodiamonds*. Physical Review Letters, 2003. **90**(3).
20. Barnard, A.S., et al., *A Monte Carlo Study of Surface Reconstruction in (100) and (111) Diamond Surfaces and Nanodiamond*. Molecular Simulation, 2004. **30**(1): p. 1-8.
21. Weast, R.C., et al., *CRC handbook of chemistry and physics a ready-reference book of chemical and physical data*. 1984, Boca Raton, Fla.: CRC Press.
22. *Synthesis, Properties And Applications of Ultrananocrystalline Diamond*. 2005: Kluwer Academic Pub.

FIGURES

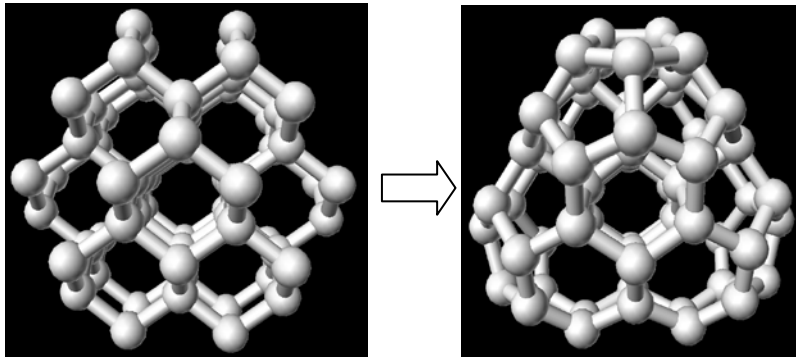


Figure 3.1 The Surface transformation of cubooctahedra to fullerenes like structure

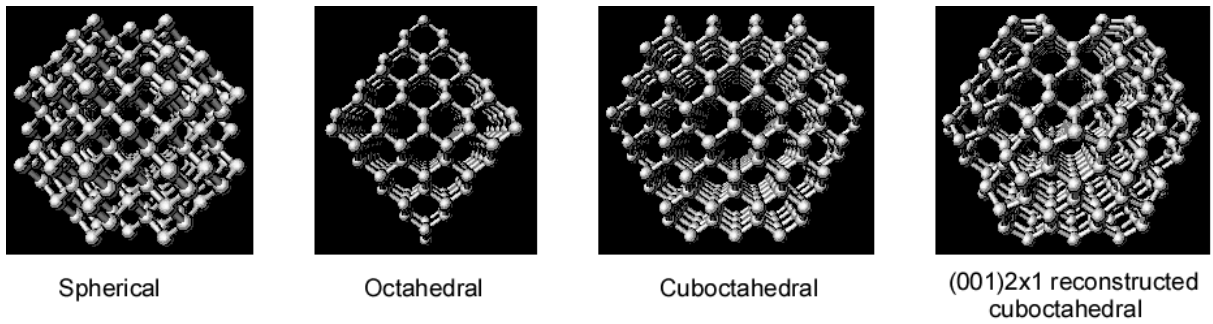


Figure 3.2 Representative structures from the set of ND morphologies simulated.

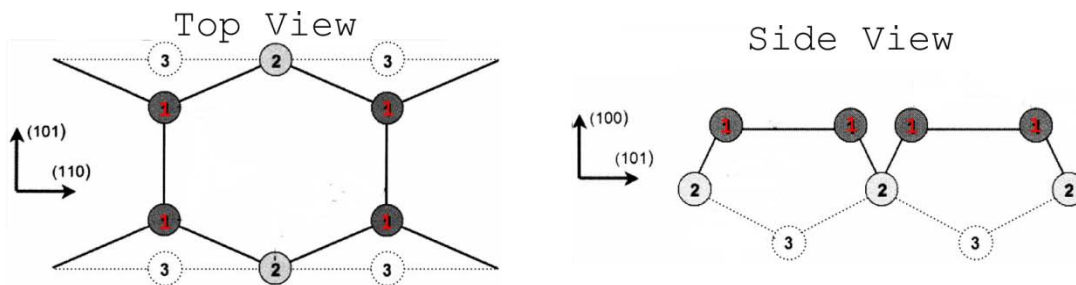


Figure 3.3 Schematic diagram of dimers – top view and side view.

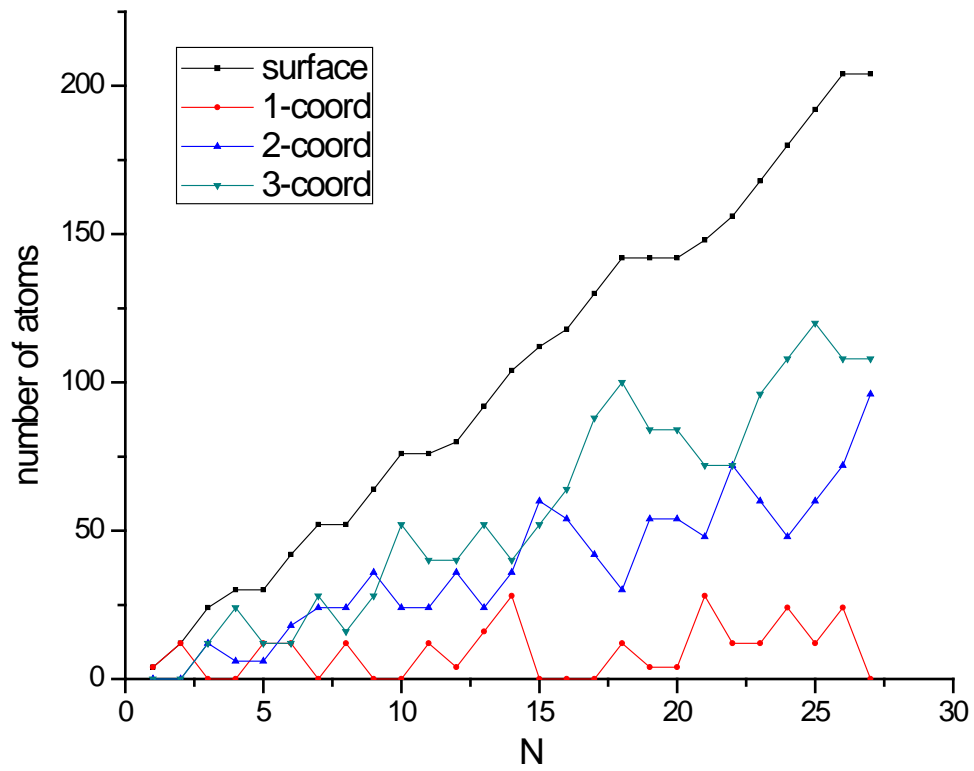


Figure 3.4 Number of under-coordinated surface atoms of different types for a spherical particle as a function of the number of atoms along the diameter.

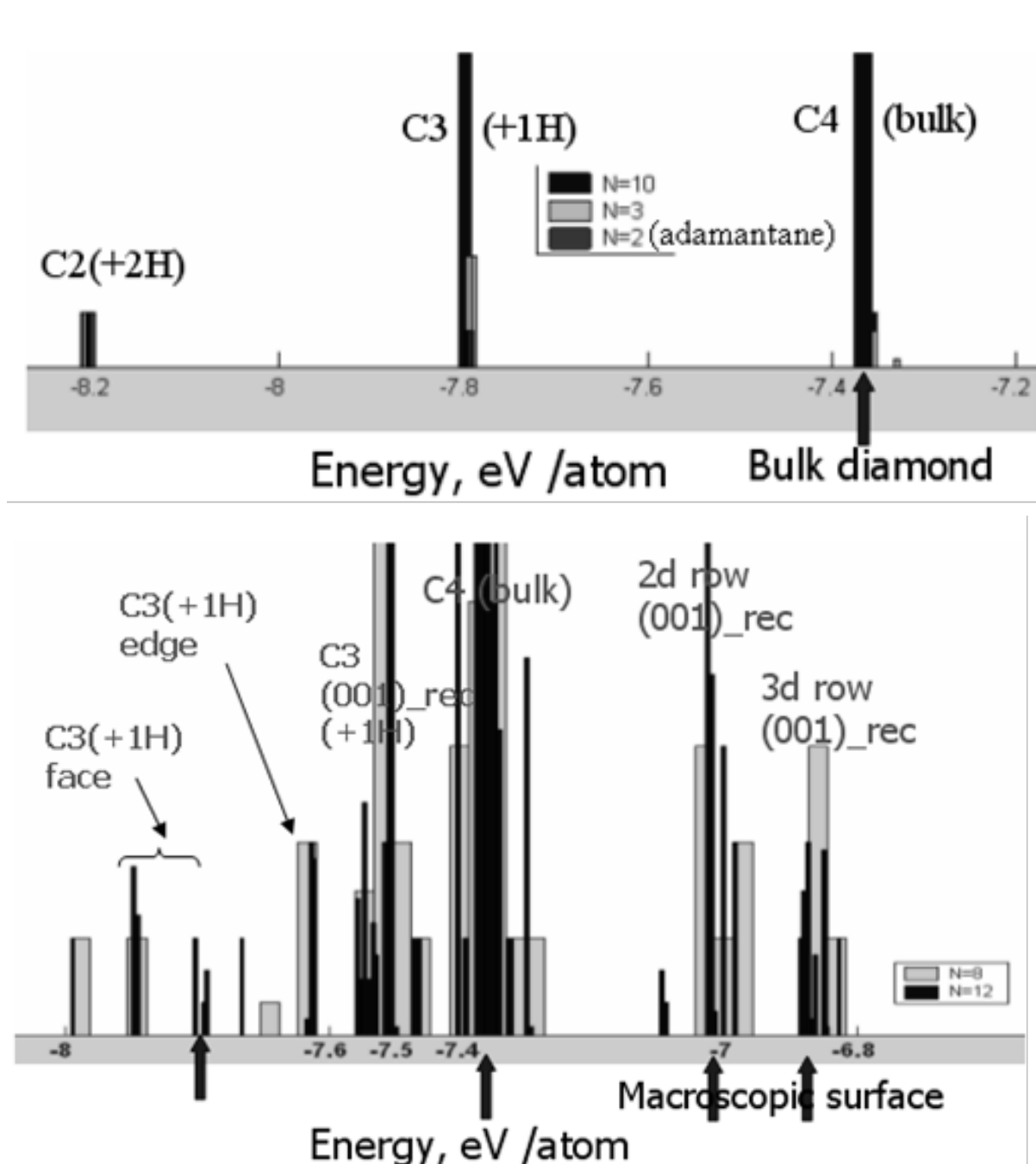


Figure 3.5 Histograms of atomic energies of carbon atoms for three octahedral particles (top) (C10H16 (N=2), C35H36 (N=3), C1330H400 (N=10)) and two cubo-octahedral particles (bottom) (C436H208 (N=8), C1550H432 (N=12)). Arrows from the bottoms of the pictures mark energies of carbon atoms in bulk diamond (-7.37eV) and at the (111) hydrogenated (-7.8 eV) and (100) 2x1 reconstructed (-7.5 for C2+1H, -7eV for C4-2d row and -6.9eV for the C4-3drow) macroscopic surfaces.

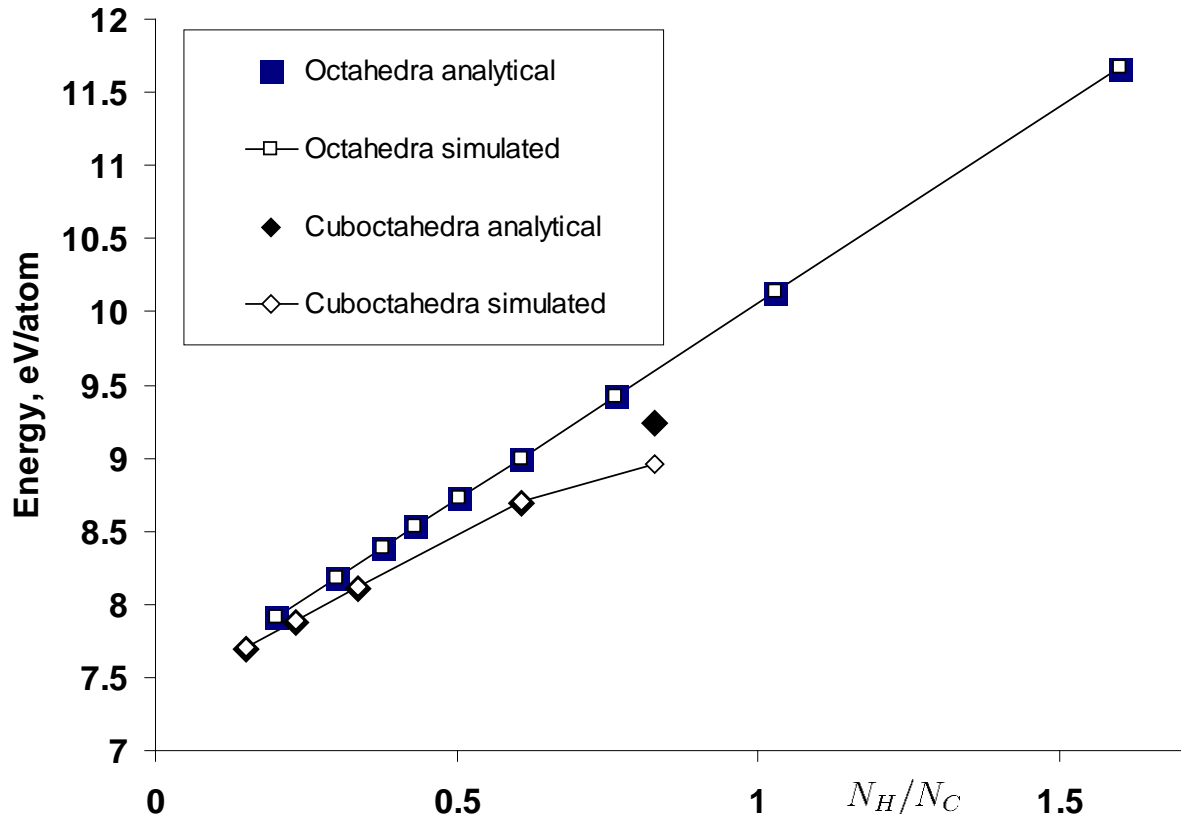


Figure 3.6 Cohesive energy from simulations with the bond-order potential (open symbols) and predicted analytically (solid symbols).

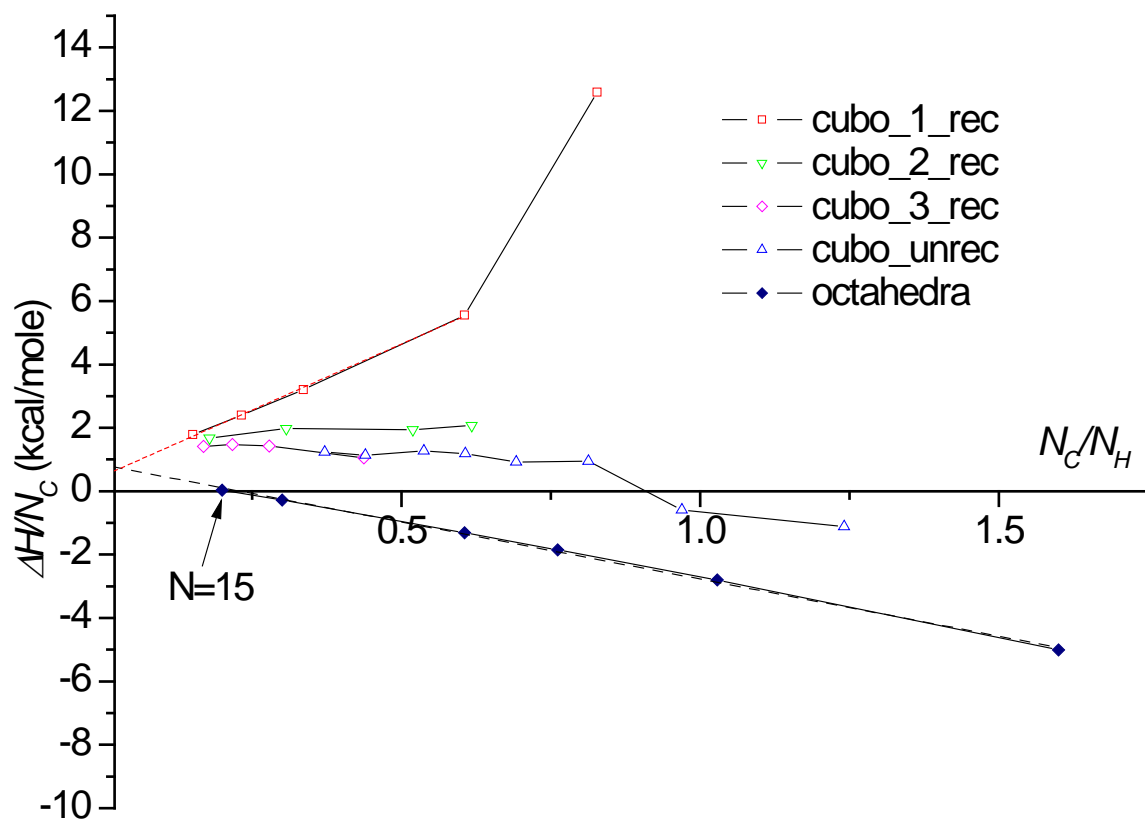


Figure 3.7 Heats of formation for hydrogenated octahedra and cuboctahedra.

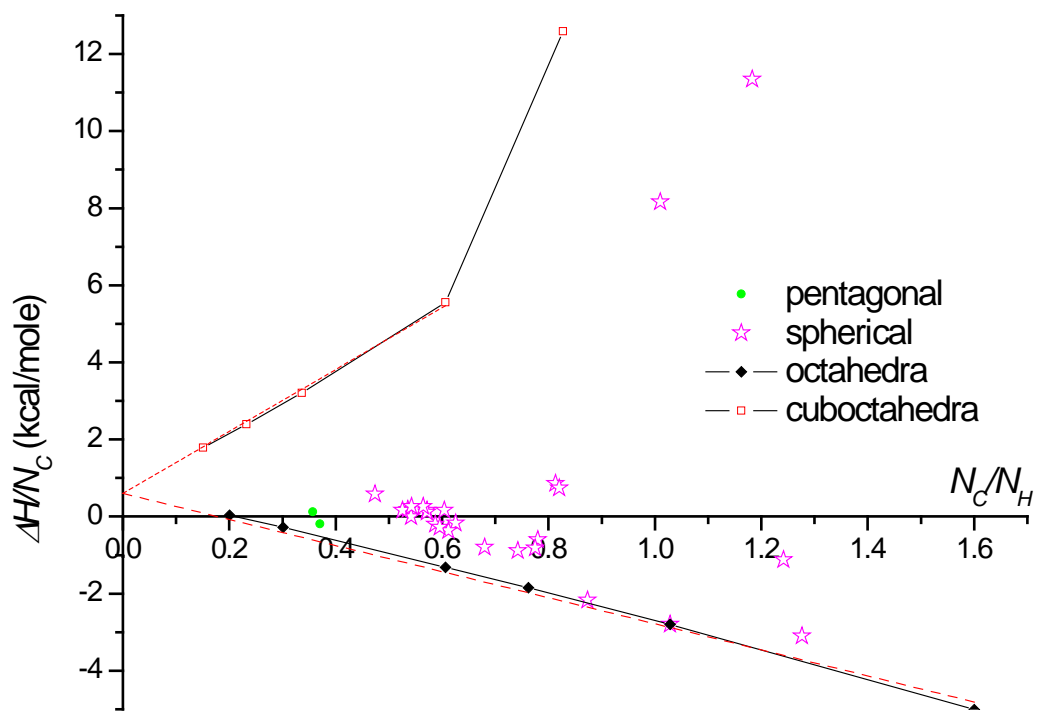


Figure 3.8 Heats of formation for hydrogenated octahedra, (001)2x1 reconstructed cubo-octahedra, spherical clusters and pentagonal clusters.

CHAPTER 4. STABILITY OF NANORODS

4.1 INTRODUCTION

Diamond nanorods (DNRs), one-dimensional analogues of bulk diamond, are an emerging class of carbon nanostructures with promising applications in several fields. Based on their high elastic modulus, strength-to-weight ratio, and the relative ease with which the surface can be functionalized[1], DNRs are an attractive choice for nanomechanical designs and mechanical reinforcement. Theoretical calculations[2-4] have suggested that DNRs are more brittle and stiffer than carbon nanotubes for radii greater than about 1-3 nm, depending on the orientation of the DNRs[2]. DNRs also have the lowest measured compressibility of any material[3]. It is also well known that diamond and CNTs have a high thermal conductivity, which would be expected for DNRs. DNRs may also be insulating, semi-metallic, or semiconducting depending on doping status, diameter, surface morphology and the degree of hydrogenation, suggesting that DNRs may have unique niche applications in nanoelectronics[4]. Novikov et al. [5] have confirmed with experiments and theoretical analysis that the thermal conductivity of polycrystalline DNR thin films will reduce as grain sizes approach the nanometer scale due to phonon scattering. Studies by Padgett, Shenderova and Brenner [6] suggested that DNRs should be useful for thermal management in nanocomposites, because the conductivity of DNRs is less sensitive to surface functionalization than modeling suggests for CNTs.

DNRs and related structures have been achieved experimentally using a number of techniques, including a top-down approach by etching diamond films[7-9], bottom-up CVD growth using templates[10, 11] and growth without spatial confinement[12-14]. The range of diameters for both polycrystalline and single-crystal DNRs can span several tens of nanometers. Molecular dynamics and first principle calculations have shown that diamond nanorods are energetically and mechanically viable structures[2, 3, 15].

Compared to the vast majority of research on carbon nanotubes (CNTs), there is a dearth of research on similarly one-dimensional DNRs, though they also hold promise for several important applications. Using literature *ab initio* data, Shenderova et al.[2] showed that DNRs would have smaller brittle fracture forces and zero strain stiffnesses than single walled carbon nanotubes for radii less than about 2-6 nm, depending on the orientation of the DNRs. For larger diameters, however, both brittle fracture forces and zero strain stiffnesses for DNRs are expected to be larger than those for CNTs. The authors also concluded that the binding energy of DNRs is similar to that for single walled CNTs, especially at large diameters, by comparing to the data for (17,0) single walled CNTs. Barnard et al.[16] investigated the morphologies of several DNRs with density functional theory calculations. It was concluded that the bare (111) surface undergoes partial graphitization in a way similar to the manner in which nanodiamond's bare (001) surface forms dimers under surface reconstruction, while the bare (011) surface largely preserves the diamond structure. The same classes of DNRs with hydrogen termination were found to keep the diamond surface morphologies

4.2 STABILITY OF NANORODS

To further explore the stability of these structures, molecular dynamics modeling using the REBO potential was used to calculate the heat of formation for structures that represent the six different morphologies as illustrated in Figure 4.1. These morphologies correspond to $\langle 001 \rangle$ and $\langle 011 \rangle$ principal axes and low-index facets.

The molar heats of formation of a compound (ΔH_f), a key property in thermochemistry, is the change of enthalpy that accompanies the formation of 1 mole of a substance in its standard state from its constituent elements in their standard states (the most stable form of the element at 101.325 kPa of pressure and the specified temperature, usually 298 K). It also is a key property to determine the relative stability of isomeric systems. For compounds, significant resources could be expended in synthesizing the material, only to discover upon measuring its ΔH_f that it is an unsuitable candidate for use. Therefore, computational tools have been developed as an alternative to predict this key property.

In our studies, all (001) surfaces were reconstructed to form dimers, and periodic boundary conditions were applied along the principal axis direction to create DNRs with infinite length. Theoretical heats of formation at 0 K were calculated by subtracting calculated atomization energies from known heats of formation of the isolated atoms[17]. Formation energies and preferred morphologies were calculated using the second-generation reaction empirical bond order (REBO) potential, a bond-order potential for hydrocarbons:

$$\Delta H_f^\circ(DNR) = N_C \cdot \Delta H_f^\circ(C) + N_H \cdot \Delta H_f^\circ(H) - E^{at} \quad (4.2.1)$$

or

$$\frac{\Delta H_f^\circ(DNR)}{N_C} = \Delta H_f^\circ(C) + \frac{N_H}{N_C} \cdot \Delta H_f^\circ(H) - \frac{E^{at}}{N_C} \quad (4.2.2)$$

where E^{at} is the atomization energy obtained from the simulations. $\Delta H_f^\circ(C)=7.40$ eV is the experimental atomic enthalpy of formation at 0 K for carbon gaseous atom from carbon standard state (graphite)[18] and $\Delta H_f^\circ(H)=2.239$ eV is the atomic enthalpy of formation for hydrogen gaseous atom from hydrogen standard state (H₂ molecule)[19].

The results shown in Figure 4.2 are the enthalpy of formation $\frac{\Delta H_f^\circ(DNR)}{N_C}$ for the DNRs as a function of the ratio $\frac{N_H}{N_C}$. For DNRs, the ratio $\frac{N_H}{N_C}$ is independent of its length and a decrease of the ratio $\frac{N_H}{N_C}$ corresponds to an increase of the DNR diameter. As the value of the ratio $\frac{N_H}{N_C}$ approaches to zero, the atomic enthalpy of formation for all DNRs comes to that for bulk diamond, which is about 0.025 eV in our simulations with the REBO potential. This value also demonstrates that the diamond is a metastable structure under ambient conditions. For comparison, the enthalpy of formation for a single walled (17,0) carbon nanotube with hydrogen termination at both ends is also plotted in the figure as a dotted line. Because of the inherent strain energies associated with a curved structure like CNTs, the converged enthalpy of formation for this CNT is not zero when $\frac{N_H}{N_C}$ approaches to zero, though CNTs are one-dimensional tubular analogues of graphite.

As the hydrogen-to-carbon ratio $\frac{N_H}{N_C}$ increases, that is, the diameter of DNRs

decreases, the behavior for different DNR morphologies is different. The morphologies represented by structures (a), (e), and (f) in Figure 4.1 become more stable, while the morphologies (b), (c) and (d) become less stable as the diameter approaches zero. The morphologies (a) and (f) are more stable than the (17,0) CNT, while the morphology (e) is less stable than the (17,0) CNT. Clearly, principal orientation or surface structure alone are not enough to determine the stability of DNRs, but rather the combination of the principal axis and surface orientation determine the energetic stability. Our simulation results for $\langle 011 \rangle$ DNRs are consistent with the experimental studies done by Sun et al.[14], who observed that the diamond nanorods grow along diamond $\langle 011 \rangle$ direction, and the calculation by Shenderova[2] based on *ab initio* data

4.3 SUMMARY

Molecular simulations using a heat of formation model with the REBO potential for the hydrogenated carbon nanorods showed that their stability is not only size dependent but also surface orientation and principal axis dependent. The simulation results indicated that the three DNRs with the combination of $\langle 001 \rangle$ and (011) as the structure in Figure 4.1 (a), $\langle 011 \rangle$ and (111) as the structure in Figure 4.1 (f), $\langle 011 \rangle$ and (001)/(111) as the structure in Figure 4.1 (e) are energetically stable structures when the diameter is less than 5.5 nm. In the other size range, the nanorods are metastable. In these three structures, the first two morphologies are more stable than (17,0) CNT with hydrogenate termination at both ends. The simulation results are also very useful in explaining the growth of nanorods from carbon nanotubes as discovered by Sun et al. [14]

4.4 REFERENCES

1. Shenderova, O.A., V.V. Zhirnov, and D.W. Brenner, *Carbon nanostructures*. Critical Reviews in Solid State and Materials Sciences, 2002. **27**(3-4): p. 227-356.
2. Shenderova, O., D. Brenner, and R.S. Ruoff, *Would diamond nanorods be stronger than fullerene nanotubes?* Nano Letters, 2003. **3**(6): p. 805-809.
3. Dubrovinskaia, N., et al., *Aggregated diamond nanorods, the densest and least compressible form of carbon*. Applied Physics Letters, 2005. **87**(8).
4. Shenderova, O.A., D.M. Gruen, and Knovel. *Ultrananocrystalline diamond synthesis, properties, and applications*. 2006.
5. Novikov, N.V., et al., *Influence of isotopic content on diamond thermal conductivity*. Diamond and Related Materials, 1999. **8**(8-9): p. 1602-1606.
6. Padgett, C.W., O. Shenderova, and D.W. Brenner, *Thermal conductivity of diamond nanorods: Molecular simulation and scaling relations*. Nano Letters, 2006. **6**(8): p. 1827-1831.
7. Baik, E.S., Y.J. Baik, and D. Jeon, *Aligned diamond nanowhiskers*. Journal of Materials Research, 2000. **15**(4): p. 923-926.
8. Zhang, W.J., et al., *Structuring nanodiamond cone arrays for improved field emission*. Applied Physics Letters, 2003. **83**(16): p. 3365-3367.
9. Ando, Y., Y. Nishibayashi, and A. Sawabe, *'nano-rods' of single crystalline diamond*. Diamond and Related Materials, 2004. **13**(4-8): p. 633-637.
10. Masuda, H., et al., *Synthesis of well-aligned diamond nanocylinders*. Advanced Materials, 2001. **13**(4): p. 247-+.
11. Yanagishita, T., et al., *Synthesis of diamond cylinders with triangular and square cross sections using anodic porous alumina templates*. Chemistry Letters, 2002(10): p. 976-977.
12. Chih, Y.K., et al., *Formation of nano-scale tubular structure of single crystal diamond*. Diamond and Related Materials, 2004. **13**(9): p. 1614-1617.
13. Kobashi, K., et al., *Fibrous structures on diamond and carbon surfaces formed by hydrogen plasma under direct current bias and field electron-emission properties*. Journal of Materials Research, 2003. **18**(2): p. 305-326.

14. Sun, L.T., et al., *Diamond nanorods from carbon nanotubes*. *Advanced Materials*, 2004. **16**(20): p. 1849-+.
15. Barnard, A.S., *Structural properties of diamond nanowires: Theoretical predictions and experimental progress*. *Reviews on Advanced Materials Science*, 2004. **6**(2): p. 94-119.
16. Barnard, A.S., S.P. Russo, and I.K. Snook, *Ab initio modelling of the stability of nanocrystalline diamond morphologies*. *Philosophical Magazine Letters*, 2003. **83**(1): p. 39-45.
17. Curtiss, L.A., et al., *Assessment of Gaussian-2 and density functional theories for the computation of enthalpies of formation*. *Journal of Chemical Physics*, 1997. **106**(3): p. 1063-1079.
18. *Synthesis, Properties And Applications of Ultrananocrystalline Diamond*. 2005: Kluwer Academic Pub.
19. Brenner, D.W., et al., *A second-generation reactive empirical bond order (REBO) potential energy expression for hydrocarbons*. *Journal of Physics-Condensed Matter*, 2002. **14**(4): p. 783-802.

FIGURES

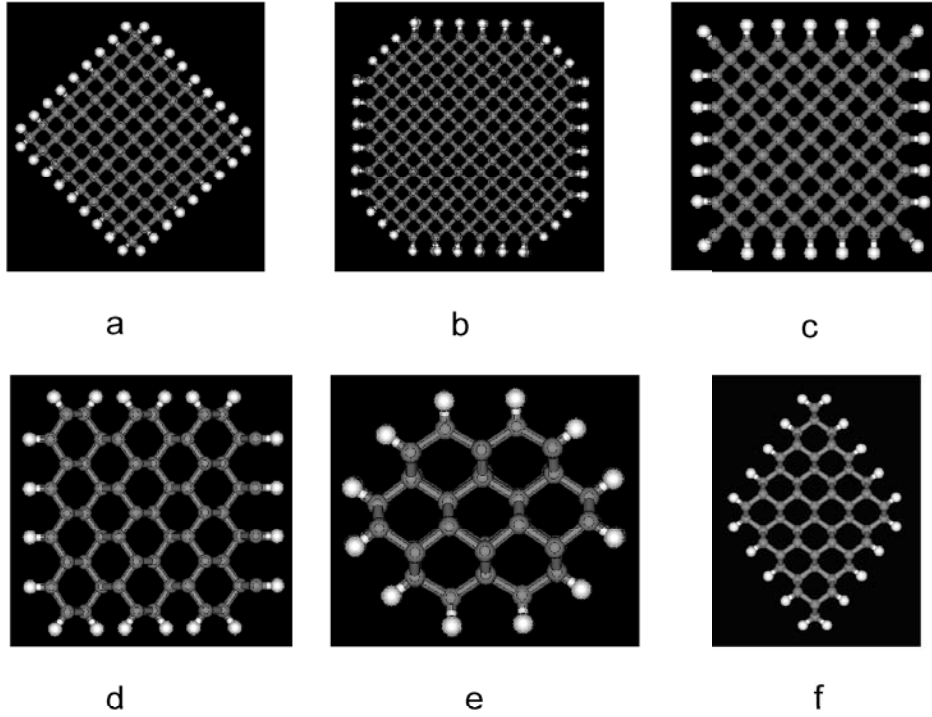


Figure 4.1 Representative structures from the set of DNR morphologies simulated. The top structures correspond to $\langle 001 \rangle$ orientation along the DNR axis; the bottom structures correspond to $\langle 011 \rangle$ orientations. Surface orientations for the top structures, left to right: (011) , (011) , and (001) , (001) . Surface orientation for the bottom structures, left to right (011) and (001) , (001) and (111) , (111) .

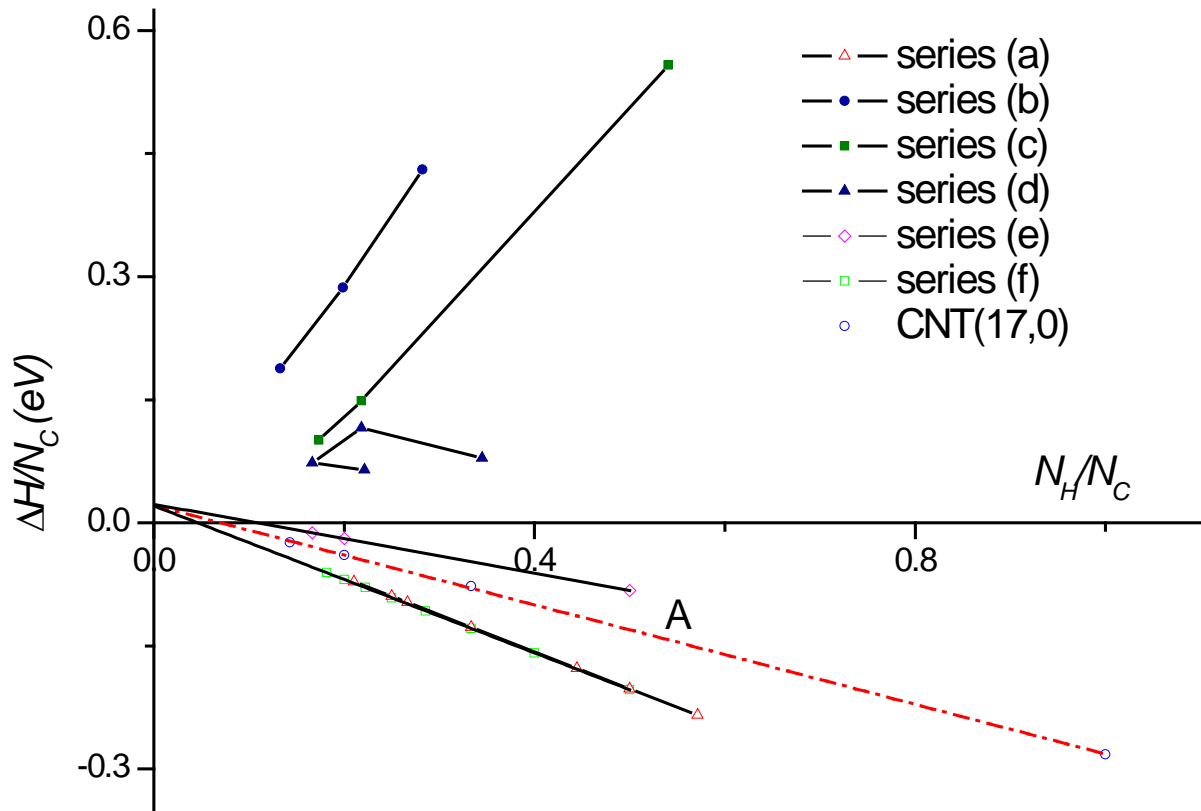


Figure 4.2 Atomic enthalpy of formation versus the hydrogen-to-carbon ratio for DNRs of infinite length (via a periodic boundary) corresponding to the different morphologies represented in Figure 4.1

CHAPTER 5. GLASS TRANSITION OF POLYETHYLENE- NANODIAMOND COMPOSITES

5.1 INTRODUCTION

Amorphous polymers are widely used in industry. Usually, they are blended with different fillers in practical applications for temperature stability, mechanical properties, optical properties and processability. To create polymer composites with a set of desired properties, the physics underlying the material behavior needs to be understood and characterized. Understanding the nature of the glassy state and glass transition is one of the long-standing problems of materials science and physics. Varieties of experimental techniques are utilized toward this end and various macroscopic properties around and below the glass transition temperature have been extensively investigated.[1-3] Molecular dynamics (MD) simulation has emerged as a powerful technique for investigating the glass transition from a molecular point of view, and in a short time scale range, i.e. from $\sim 10^{-14}$ to $\sim 10^{-8}$ s. The recent development of nanotechnology and the need for new materials modified with nanoparticles have driven an increased interest in understanding the structural and dynamic properties of nanocomposites on the molecular level. MD simulation can provide an excellent opportunity to directly study the influence of nanoparticles on the structure and dynamics of polymers. In our study, MD is used to investigate the glass transition of polyethylene composites embedded with nanodiamond particles.

5.1.1 SURVEY OF GLASS TRANSITION THEORY AND COMPUTATIONAL APPROACHES

Understanding the nature of the glassy state and its transition is one of the most important problems for polymers scientists both for practical and theoretical reasons. A variety of theoretical explanations based on experimental results have been developed since the 1950's, which include kinetic, phenomenological and thermodynamic, to explore the nature of the glassy state of polymers.

In the kinetic regime, the glass transition temperature, T_g , is interpreted as the temperature at which large-scale cooperative mobility of the polymer matrix occurs, or, alternatively, where the thermal expansion coefficient, α , changes from the rubbery to the glassy state, with its value being dependent on the rate at which data are measured. The secondary, or β transition, associated with limited molecular mobility below T_g at a temperature T_β , is a broad relaxation process. This process is believed to correlate with side chain rotations (such as the wagging of a phenyl unit in polystyrene), the motion of a small number of monomeric units in the main chain and short chain portions. The relaxations characterized by both T_g and T_β represent a distribution of relaxation times. Traditionally, experiments used to measure the glass transition temperature are carried out under isobaric conditions, during which the volume varies with temperature. Consequently, the volume change has been regarded as the most important factor in explaining glass formation process. Among various kinetic models, the free volume theory, which was first proposed by Fox and Flory[4], and further applied by Simha and Boyer[5], is the most widely accepted one.

The free volume, V_f , is defined as the unoccupied space in a sample, arising from the inefficient packing of disordered chains in the amorphous regions of a polymer sample. The available unoccupied space surrounding a particle (molecule) plays a key role in determining the mobility of the particle (molecule). This theory has been successfully applied to hydrocarbon liquids. When the polymer is in the liquid or rubber-like state, the free space will increase with temperature as the molecular motions increase. If the temperature decreases, the free space will decrease and eventually reach a critical value where there is not sufficient free space to undergo large-scale segmental motion. The temperature where this critical volume is reached is the glass transition temperature. Below the T_g , the free volume will remain almost constant as the temperature decreases further, since the chains have been immobilized and frozen in position. In other words, the glass transition can be visualized as the onset of segmental motion, made possible by the increase of the free space surrounding the particle (molecule) to the size sufficient to undergo this type of motion.

Williams, Lendel and Ferry[6] found an empirical equation (WLF equation) that expresses, after a suitable choice of reference temperature, T_s , the ratio α_T of all mechanical and electrical relaxation times at temperature T to their values at T_s by the equation $\log \alpha_T = -8.86 (T - T_s) / (101.6 + T - T_s)$ over a T range of $T_s \pm 50$ (K). This applies to a wide variety of polymers, polymer solutions, organic glass-forming liquids, and inorganic glasses. As chosen, T_s lies about 50 (K) above the glass transition temperature, T_g . If, alternatively, the reference temperature is chosen as T_g , then the expression becomes $\log \alpha_T = -17.44 (T - T_g) / (51.6 + T - T_g)$. Doolittle[7] and WLF[6] explained this

empirically in terms of the free volume, and predicted that a rapid increase of viscosity associated with an decrease of free volume as T_g is approached.

In the thermodynamic regime, Gibbs and DiMarzio[8] proposed that the glass transition is a second order phase transition (G-D theory). They employed a statistical-mechanical quasi-lattice theory to calculate the configurational function on on the chain stiffness and the volume changes with temperature. They consider the fundamental transition to be a true equilibrium. Many experiments imply that the observed T_g would decrease further if a sufficiently long time for measurement was allowed. This aspect is considered in the G-D theory by defining a new transition temperature, T_2 , at which the configurational entropy of the system is zero. This temperature can be considered in effect to be the limiting value T_g would reach in a hypothetical experiment taking an infinitely long time. The theoretical derivation is based on a lattice treatment. The configurational entropy is found by calculating the number of ways that n_x linear chains, each x segments long, can be placed on a diamond lattice (coordination number, $Z = 4$), with n_0 unoccupied holes. The restrictions imposed on the placing of a chain on the lattice are embodied in the hindered rotation which is expressed as the “flex energy,” δ_ϵ , and, ϵ_h , the energy of formation of a hole. The flex energy is the energy difference between the potential energy minimum of the located bond and the potential minima of the remaining $(Z-2)$ possible orientations that can be used on the lattice. The quantity ϵ_h is a measure of the cohesive energy. The configurational entropy, S_{conf} , is derived from the partition function describing the location of holes and polymer molecules. As the temperature drops to T_2 , the number of available configuration states in the system

decreases until the system possesses only one degree of freedom. The temperature, T_2 , is not an experimentally measurable quantity, but is calculated to lie approximately 50 K below the experimental T_g , and can be related to T_g on this basis.

An attempt to unite the kinetic and dynamic theories was made by Adam and Gibbs (who outlined the molecular kinetic theory). They relate the temperature dependence of the relaxation process to the temperature dependence of the size of a region, which is defined as a volume large enough to allow cooperative rearrangement to take place without affecting a neighboring region. This “cooperatively rearranging region” is large enough to allow the transition to a new configuration, hence it is determined by the chain configuration, and by definition will equal the sample size at T_2 , where only one conformation is available to each molecule. The polymer sample is described as an ensemble of cooperative regions, or subsystems, each containing Z monomeric segments. The transition probability of such a cooperative regions is then evaluated as a function of its size to be

$$W(T) = A \exp(-Z\Delta\mu/KT) \quad (1.1.1)$$

where $\Delta\mu$ is the activation energy for a cooperative rearrangement per monomer segment. This can be approximately expressed in the WLF form.

While these models are somewhat successful in terms of understanding the glass transition process, they are not capable of predicting the glass transition temperature dependence of chain length, side chain, polarizability, etc. Understanding these dependencies are very important in terms of designing various exotic polymer materials. Despite extensive experimental efforts, the glass transition phenomena of polymers are still not fully

understood. Questions persist because of the inability to access the molecular level information to characterize the molecular motion and structural changes with current experimental techniques.

5.1.2 MEASUREMENT OF FREE VOLUME

Experimentally, the annihilation of positrons and the kinetics of isomerization of probe molecules are used to measure the free volume; however, these techniques are laborious and involve some ambiguities in interpreting the result quantitatively. Computational modeling provides an alternative method for the free volume evaluation. The method will enable new types of “measurements” to be performed to evaluate properties of glasses that conventional laboratory experiments cannot easily provide. Roe and co-workers[9] have performed extensive research on the study of glass transition in small alkane molecules and polyethylene systems. The results show that molecular simulations could capture the detailed structural information on the molecular scale and the nano-second time scale. They found that the internal energy changes abruptly at T_g . These simulations also provide an insight into the molecular scale during the glass transition, such that the conformational transition rate and the segmental diffusion coefficient vanish under T_g . Brown and Clarke[10] also showed that the torsional energy of the polymer systems is constant below T_g . This result demonstrated that the freezing torsional degrees of freedom are closely related to glass transition phenomena. In other words, more detailed knowledge about glass transition can be obtained by using numerical simulation techniques compared to experiments.

Free volume theory is also widely used to explain the behavior of glassy materials and the glass transition phenomena in computational dynamics simulation. There is, however, no unique quantitative definition of free volume accepted by all the researchers. The free volume is often defined according to the need to interpret a particular phenomenon under consideration. Similarly, there are a number of different approaches to evaluate of the free volume from molecular models, three of which are most widely used. In the first approach, the atoms are replaced by hard spheres of van der Waals radius or some similarly defined radius. Any space not covered by any of these overlapping hard spheres is then considered as free volume. Here, a correct choice of the hard-sphere radius is important. Whether the radius is to depend on temperature (to allow for vibrational amplitudes varying with temperature) is a difficult choice to make. In the second approach, the technique of Voronoi tessellation of a space is utilized. The space is subdivided into space-filling convex polyhedra surrounding each atom. Given the positions of atomic centers, Voronoi polyhedra are unambiguously defined, and the distribution of free volume can be evaluated by reference to the size distribution of these polyhedra, thus circumventing the issue of the correct atomic radius to use. In the third approach, the free volume, v_f , surrounding an atom i is defined by

$$v_f = \int \exp[-\phi_i(r)/kT + \phi_i(r_0)/kT] dr \quad (4.1.2)$$

where $\phi_i(r)$ is the potential energy that would act on atom i , if it is placed at position r while keeping all the surrounding atoms at their respective positions, and r_0 is the position of the local potential energy minimum. The above definition, originally developed for analysis of monatomic liquids, needs modification for the study of polymer liquids in view of

the presence of covalently bonded neighbors along the chain.

5.2 SIMULATION DETAILS AND SAMPLE PREPARATION

There are mainly two categories in terms of atomic-level simulations, Monte Carlo (MC) and molecular dynamics (MD). Of the two methods, MD is potentially the more useful one since it can provide information on the time evolution of a system as well as its time-averaged properties, thus allowing the study of many kinetic aspects of the glassy state. Both MC and MD methods have been applied to the study of glass formation of simple liquid systems. Although some questions still remain as to the validity of these studies, mainly because of the very short duration of simulation - usually nano-scale, in comparison to the laboratory experiments - they have nonetheless found wide use and have provided many useful insights into the nature of the glassy state. In our study, the MD simulation with a united-atom model was applied to examine glass transition phenomena of polyethylene and its composites with nanodiamonds.

5.2.1 POTENTIALS

A united-atom is a particle that incorporates a group of atoms but can approximately represent the molecular properties of the group on a size scale that is larger than the atomic scale. The united-atom model is a good approximation to simulate molecular systems in which the intermolecular motion is much more important than the intramolecular motion, or the intramolecular motion is much less significant than the intermolecular motion. In our study, a united-atom model was employed to describe individual polymer chains, in which

each CH₂ or CH₃ group is considered as a single interaction unit to avoid high-frequency vibrations of the C-H bonds without losing the information of chain dynamics, since the intrachain covalent bond potential is, by far, the stiffest interaction in polymers. Individual chains are modeled as sequences of spherical “segments” as illustrated in Figure 5.1.

The intra-polymer potential by Clarke et al.[11] has been used to describe interactions within a polymer chain. This potential has two components: a valence angle potential and a torsion potential. The valence angle potential is described as

$$\Phi(\theta)/J \cdot \text{mol}^{-1} = \frac{1}{2}k_{\theta}(\cos \theta - \cos \theta_0)^2 \quad (5.2.1)$$

where $k_{\theta} = 520J \cdot \text{mol}^{-1}$, $\theta_0 = 112.813^\circ$, and the torsion potential is described as

$$\Phi(\alpha)/J \cdot \text{mol}^{-1} = C_0 + C_1 \cos \alpha + C_2 \cos^2 \alpha + C_4 \cos^3 \alpha \quad (5.2.2)$$

where $C_0=8,832 J \cdot \text{mol}^{-1}$, $C_1=18,087 J \cdot \text{mol}^{-1}$, $C_2=4,880 J \cdot \text{mol}^{-1}$, and $C_4=-31,800 J \cdot \text{mol}^{-1}$. In general, the C-C bonds in a polymer chain are typically kept rigid to allow large MD times steps during the simulations. However, we have allowed full dynamics of these bonds, to be consistent with the dynamics of C-C bonds within CNTs. A harmonic potential described as

$$\Phi(l)/J \cdot \text{mol}^{-1} = \frac{1}{2}(l - l_0)^2 \quad (5.2.3)$$

is used for the dynamics of C-C bonds within a chain, where $k_b = 346J \cdot \text{mol}^{-1}/\text{\AA}^2$, and $l_0 = 1.53 \text{\AA}$ [9]. Truncated 6-12 LJ potentials as described in Eqn (5.2.4)

$$\Phi(r_{ij})/J \cdot \text{mol}^{-1} = \begin{cases} 4\epsilon \left[\left(\frac{\sigma}{r_{ij}} \right)^{12} - \left(\frac{\sigma}{r_{ij}} \right)^6 \right] & \text{for } |r_{ij}| \leq r_{cutoff} \\ 0 & \text{for } |r_{ij}| \geq r_{cutoff} \end{cases} \quad (5.2.4)$$

are applied to pairs of units that are apart by more than three units with $\epsilon_{CH_2-CH_2}=0.498$ KJ \cdot mol⁻¹ and $\sigma_{CH_2-CH_2}=3.95$ Å. The interactions of the carbons within octahedral diamond particles are described with harmonic bond potential as described in Eqn (5.2.3) with $k_l=2848.879$ KJ \cdot mol⁻¹, and $l_0=1.53$ Å, and harmonic angle potential as described in Eqn (5.2.1) with $k_\theta=250.8$ KJ \cdot mol⁻¹ and $\theta_0 = 109.4^\circ$. Truncated 6-12 LJ potentials are also applied to pairs of units that are apart by more than three units with $\epsilon_{C-C}=0.4255$ KJ \cdot mol⁻¹ and $\sigma_{C-C}=3.37$ Å

For the bond connection between polymer chains and nanodiamond particles, the harmonic potential is used whose parameters are derived using the Lorentz-Berthelot mixing rules[12],

$$k_l^H = [k_l^P \cdot k_l^C]^{\frac{1}{2}} \quad (5.2.5)$$

$$l_0^H = \frac{1}{2} (l_0^P + l_0^C) \quad (5.2.6)$$

where k_l^P and l_0^P are the harmonic bond potential parameters for polymers and k_l^C and l_0^C are the harmonic bond potential parameters for carbon nanodiamond. For the long distance interaction between the united atoms of the polymer chains and the carbon atoms of nanodiamond, the Lorentz-Berthelot mixing rules[12] are again applied,

$$\sigma_{C-CH_2} = \frac{1}{2} [\sigma_{C-C} + \sigma_{CH_2-CH_2}] \quad (5.2.7)$$

$$\varepsilon_{C-CH_2} = [\varepsilon_{C-C} + \varepsilon_{CH_2-CH_2}]^{\frac{1}{2}} \quad (5.2.8)$$

For the composite systems, we have considered six nano-diamond particles as fillers embedded in the polyethylene matrix because of their potential promising reinforcement and/or toughening characteristics for the polymers. The cutoff radius, $r_{cutoff}=12 \text{ \AA}$, is used in our simulation.

The *trans* state of the dihedral angle, where $\phi = 0^\circ$, gives the lowest torsional potential energy; and the *gauche* state, where $|\phi| = 112^\circ$, is a metastable state with a potential energy of $4.42 \text{ kJ} \cdot \text{mol}^{-1}$; there is a potential barrier of $15.12 \text{ kJ} \cdot \text{mol}^{-1}$ at $|\phi| = 60^\circ$. These potential features play important roles in the glass transition, as discussed below. In the analysis presented here, we consider a bond triplet to be in *trans* orientation when the absolute value of ϕ is less than 60° . Newton's equations of motion for all the united atoms were numerically solved using leapfrog algorithm with 1 MD step = 1 fs.

The first one of the aforementioned three free-volume analysis schemes is applied in our study, as illustrated in Figure 5.2. To evaluate the free-volume, the configurations of the systems were analyzed by replacing each segment with a sphere of diameter $D = 0.8r^*$ (r^* is the *Van der Walls* diameter); then, the systems were divided into $0.3 \times 0.3 \times 0.3 \text{ \AA}$ cubic cells, each of which was labeled as unoccupied whenever less than half of its volume lay within one of the spheres of diameter, D . The free volume was calculated by summing the unoccupied cubic cells. The unoccupied cubic cells were labeled as connected if these cells could reach each other via unoccupied cells; otherwise, they were labeled as disconnected. The hole volume was then evaluated.

5.2.2 SAMPLE PREPARATION

The thermal history of polymers and composites is important in determining their properties and structures. Before conducting the cooling simulation, a series of high temperature, liquid samples must be prepared and relaxed for certain times. The mobility of the polymer chain is much smaller compared to the small molecule systems, even at high temperatures, and only a small portion of conformational phase space can be reached during the courses of a typical MD simulation. Therefore, the initial structures of the polymers and composites systems is critical to the cooling process. Two of the initial pure pristine structures were obtained using the amorphous polymer model in Material Studio from Accelrys, with fixed bonded length $r = 1.53 \text{ \AA}$ and density 0.95 g/cm^3 at 600K, which is well above the glass transition temperature for bulk polyethylene. Another initial pure pristine structure was grown by crossing the straight polymer chains layer by layer in a huge box first, relaxing for 2 ns, and then shrinking the size of the box to get desired density, 0.95 g/cm^3 at 600 K.

Following these initial structures, relaxation within an NVT ensemble was carried out. The non-bonded LJ interaction was not fully switched on during this stage because of the high energies and large forces associated with these initial structures, which could lead to numerical instabilities in the MD program. To avoid this, a softened LJ potential, whose zero potential distance σ was increased slowly to its normal value, was employed to introduce the approximate excluded volume into the system after about 200,000 MD steps. At the same time, the LJ non-bonded interaction was fully turned on and the extremely large internal

pressure associated with the initial structures was effectively reduced during this relaxation. These samples were further relaxed by holding at a pressure of one bar and a temperature of 600 K for about 1 nanosecond within an NPT ensemble. The system volumes quickly equilibrated and then fluctuated around the equilibrium value.

After the pristine matrix was fully relaxed, a dummy atom was randomly embedded into the matrix. A softened non-bonded LJ interaction between the dummy atom and all other atoms in the matrix was employed to slowly introduce the appropriate excluded volume around the dummy atom to hold a nanodiamond by slowly increasing the zero potential distance σ in LJ potential (see Eqn (5.2.4)). A nanodiamond-polyethylene composite system was generated by replacing the dummy atom with a nanodiamond particle. By repeating this procedure, a composite system with different nanodiamond density could be generated. This sample was further relaxed by holding at a pressure of one bar and a temperature of 600 K for 1,000,000 MD steps within an NPT ensemble, so that the system could effectively track the target pressure. This sample was the starting structure of the polyethylene-nanodiamond composites without crosslinks between polyethylene and NDs.

Based on the distance between carbon atoms in NDs and CH₂ unit atoms in polyethylene chains, some extra bonds, which connect the carbon atoms at the ND surface and their corresponding nearest CH₂ neighbor, were manually constructed. The initial bond length of these manually constructed bonds was larger than C-C bond lengths at equilibrium. A harmonic bond potential with equilibrium bond length equal to the initial bond length and decreasing by 0.01 Å every 5 ps until reaching equilibrium length 1.53 Å was introduced for

these manually constructed bonds during relaxation. The sample was further relaxed by holding a pressure of one bar and a temperature of 600 K for 1,000,000 MD steps within the NPT ensemble so that the system could effectively track the target pressure after the bond length of all manually constructed bonds reached 1.53 Å.

Samples under other isobaric conditions ($P=100$ bar) were prepared by gradually increasing the pressure of the 1 bar pressure samples at a constant rate, while keeping the temperature fixed at 600 K. This was accomplished within the NPT extended ensemble MD method by increasing the target pressure P_{ext} at a rate of $dP_{ext}/dt = 1 \times 10^{-3}$ bar/ps. After reaching the target pressure, the samples were allowed to further relax at 600 K at this pressure for 1,000,000 MD steps (1 nanosecond).

Samples with short chain lengths were prepared by cutting long chain in samples prepared previously and removing the parts no longer needed, and then equilibrating with NPT ensemble for 1,000,000 MD steps to reach the desired temperature and pressure.

All other samples were prepared with the methods described above. The samples used in our studies were listed in Table 5.1 and their snapshots at 600 K were illustrated in Figure 5.3.

To identify the effect of the nano particles on the initial structure, the radial distribution functions $g(r)$ for two systems, (a) system with 12 NDs and 97x200 polyethylenes and (b) system with 12 NDs and 97x40 polyethylenes, at 600 K and 1 bar are shown in Figure 5.4. As seen from Figure 5.4 (a), there is a gap between the curves for the composites and pure pristine system because the introduced NDs change the density profile

in the pristine system. No obvious difference between the two composite curves for the system with 12 NDs and 97x200 polyethylenes is observed, since the percentage of extra bonds in this system is relatively small. However, a relatively big difference between the two composite curves for the system with 12 NDs and 97x40 polyethylenes is observed, because of the relatively high percentage of extra bonds in this system. The extra bonds retard the movement of the polymer chain and introduce vacancies around the bonds, which make the composite with crosslinks denser than one without crosslinks, as shown in a later section (in Table 6.7)

5.2.3 SIMULATION DETAILS

Since the glass transition is a kinetic process, the path the system traverses is important in determining the structure of the glass and the nature of the glass transition. We employ Berendsen's loose coupling constant pressure molecular dynamics to control the system pressure and temperature[13]. The Hamiltonian of the dynamics is

$$H = H_{part} + H_{ber} + H_{stress} \quad (5.2.9)$$

where the H_{part} describes the ordinary Hamiltonian for the N particles, H_{ber} describes the temperature bath, and H_{stress} describes the stress bath. The method considers a coupling of a system to an external bath with fixed reference temperature T_0 . This coupling is realized by the modified Langevin equation

$$m_i v_i = F_i - m_i \gamma \left(\frac{T_0}{T} - 1 \right) v_i \quad (5.2.10)$$

The detailed NPT MD equations of motion, which dynamically control the system temperature and pressure at the specified value T_{ext} and P_{ext} , were derived by Berendsen in reference [13] and realized in the molecular simulation package DL_POLY[14]. By decreasing the target temperature T_{ext} with a fixed rate, isobaric cooling at fixed dT_{ext}/dt is achieved, under the assumption that the simulation system can rapidly adjust to the changes in T_{ext} . For the value of dT_{ext}/dt employed in the present simulations (2×10^{-4} degrees per MD time step), the system temperature and T_{ext} accurately and promptly track each other. For the polyethylene-NDs composite systems, T_{ext} and T_{int} (system internal temperature) for the complete cooling procedure are illustrated in Figure 5.5. With this cooling rate, the temperature can be reduced from 600 K to 75 K in about 3.2×10^6 MD time steps (about 3.2 nanoseconds). Performing similar simulations at higher cooling rates yielded no qualitative changes in the glass behavior, but did lead to slightly different glass densities. The parallel numerical algorithm employed in our study to integrate the equations is described in detail in the DL_POLY_2.0 Manual[14]. The time step used in our study is $dt = \tau = 1$ fs.

Accurate determination of the pressure is critical for the isobaric glass formation studies. In a molecular system, the pressure can be calculated based upon either molecular or atomic units. The average value of the pressure calculated using these two methods should be same. This equivalence has been demonstrated by Berendsen[13]. However, the instantaneous values of the pressure calculated with these two approaches are not necessarily the same. In our simulation, the pressure has been calculated using the molecular approach by summing the following expression over all N united atoms.

$$P = \frac{1}{V} \sum_{i=1}^N \left[\frac{1}{m_i} p_i p_i + r_i f_i \right] \quad (5.2.11)$$

where V is the system volume and m_i , p_i , r_i , and f_i are the mass, momentum, position, and force on the i th site, respectively. Periodic boundary conditions are employed in all three directions in the present simulations.

It is also essential that the interval ΔT of data collection points not be so large as to trap the configuration in a metastable state. After considering various values for ΔT , we found $\Delta = 25$ K to be satisfactory. In other words, we run an equilibrium simulation with fixed temperature for 100ps to collect data at every 25 K decrease in temperature during the whole cooling procedure. Figure 5.13 shows the unit cell volume fluctuation during dynamics at various temperatures.

The DL_Poly[14] MD simulation package was used and adapted to simulate the cooling procedure and the crosslinks between polyethylene chains and NDs in our study.

5.3 RESULTS AND DISCUSSIONS

The specific volume, v , versus temperature, T , for the samples studied in our research are presented in Figs 5.6-5.11, where some curves for the composite system are shifted on the vertical axis for clarity. At both high and low temperatures, the specific volume decreases linearly with decreasing temperature for both pressures, albeit with a smaller thermal expansion coefficient at low temperatures than that at high temperatures. The abrupt change in the thermal expansion coefficient is a classic signature of the glass

transition. To determine the glass transition temperature T_g , and glass formation volume v_g , a least square linear fit to the form $v = aT + b$ is made for the data at temperature well above and below T_g . The intersection of the high and low temperature linear fits is taken as T_g . The temperature range for the linear fitting and the fitting coefficients for each sample are represented in Table 5.2 - Table 5.7, in which the subscript "r" indicates the parameter for the rubbery state, and the subscript "g" the glass state. The specific volume for the system with long polyethylene chains is similar to the experimental value of amorphous PE, extrapolated from densities of the semi-crystalline PE. This demonstrated that the cooling rate employed in our MD simulation is reasonable.

Several important observations can be made based on the Figs 5.6-5.11. First, the systems with long polymer chains are not as sensitive as those with short polymer chains to pressure and fillers. Second, the glass transition temperature T_g increases and the glass formation volume v_g decreases with increasing pressure. Third, the slope of the specific volume versus temperature in the rubbery state, α_r , decreases with increasing pressure. The linear curve fits from the rubbery state at different pressures all extrapolate to about the same specific volume for the same system. Fourth, the slope of specific volume versus temperature in the glassy range, α_g , decreases with increasing pressure, although this is much weaker than in the rubbery state. Fifth, the longer the polymer chain in the system, the higher the glass transition temperature. Sixth, the glass transition temperature increases with the increasing volume percentage of nanodiamonds. As suggested by *Colucci et al.[15]*, the ratio of the slopes of the specific volume versus temperature lines for the rubbery and glassy states,

a_r/a_g , provides a measure of the glass transition strength. The data in Table 5.2 - Table 5.7 show that the glass transition strength in the present simulation decreases with increasing pressure. Finally, we note that the data in Figs 5.6- 5.11 near T_g lie above the intersection of the extrapolation of the high and low temperature data. This, too, is consistent with the experimental observations (see, e.g. Chap. 1, Figure 3 of Ref. [16]). All these observations demonstrate that the MD simulations can capture the experimental trends in glass transition behavior under isobaric conditions.

Above T_g , the polymer melt is in either equilibrium (above T_m), or a deep metastable state ($T_g < T < T_m$). When the melt is cooled below T_g , its mobility rapidly decreases, and the departure from equilibrium becomes increasingly severe. This picture is reflected by the observations made with respect to Figs 5.6- 5.11. The observation that the specific volume simulation data lie above the high and low temperature extrapolations near T_g is a result of the fact that, as the system nears T_g , the freezing out of configurational degrees of freedom prevents the system from keeping up with the evolving thermodynamic state. The high rate cooling in the MD simulations accentuates this effect. As the pressure is increased, this deviation becomes even more pronounced due to the fact that the relaxation rate slows with increasing density. This picture is reflected in the fact that the slope at rubbery at high pressure usually is smaller than that at low pressure.

The size of the nanodiamond used in our study is about 4 nm, which is smaller than the gyration radius of the polymer with the long chain length and at the same level as that for short chain length, as shown in Figure 5.12. If the filler size is smaller than the characteristic

size of the polymer, they cannot considerably reduce the mobility of the polymer chains. Table 5.8 shows the effect of nanodiamond on the diffusion coefficient of long/short chains at 600 K. It is seen that the diffusion coefficient is strongly reduced in the presence of filler for a short chain. However, the effect can be easily overwhelmed if the filler density is low. The data in Table 5.8 also shows that the chain length has a big effect on the diffusion coefficient; this is, the longer the polymer chain length, the smaller the diffusion coefficient.

Based on our observation and analysis with simulation data, there is similar behavior if chain length and filler density are comparable at the same pressure. To save space, we took the sample group with 12 NDs and 97x200 polyethylenes as our example in the following analysis. For the $\Delta T=25$ (K), $\tau_{equil}=100$ (ps) runs, by using the equilibrated portion of the dynamics at each temperature, we obtain the average volume as a function of temperature $V(T)$, as in Figure 5.13, which depicts a pristine unit cell volume versus dynamics time. The volume fluctuation is

$$\langle \delta V^2 \rangle = \langle V^2 - \bar{V}^2 \rangle \quad (5.3.1)$$

where

$$\bar{V} = \langle V \rangle \quad (5.3.2)$$

The average volume fluctuation is related to compressibility $\beta(T)$ by

$$RT\beta(T) = \frac{\langle \delta V^2 \rangle}{\bar{V}} \quad (5.3.3)$$

Fig. 5.14- 5.16 show that $RT\beta(T)\bar{V}$ curves have kinks near the glass transition temperature. Figure 5.17 shows the compressibility for the two groups of pure samples with short chains (length 40) and long chains (length 200) as a function of temperature. It is seen that the sample with short chain has a larger compressibility since the sample with the short chain has more free volume as we will show in the next section. Figure 5.18 and Figure 5.19 show the average, $\bar{R}_{end-end}(T)$ and $\bar{R}_{gyration}(T)$ as a function of temperature. The $\bar{R}_{end-end}(T)$ is obviously larger than the ND size, which is a leading cause that embedded nano-sized particles would not change the glass transition temperature of polymer system. The $\bar{R}_{gyration}(T)$ for both composites is larger than that for pure polyethylene, since the NDs will reduce or block the movement of polymers, which leads to a more straight polymer chain.

Some energy components versus temperature for the sample are shown in Figure 5.20, Figure 5.21 and Figure 5.22, which may help separate the roles played by the different interacting components in the glass transition. Soldera[17] reported small breaks in the plots of total, intramolecular, and intermolecular potential energies versus temperature in the simulation of the glass transition of PMMA. Fried, et al.[18] showed that a plot of internal energy versus temperature had a small break near the glass transition temperature. In our study, we find that there are small breaks in the plots of torsion energy and non-bonded energy versus temperature. The torsional and non-bond energy decreases linearly with decreasing temperature above T_g and also decreases linearly with temperatures, albeit with a smaller slope below T_g . The abrupt change in slope of LJ energy with temperature at T_g is

also very similar to the temperature dependence of the torsional energy. This observation suggests that there is a strong coupling between the volume change and freezing of the torsional degree of freedom at T_g . As the system contracts during cooling, the chains get closer and closer until there is not enough space to allow torsional state changes to occur. Therefore, the glass transition occurs apparently because of the volume change, which leads to the freezing out of the torsional degrees of freedoms and a decreased dV/dT below the glass transition temperature T_g . For other energy components such as bond energy and angle energy, they decrease linearly with decreasing temperature and there are no noticeable breaks at the glass transition temperature in the plots, which suggests that these degrees of freedom are in equilibrium both in the rubbery and glassy states.

The local segmental dynamics of a polymer chain have an important influence on the properties of polymers. An important factor concerning the structure of polymers is the dihedral distribution change while the polymers are cooling down below the glass transition temperature. The conformational transition rate and the transition correlation are mostly used to characterize the local segmental dynamics.[18] Above T_g , the thermal fluctuations are sufficient to allow the conformational fluctuations and equilibration of the torsional degrees of freedom; below T_g , conformational fluctuations do not occur at a sufficient rate to equilibrate these degrees of freedom.[19] Around the glass transition temperature, the behavior of the conformational transition was found to be different in different MD investigations. Rigby[9] found the conformational transitions almost ceased just above T_g for the *n*-alkane-like systems with short chains. Takeuchi found that for the long chain systems

the transitions existed even below T_g [20]. It was found that the conformational transition rate follows an Arrhenius temperature dependence with an activation energy that is close to the torsional barrier. At high temperature, the relaxation time characterizing the torsional angle autocorrelation function also shows an activation energy approaching the torsional barrier. But the activation energy becomes high at lower temperatures in a Williams-Landel-Ferry or Vogel-Fulcher fashion. Those results indicate that the conformational transition rate can be used to describe the glass transition. In our study, the dynamics of structure and dihedral angle for C-C-C-C of polymer chains were saved in a trajectory file to analyze the conformational transformations every 0.2 ps. We classify each dihedral angle in polymer chains in terms of:

- i. Stable conformations: $T(\phi = 180 \pm 30^\circ)$, $G^+(\phi = 60 \pm 30^\circ)$, $G^-(\phi = 300 \pm 30^\circ)$, and
- ii. Transitional conformations: $GT^+(120 \pm 30^\circ)$, $GT^-(240 \pm 30^\circ)$, and $G^+G^-(0 \pm 30^\circ)$

The transition state and the conformational state are illustrated in Figure 5.23. A transition is counted for each case where a dihedral changes between two stable configurations, separated only by the corresponding transitional conformation. The occurrences of transitions versus temperature are plotted in Figure 5.24. There are no transitions for $T < 200$ K and an increasing rate of GT transitions for $T > 300$ K. The glass transition temperature can be understood as the temperature above which conformational transitions are sufficiently fast that the molecule attains conformational equilibrium (a

viscous liquid), but below which the inter-diffusion of polymer chains is too slow for the system to equilibrate. The conformational relaxation is directly related to the rate of dihedral angle transitions, which in turn depends on both the rotational energy barrier, and on how closely the polymer chain is packed in the periodic cell, as we can see in the next section. By fitting the occurrences of transitions versus temperature to Arrhenius form as

$$k_{GT} = A_{GT} \exp \left[-\frac{E_{GT}^{act}}{RT} \right] \quad (5.3.4)$$

we can get the activation energy for GT transition in amorphous polyethylene and composites. The activation energy is about 5.15 kcal/mole for all three systems, which is consistent with the glass transition temperature of about 355 K for all three systems. Though the difference of the activation energy is small, the conclusion still can be drawn that the glass transition temperature increases with increasing activation energy.

The free volume analysis is performed, as stated in Potentials, by prescribing a sphere of diameter D on every segment center, and then evaluating the space not occupied by any of these spheres. Figure 5.26 illustrates the variation with temperature of the free volume, which is obtained by averaging over the whole 100 ps equilibrium at every 25 K temperature decrease, and Figure 5.27 shows ΔV_{free} as a function of temperature. Both have a characteristic change in slope around the glass transition temperature T_g , which shows that the glass transition is a second order phase transition as described by G-D theory. Further analysis of the free volume distribution shows that it exhibits a broad size distribution (0.027 \AA^3 to 200 \AA^3), and the number of free cavities with volume less than 0.05 \AA^3 is more than

half of the total number of cavities (see Figure 5.28), which gives little room for dihedrals to conduct conformational transitions. The large number of small free cavities also hints that the polymer is amorphous, since the aligned chains will lead to an increase in the number of larger, more elliptical free volumes[21]. Figure 5.26 also shows that there is much less free volume in the glassy state than in the rubbery state. Some snapshots of a 1 nm slice at 6 different temperatures are shown in Figure 5.29, in which the white background denotes the free volume. The free volume distribution associated with atoms is also examined in our study; the simulation results indicate that the distribution of free volume is generally associated with the atoms located at the ends of polymer chains and where the crosslinks are formed, which is consistent the observations discussed above.

The intermolecular radial distribution function $g(r)$, evaluated for the composite system without crosslinks, is shown in Figure 5.30 for polyethylene chains at 600 K, 400 K, 200 K and 75 K. The other two systems have the same trends. The first peak corresponds to the shortest distance between two neighboring chains; it increases with decreasing temperature. This can be attributed to the fact that decreasing temperature leads to higher densities and lower free volume in the systems. In Figure 5.31, we show the mean square distance with temperature. The data indicates that the introduction of nanodiamonds and crosslinks reduce the movement of polymer chains in the system, and the movement of polymer chain is almost fully stopped after temperature decreases to T_g .

5.4 SUMMARY

MD simulations were carried out to investigate the relationship between the glass transition temperature and chain length, nanodiamond density and pressure. The effect of nano fillers and pressure are suppressed in the long polymer chain systems; however, they will increase the glass transition temperature with increasing pressure and nano filler density in the short polymer chain systems. The nonbonded LJ potential energy and torsional energy decrease linearly with decreasing temperature both above and below T_g , with an abrupt change in slope at T_g . The free volume and transition data suggest that the glass transition is a second order phase transition, which is primarily associated with the freezing of the torsional degrees of polymer chains.

5.5 REFERENCES

1. Binder, K., *Monte Carlo and Molecular Dynamics Simulations in Polymer Science*. 1995, New York: Oxford University.
2. McKechnie, J.I., D. Brown, and J.H.R. Clarke, *METHODS OF GENERATING DENSE RELAXED AMORPHOUS POLYMER SAMPLES FOR USE IN DYNAMIC SIMULATIONS*. *Macromolecules*, 1992. **25**(5): p. 1562-1567.
3. Yang, L., D.J. Srolovitz, and A.F. Yee, *Molecular dynamics study of isobaric and isochoric glass transitions in a model amorphous polymer*. *Journal of Chemical Physics*, 1999. **110**(14): p. 7058-7069.
4. Fox, T.G. and P.J. Flory, *2ND-ORDER TRANSITION TEMPERATURES AND RELATED PROPERTIES OF POLYSTYRENE .1. INFLUENCE OF MOLECULAR WEIGHT*. *Journal of Applied Physics*, 1950. **21**(6): p. 581-591.
5. Boyer, R.F. and R. Simha, *RELATION BETWEEN EXPANSION COEFFICIENTS AND GLASS TEMPERATURE - REPLY*. *Journal of Polymer Science Part C-Polymer Letters*, 1973. **11**(1): p. 33-44.
6. Williams, M.L., R.F. Landel, and J.D. Ferry, *MECHANICAL PROPERTIES OF SUBSTANCES OF HIGH MOLECULAR WEIGHT .19. THE TEMPERATURE DEPENDENCE OF RELAXATION MECHANISMS IN AMORPHOUS POLYMERS AND OTHER GLASS-FORMING LIQUIDS*. *Journal of the American Chemical Society*, 1955. **77**(14): p. 3701-3707.
7. Doolittle, A.K., *Journal of Applied Physics*, 1951. **22**.
8. Gibbs, J.H. and E.A. DiMarzio, *NATURE OF THE GLASS TRANSITION AND THE GLASSY STATE*. *Journal of Chemical Physics*, 1958. **28**(3): p. 373-383.
9. Rigby, D. and R.J. Roe, *MOLECULAR-DYNAMICS SIMULATION OF POLYMER LIQUID AND GLASS .1. GLASS-TRANSITION*. *Journal of Chemical Physics*, 1987. **87**(12): p. 7285-7292.
10. Brown, D. and J.H.R. Clarke, *MOLECULAR-DYNAMICS SIMULATION OF AN AMORPHOUS POLYMER UNDER TENSION .1. PHENOMENOLOGY*. *Macromolecules*, 1991. **24**(8): p. 2075-2082.

11. Brown, D., et al., *THE PREPARATION OF POLYMER MELT SAMPLES FOR COMPUTER-SIMULATION STUDIES*. Journal of Chemical Physics, 1994. **100**(8): p. 6011-6018.
12. M. P. Allen, D.J.T., *Computer Simulations of Liquids*. 1987: Clarendon Press: Oxford.
13. Berendsen, H.J.C., et al., *MOLECULAR-DYNAMICS WITH COUPLING TO AN EXTERNAL BATH*. Journal of Chemical Physics, 1984. **81**(8): p. 3684-3690.
14. Smith, W., T.R. Forester, and I.T. Todorov, *The DL_POLY_2.0 User Manual*.
15. Colucci, D.M., et al., *Isochoric and isobaric glass formation: Similarities and differences*. Journal of Polymer Science Part B-Polymer Physics, 1997. **35**(10): p. 1561-1573.
16. A. Peterlin, *The Physics of Glassy Polymers*, R. N. Haward, Ed., Halsted Press, New York, 1973. 620 pp. \$45.00. Journal of Polymer Science: Polymer Letters Edition, 1973. **11**(10): p. 655.
17. Soldera, A., *Comparison between the glass transition temperatures of the two PMMA tacticities: A molecular dynamics simulation point of view*. Macromolecular Symposia, 1998. **133**: p. 21-32.
18. Fried, J.R. and P. Ren, *Molecular simulation of the glass transition of polyphosphazenes*. Computational and Theoretical Polymer Science, 1999. **9**(2): p. 111-116.
19. Liang, T.N., et al., *Conformational transition behavior around glass transition temperature*. Journal of Chemical Physics, 2000. **112**(4): p. 2016-2020.
20. Takeuchi, H., *MOLECULAR-DYNAMICS SIMULATIONS OF DIFFUSION OF SMALL MOLECULES IN POLYMERS - EFFECT OF CHAIN-LENGTH*. Journal of Chemical Physics, 1990. **93**(6): p. 4490-4491.
21. Dong, H. and K. Jacob, *Effect of molecular orientation on polymer free volume distribution: An atomistic approach*. Abstracts of Papers of the American Chemical Society, 2003. **225**: p. U660-U661.

FIGURES

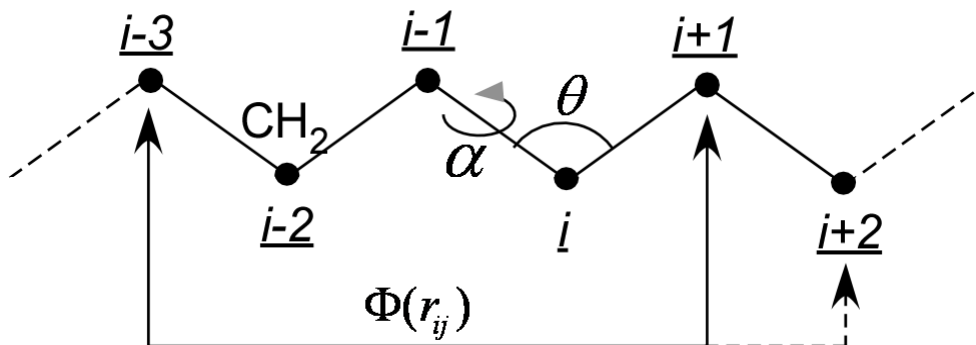


Figure 5.1 Individual chain model. The spherical “segment” simulates a CH_2 or CH_3 unit. A harmonic force constrains the bond length l around the equilibrium length l_0 . The bond angle θ is likewise constrained around the tetrahedral angle. The torsional angle ϕ , given by the angle between the plane containing segments $i-2$, $i-1$ and i and that contains segments $i-1$, i , and $i+1$, is subject to a threefold potential having *trans* and *gauche* minima. Segments separated by more than three bonds along the chain (for example $i-3$ and $i+1$), as well as segments which belong to different chains, interact according to a truncated Lennard-Jones potential.

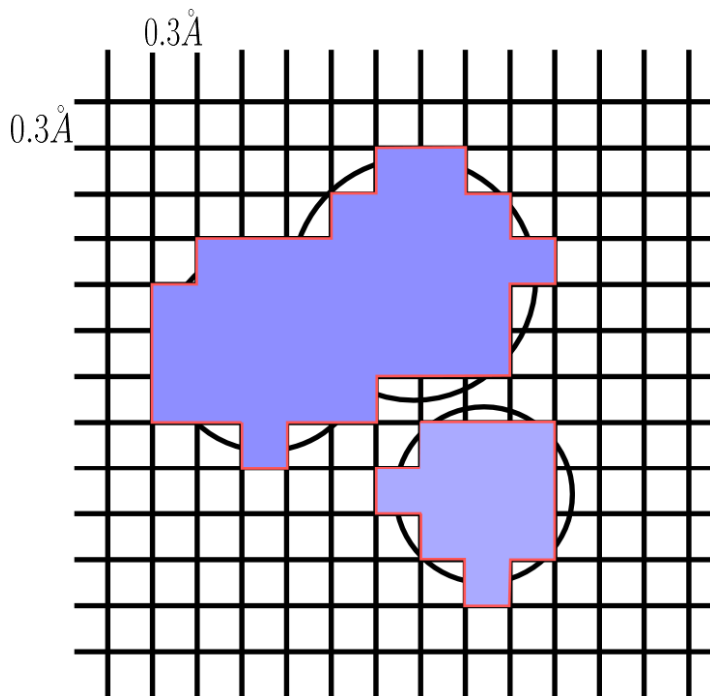
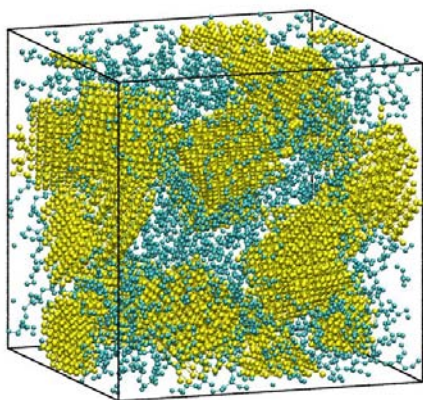
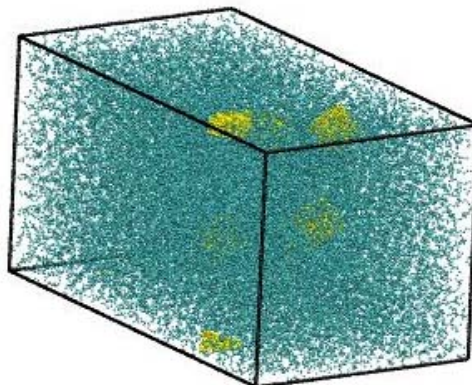


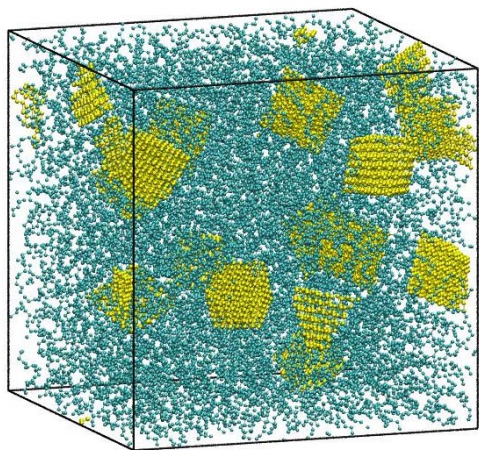
Figure 5.2 Two dimensional illustration of a free volume calculation.



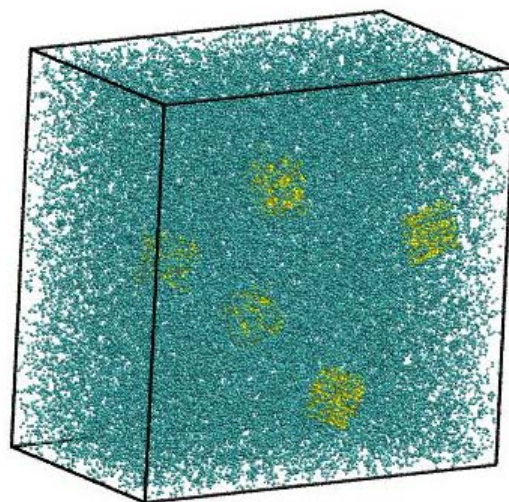
(a)



(b)

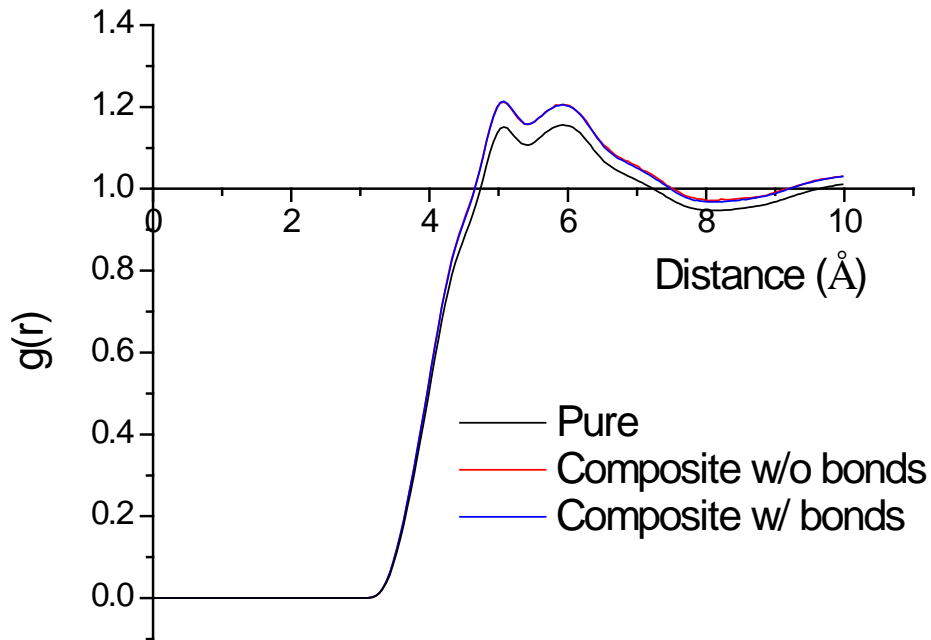


(c)

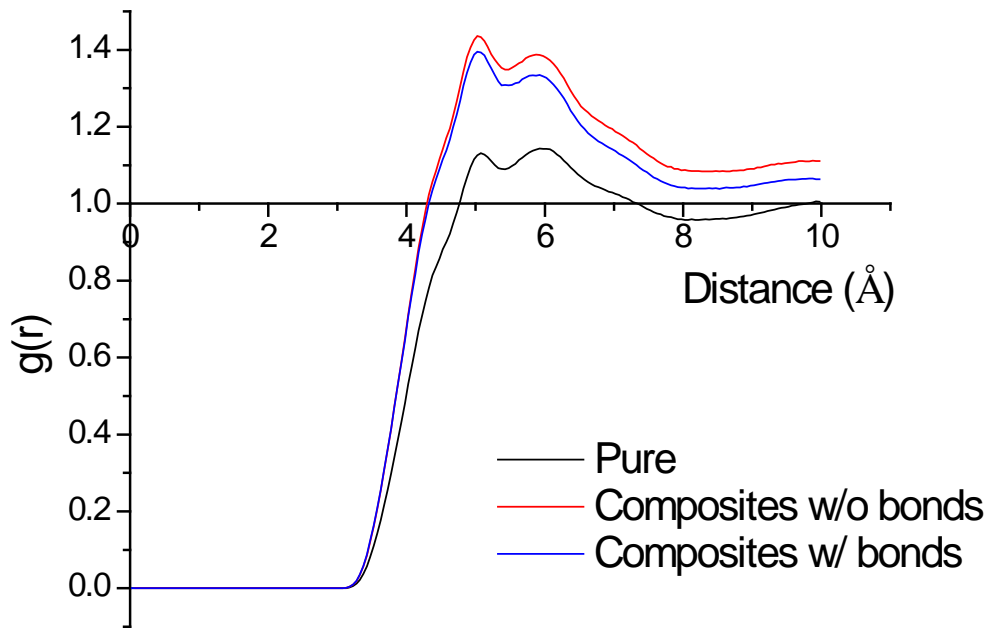


(d)

Figure 5.3 Composite samples at 1 bar and 600 K used in our studies (a) 12 NDs and 97x40 polyethylenes, (b) 6 NDs and 720x80 polyethylenes, (c) 12 NDs and 97x200 polyethylenes, and (d) 5 NDs 1440x40 polyethylenes.



(a) System with 12 NDs and 97x200 polyethylenes



(b) System with 12 NDs and 97x40 polyethylenes

Figure 5.4 Radial distribution function $g(r)$ for (a) system with 12 NDs and 97x200 polyethylene and (b) system with 12 NDs and 97x40 polyethylene.

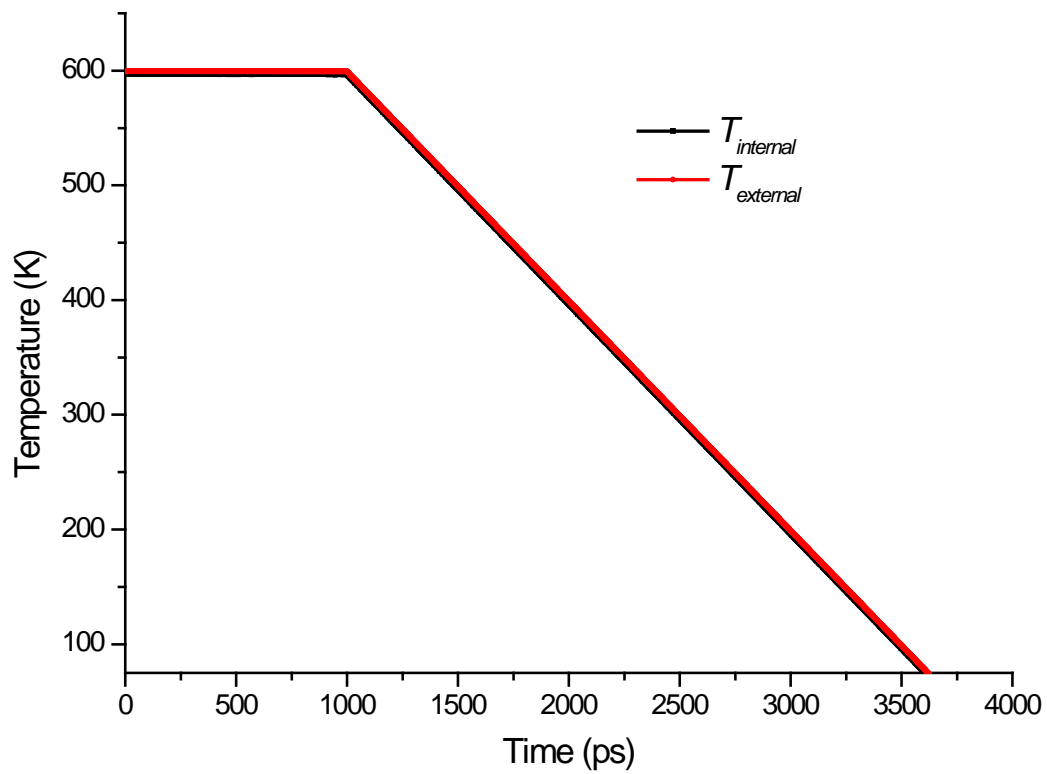


Figure 5.5 Temperature tracking for cooling procedure – polyethylene-NDs systems without linkages between polyethylene and NDs.

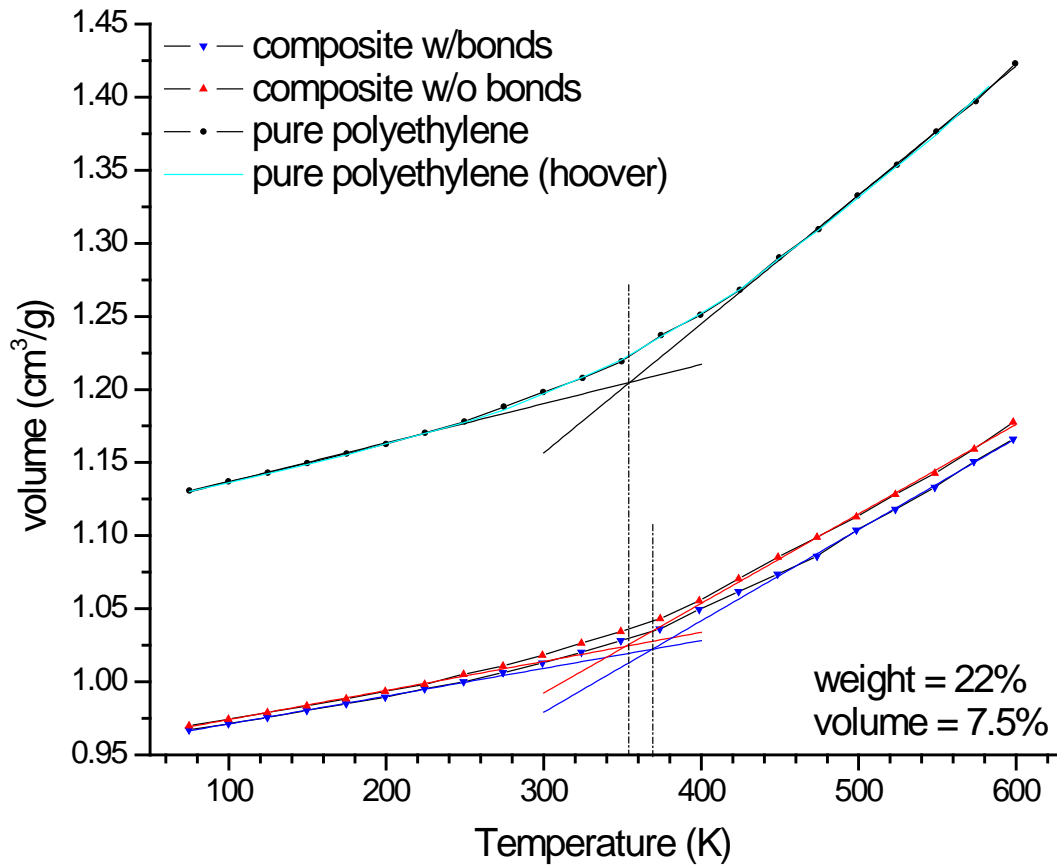


Figure 5.6 Average unit cell volume versus dynamics temperature for isobaric cooling at atmospheric pressure (1 bar) for the sample with 12 NDs and 97x200 polyethylenes. The symbols represent the simulation data, the solid lines represent the best linear fits (see Table 5.2) and the long red lines are extrapolations of the high temperature solid lines to below the glass transition. The black lines indicate T_g for each system.

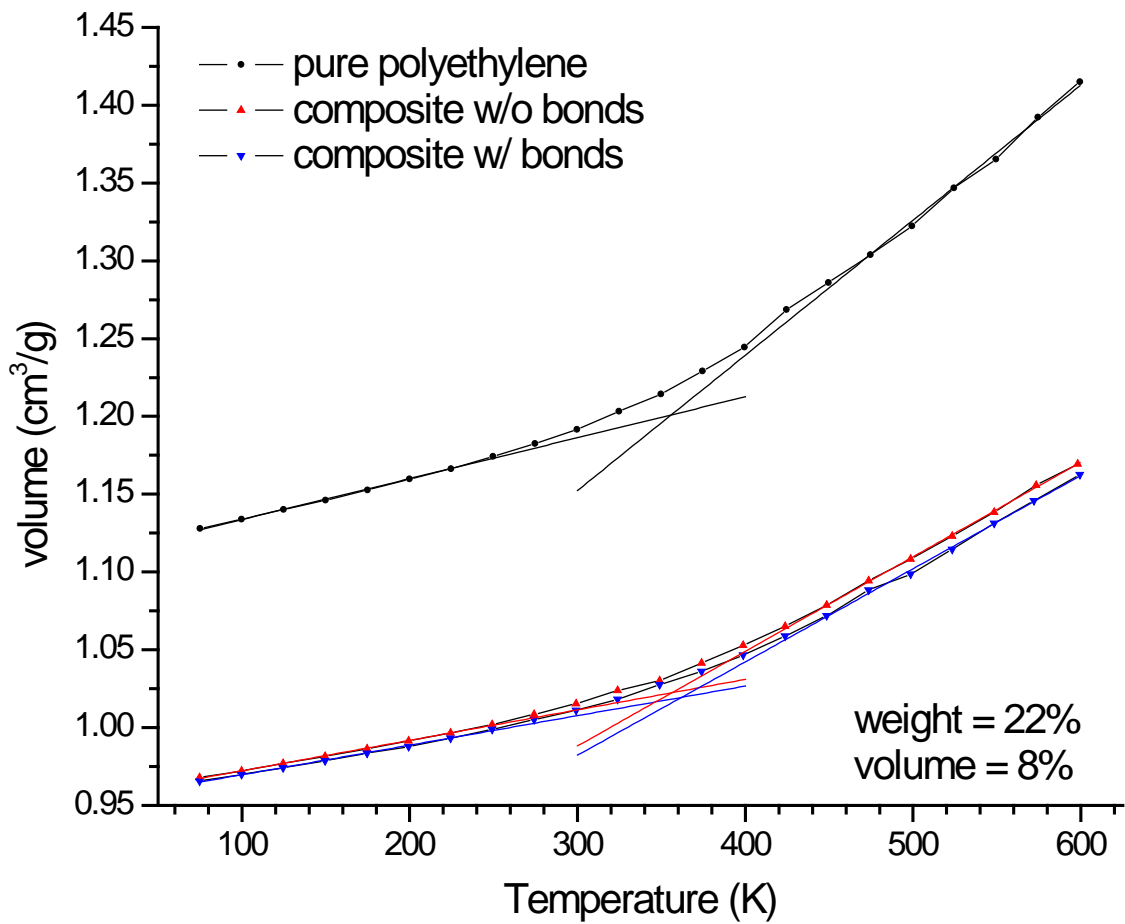


Figure 5.7 Average unit cell volume versus dynamics temperature for isobaric cooling at 100 bar for sample with 12 NDs and 97x200 polyethylenes. The symbols represent the simulation data, the solid lines represent the best linear fits (see Table 5.3) and the long red lines are extrapolations of the high temperature solid lines to below the glass transition. The black lines indicate T_g for each system.

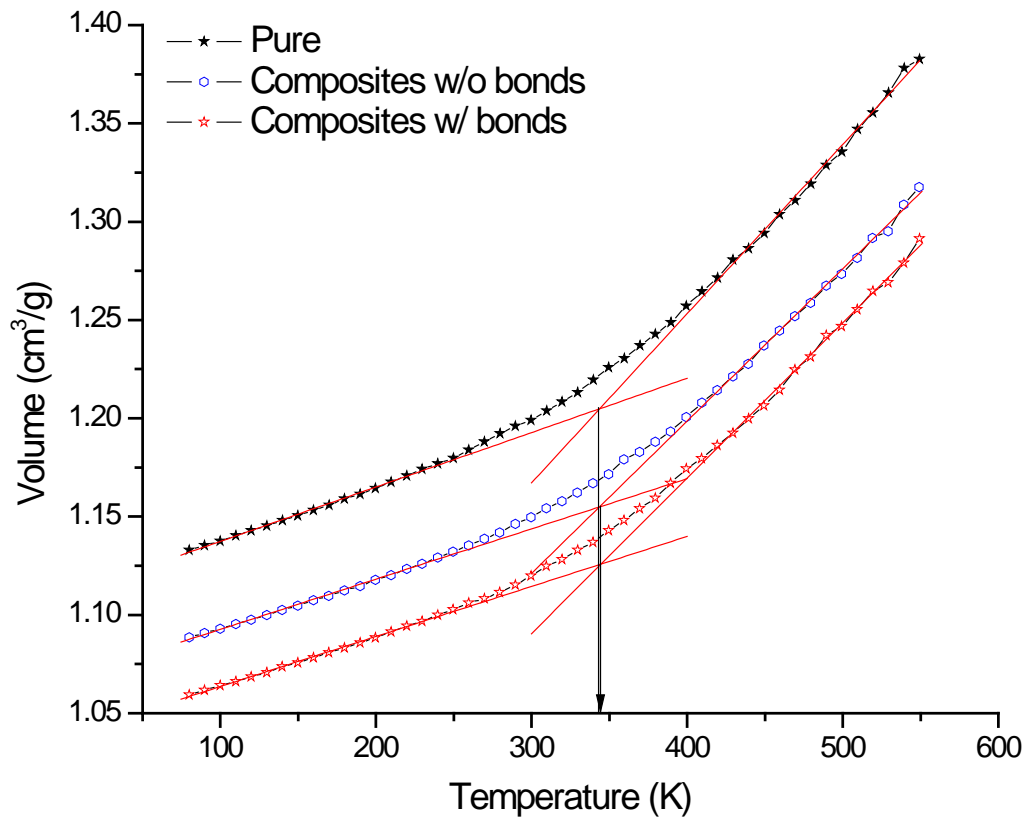


Figure 5.8 Average unit cell volume versus dynamics temperature for isobaric cooling at 1 bar for the sample with 5 NDs and 720x80 polyethylenes. The symbols represent the simulation data, the solid lines represent the best linear fits (see Table 5.4) and the long red lines are extrapolations of the high temperature solid lines to below the glass transition. The black lines indicate T_g for each system.

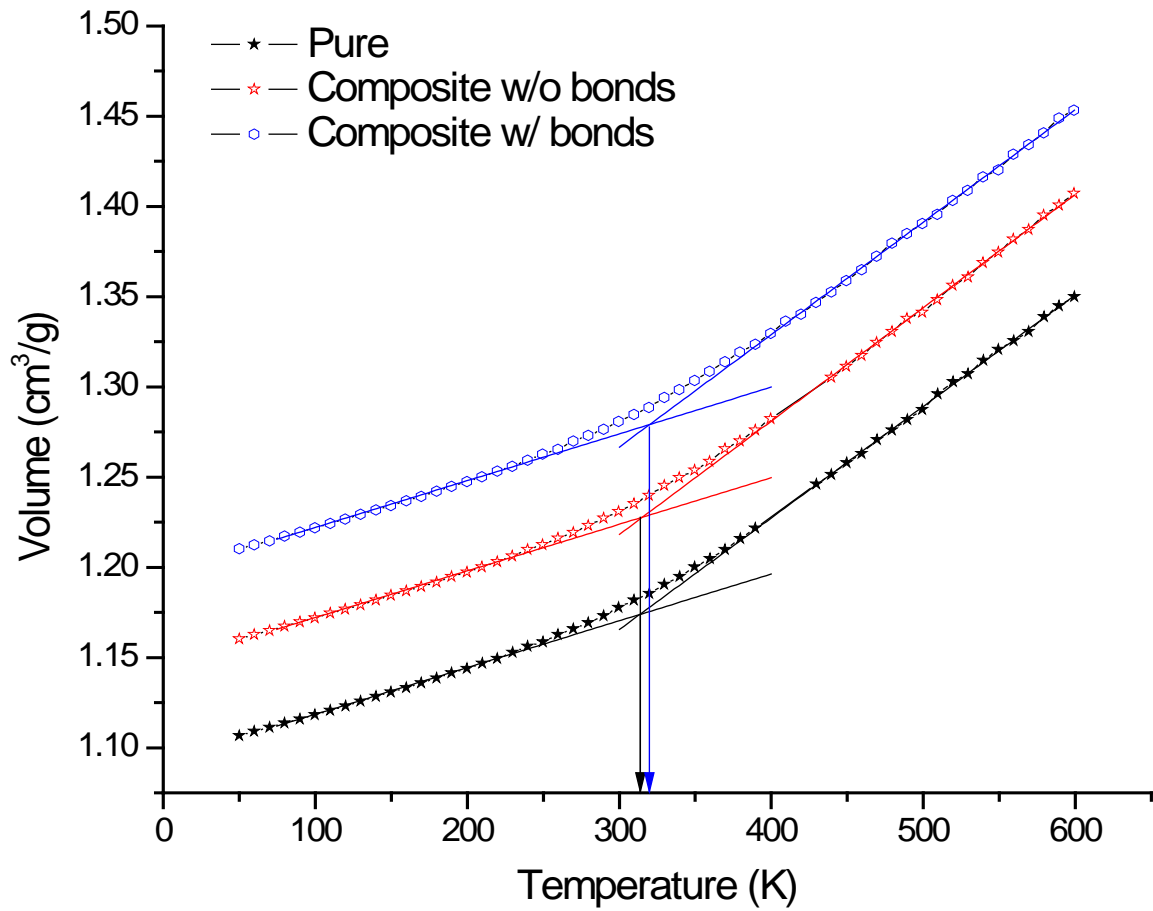


Figure 5.9 Average unit cell volume versus dynamics temperature for isobaric cooling at 1 bar for the sample with 5 NDs and 1440x40 polyethylenes. The symbols represent the simulation data, the solid lines represent the best linear fits (see Table 5.5) and the long red lines are extrapolations of the high temperature solid lines to below the glass transition. The black lines indicate T_g for each system.

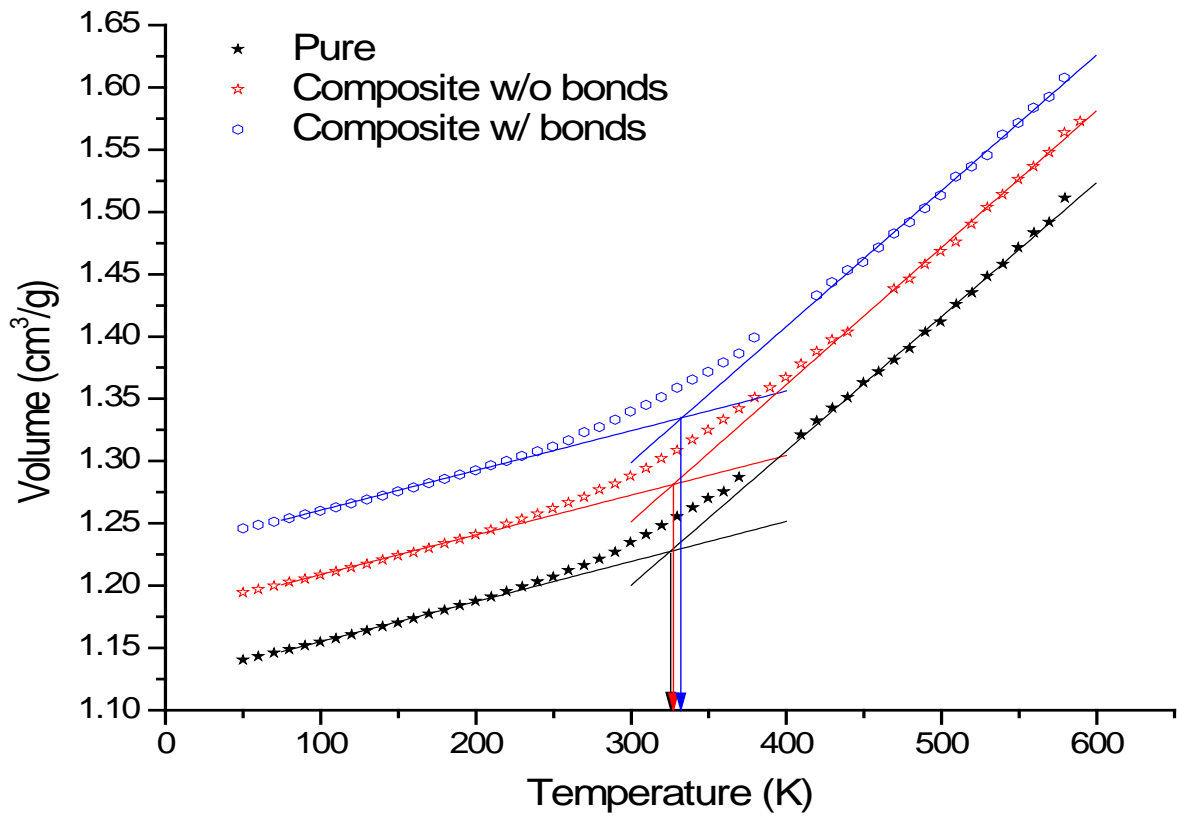


Figure 5.10 Average unit cell volume versus dynamics temperature for isobaric cooling at 100 bar for the sample with 6 NDs and 1440x40 polyethylenes. The symbols represent the simulation data, the solid lines represent the best linear fits (see Table 5.6) and the long red lines are extrapolations of the high temperature solid lines to below the glass transition. The black lines indicate T_g for each system.

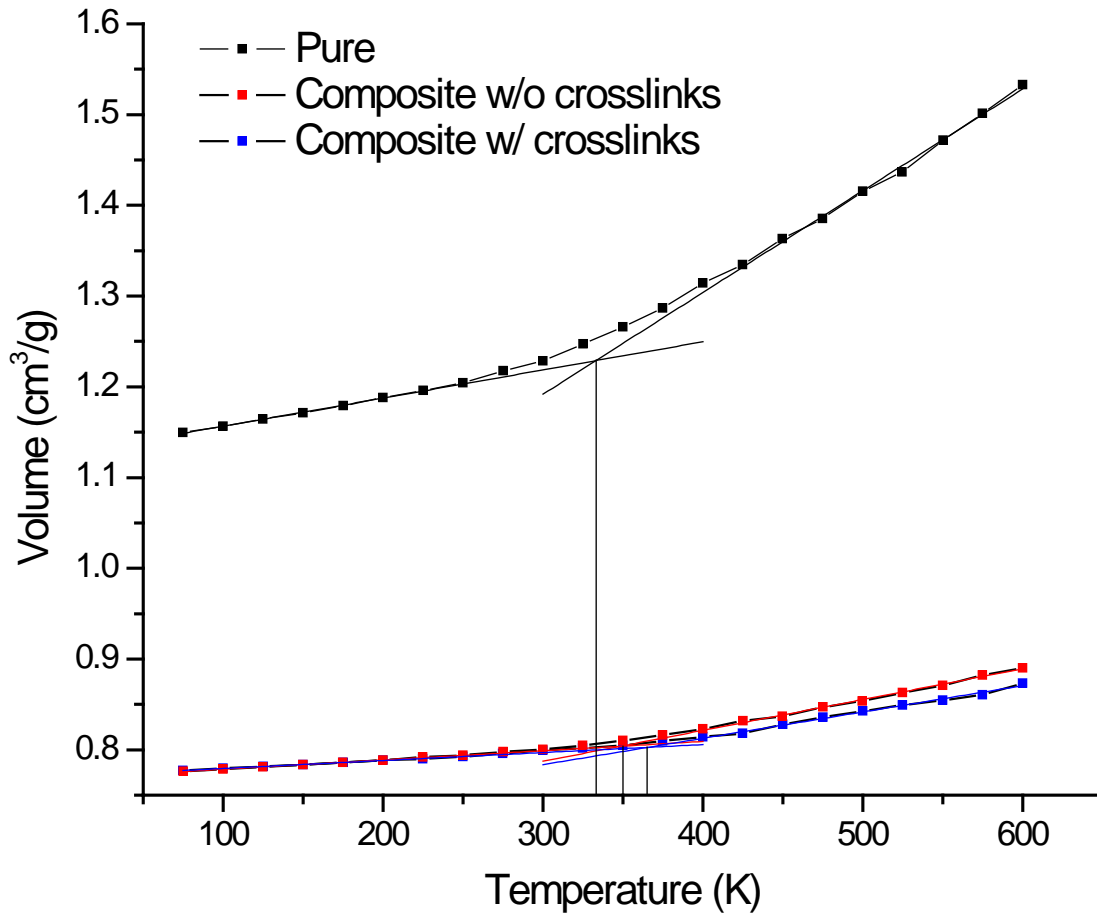
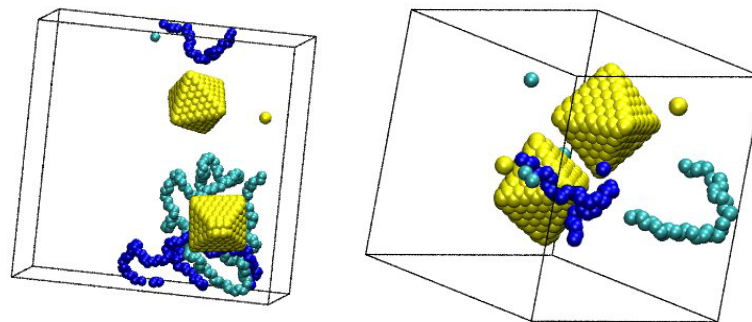


Figure 5.11 Average unit cell volume versus dynamics temperature for isobaric cooling at 1 bar for sample with 12 NDs and 97x40 polyethylenes. The symbols represent the simulation data, the solid lines represent the best linear fits (see Table 5.7) and the long red lines are extrapolations of the high temperature solid lines to below the glass transition. The black lines indicate T_g for each system.

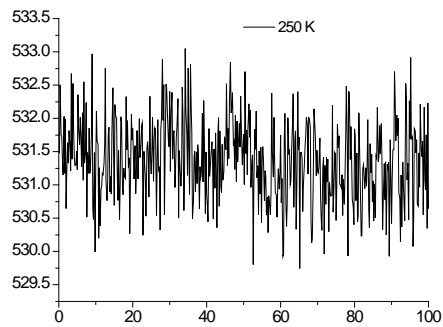
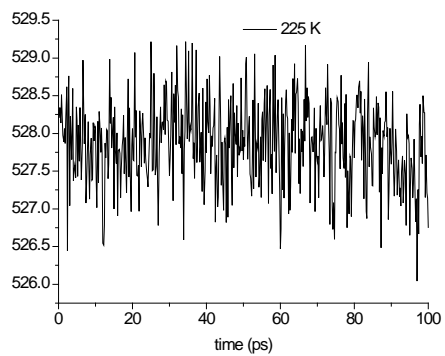
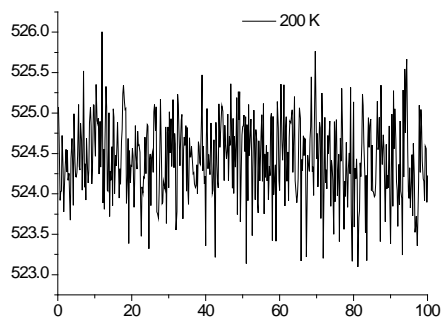
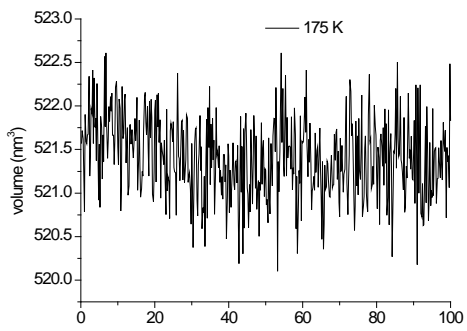
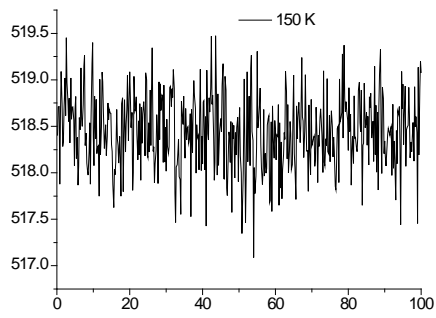
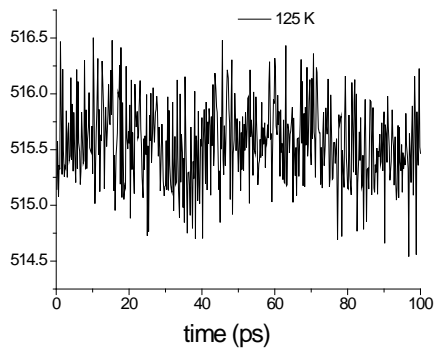
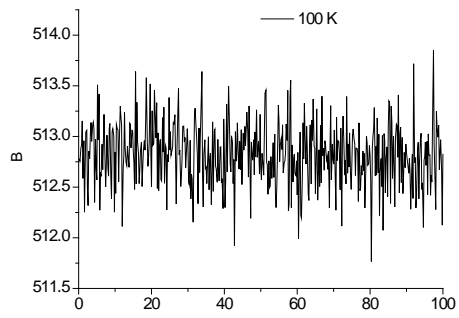
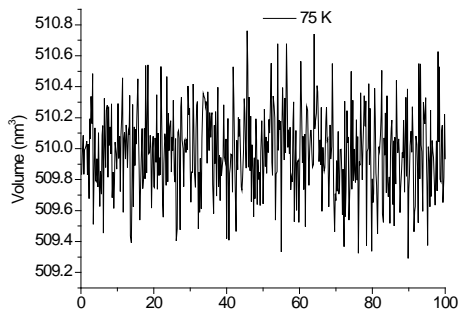


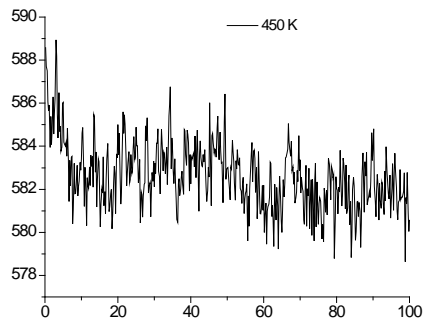
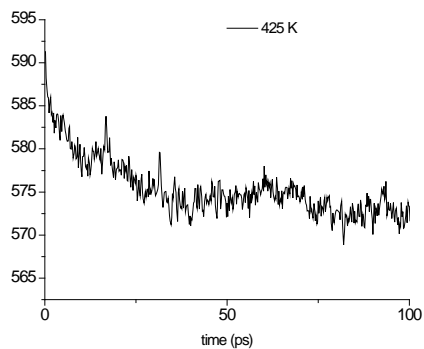
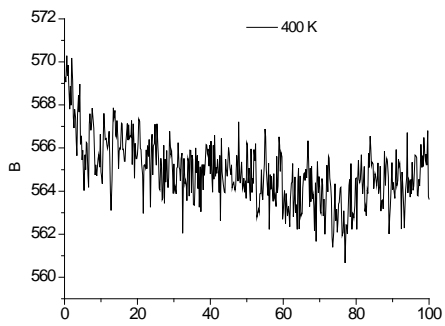
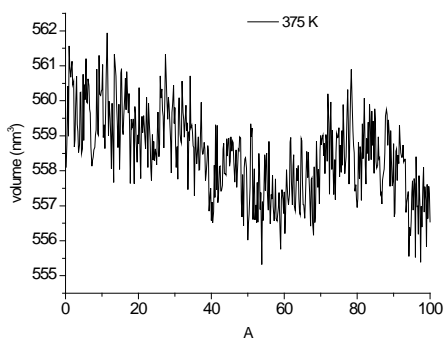
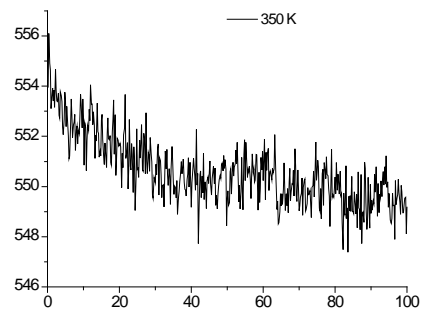
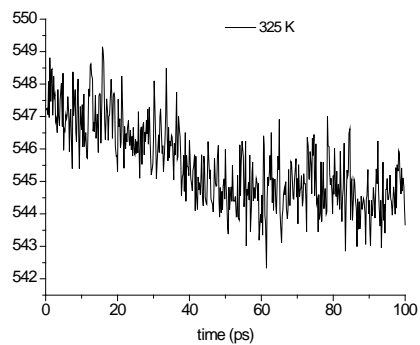
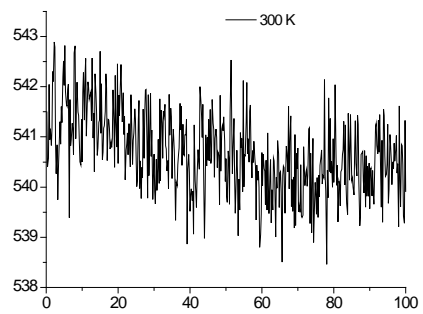
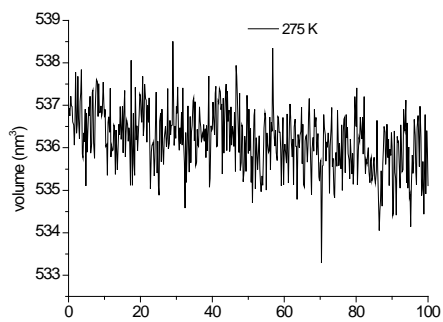
(a) long chain

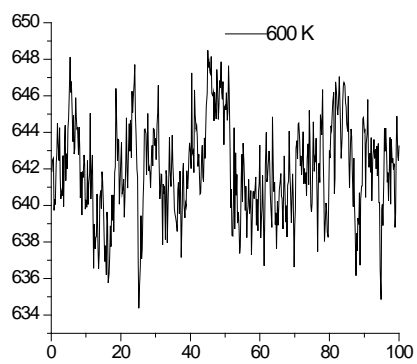
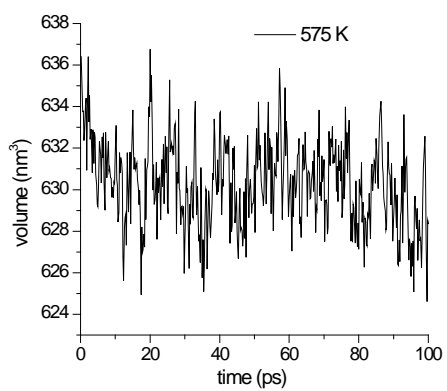
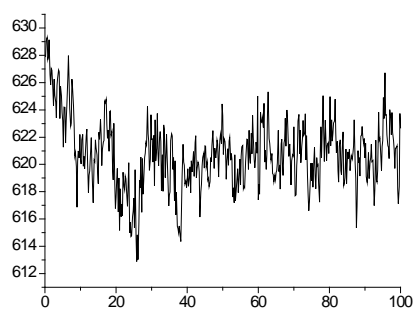
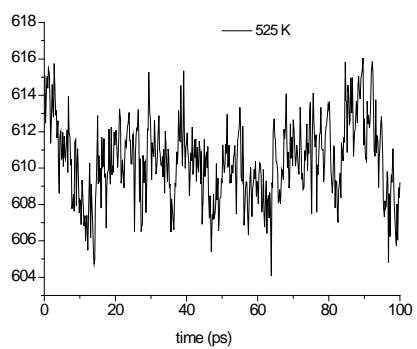
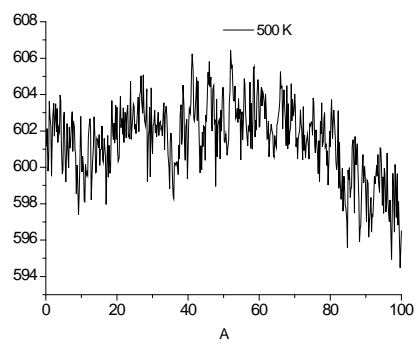
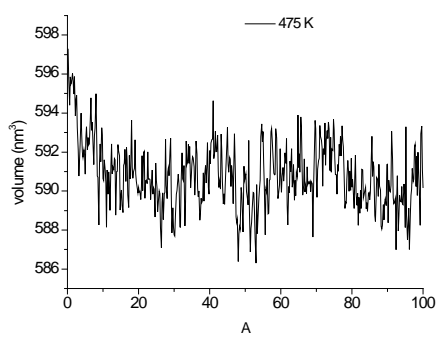
(b) short chain

Figure 5.12 The relative size of nanodiamond and polymer chain

Figure 5.13 Pristine unit cell volume versus dynamics time







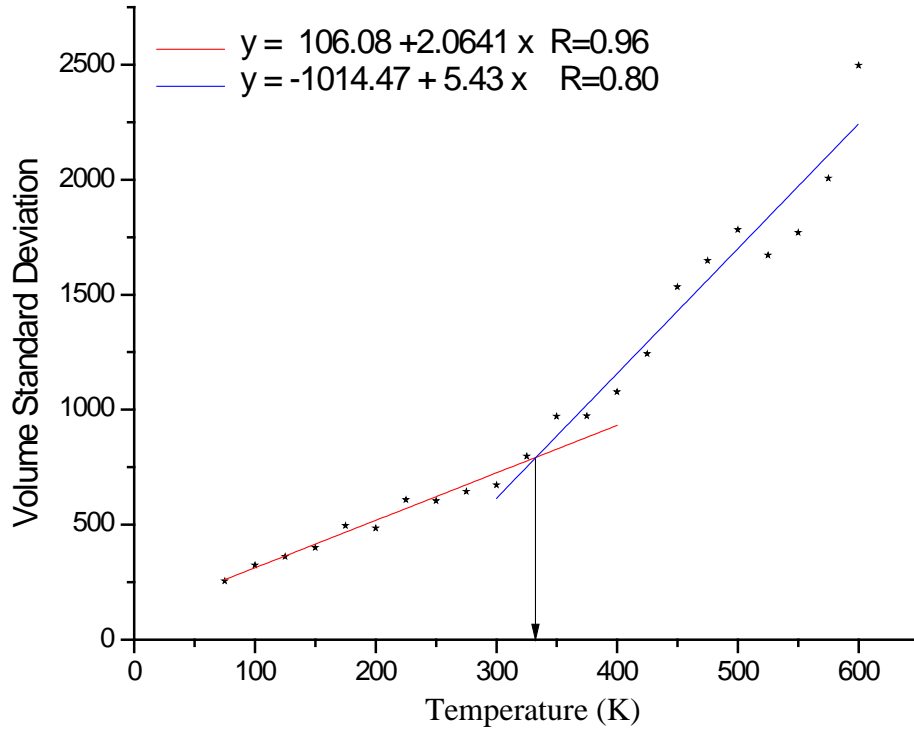


Figure 5.1 Standard deviation of the unit cell volume versus dynamics temperature for pure polyethylene

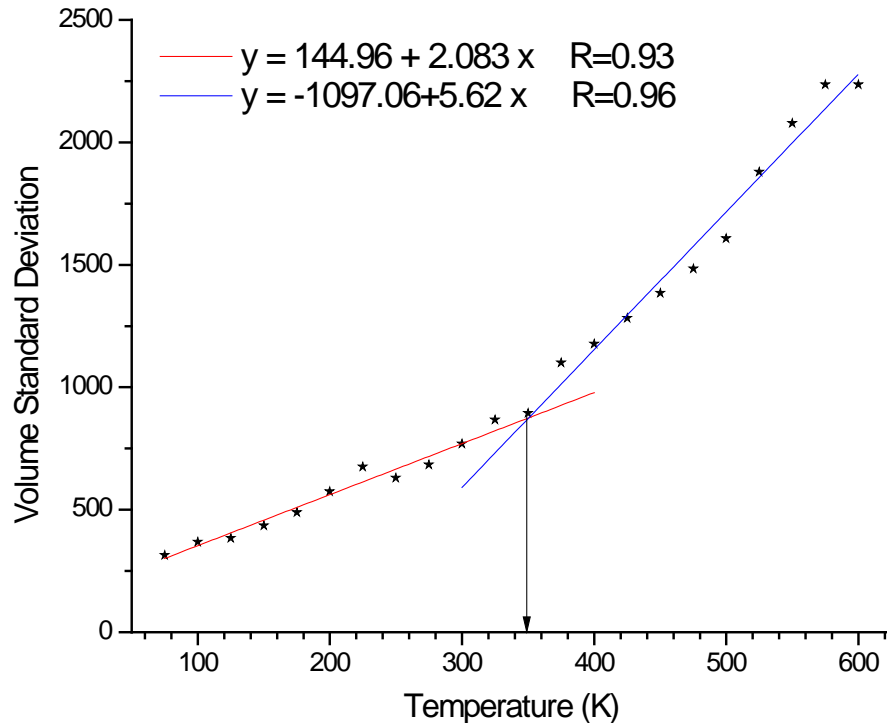


Figure 5.2 Standard deviation of the unit cell volume versus dynamics temperature for composites without crosslinks

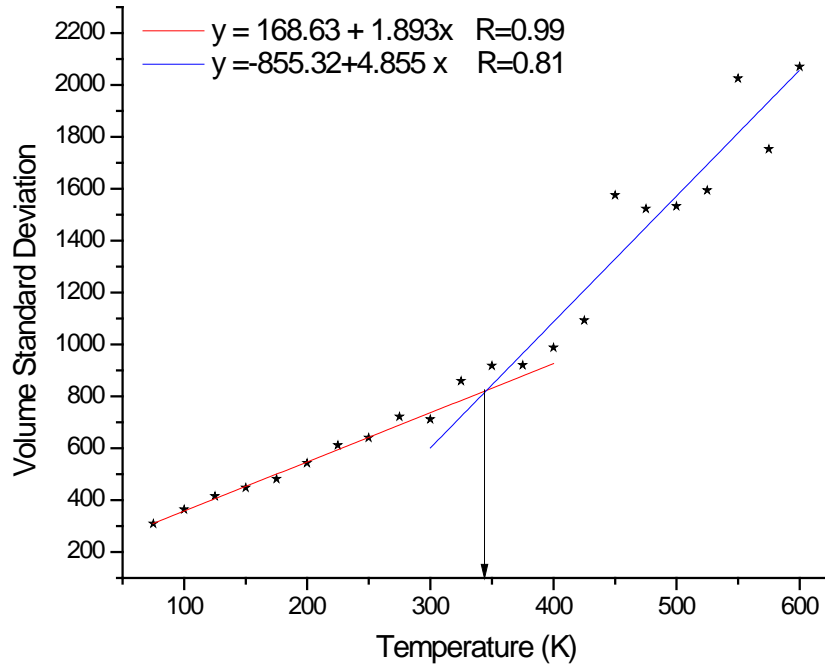


Figure 5.3 Standard deviation of the unit cell volume versus dynamics temperature for composites with crosslinks

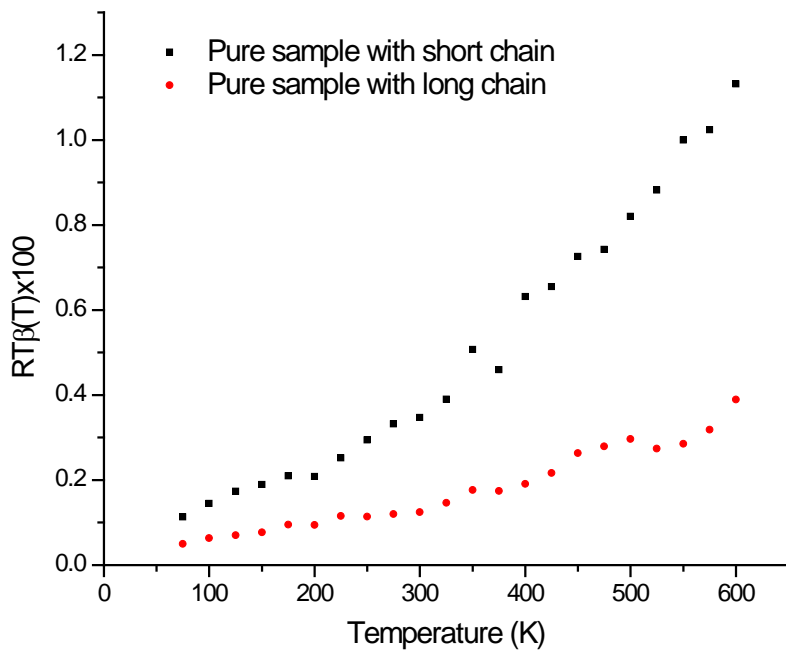


Figure 5.4 Compressibility versus temperature for pure sample with short/long chain

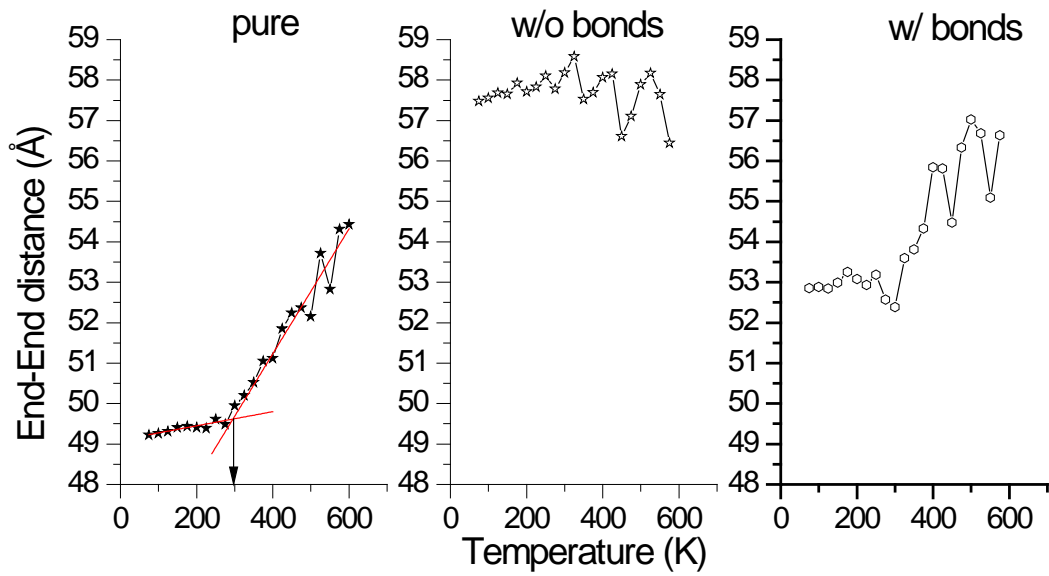


Figure 5.5 End-end distance versus dynamics temperature for the sample group with 12 NDs and 97x200 polyethylenes

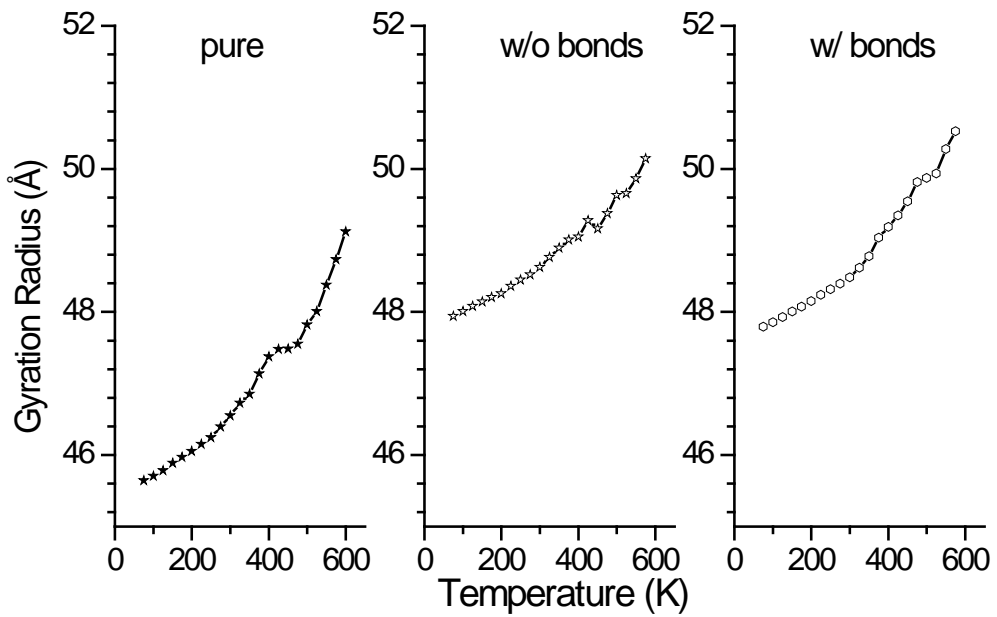


Figure 5.6 Gyration radius for the sample group with 12 NDs and 97x200 polyethylenes

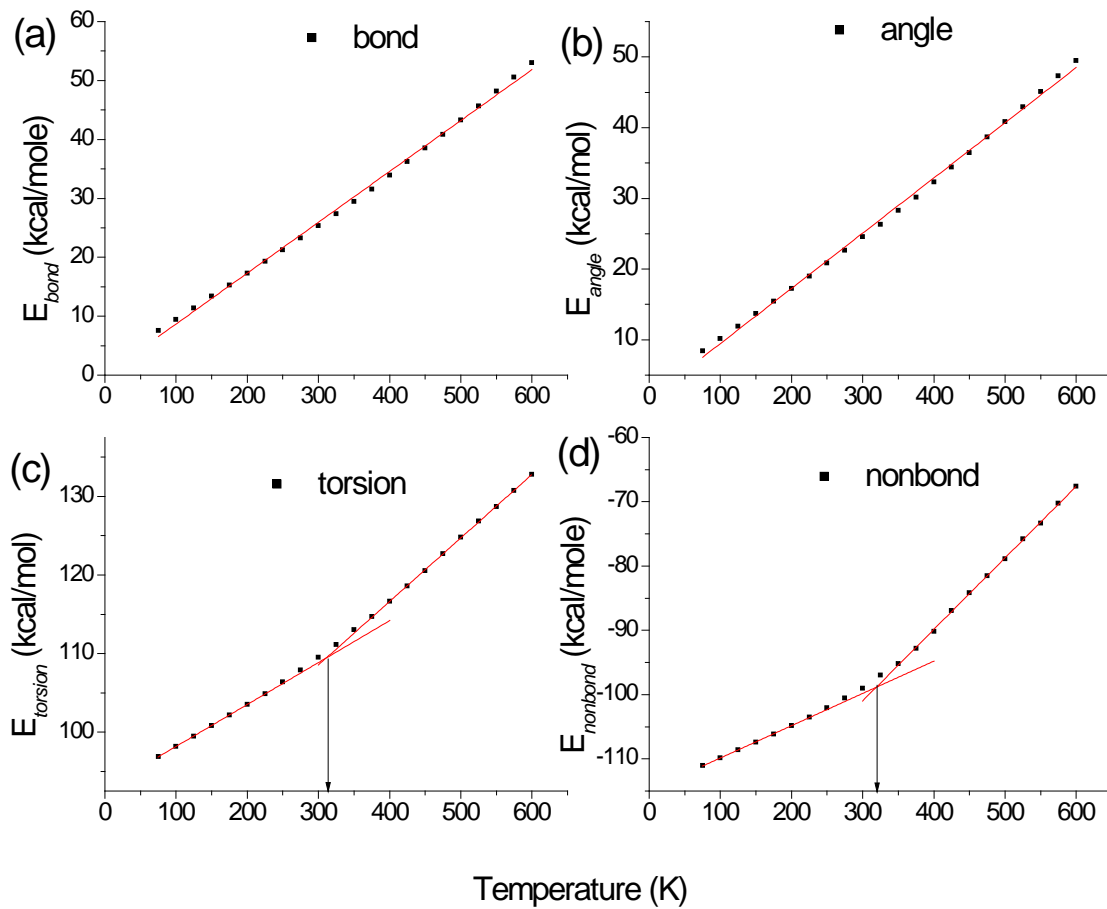


Figure 5.7 Plots of some energy components versus temperature for pure polyethylene: (a) bond energy; (b) angle energy; (c) torsion energy; (d) non-bond energy

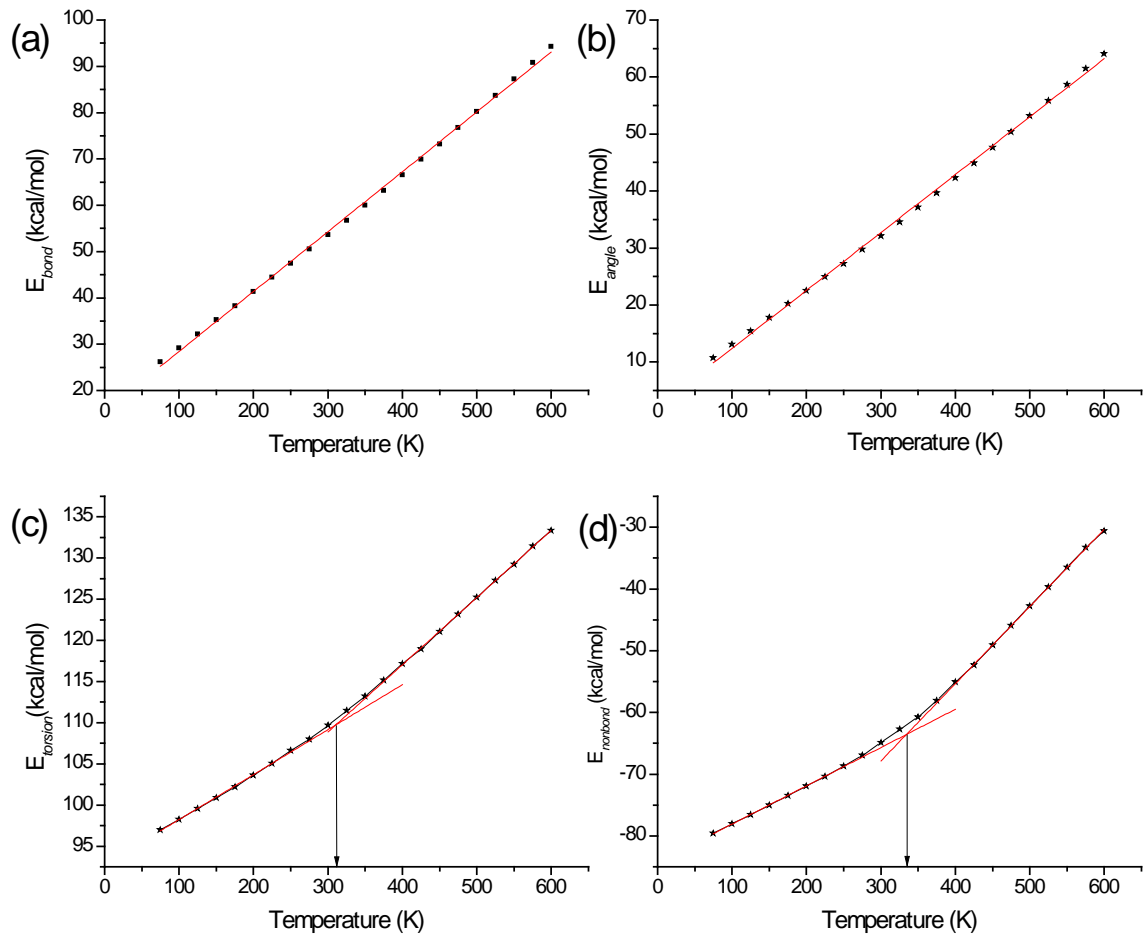


Figure 5.8 Plots of some energy components versus temperature for composites without bonds: (a) bond energy; (b) angle energy; (c) torsion energy; (d) non-bond energy

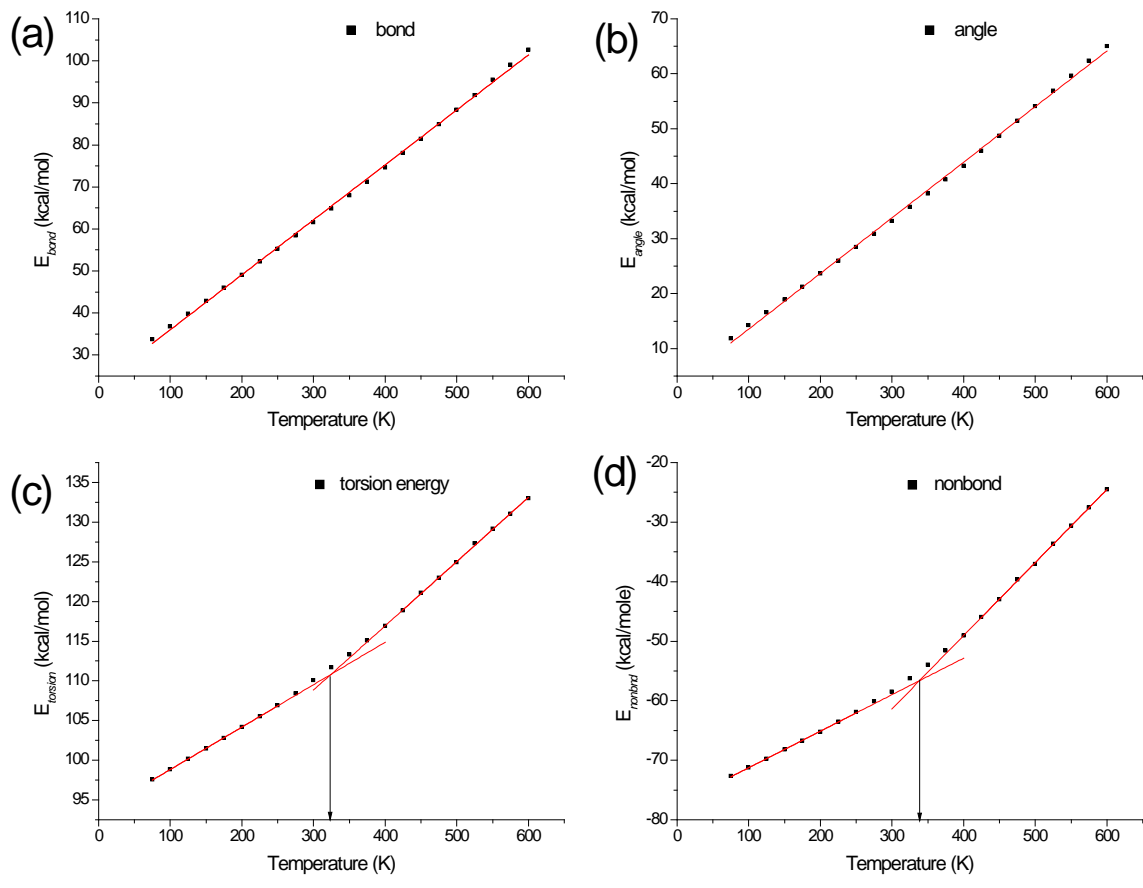


Figure 5.9 Plots of some energy components versus temperature for composites with bonds: (a) bond energy; (b) angle energy; (c) torsion energy; (d) non-bond energy

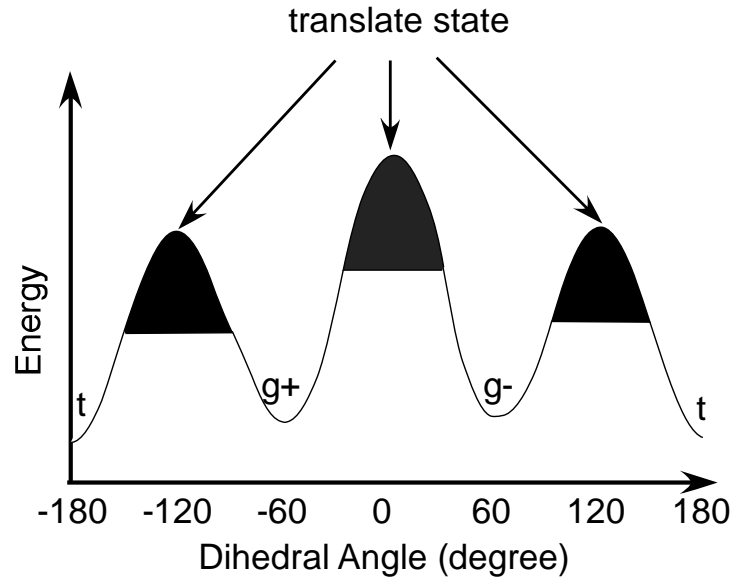


Figure 5.10 The illustration of the transition state and the conformational state. Minimum of the energy curve is the T , G^+ , and G^- conformational state. The shaded domains are the transition state areas.

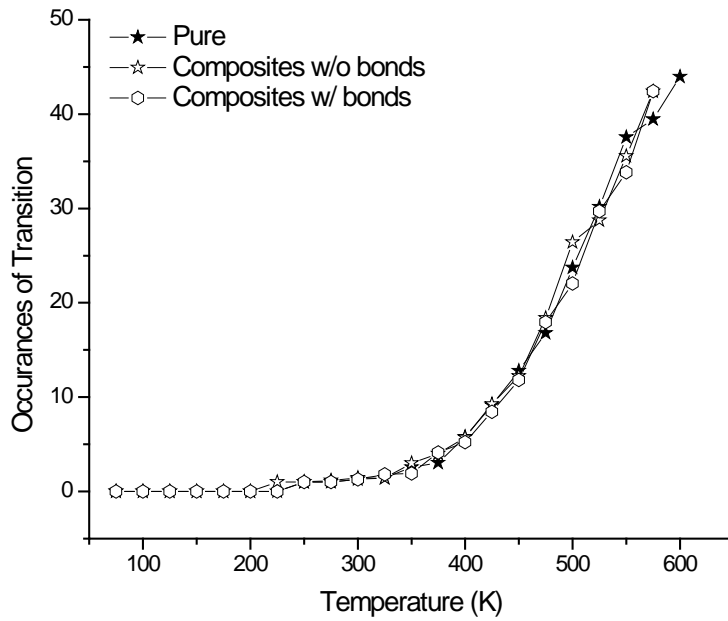


Figure 5.11 The occurrences of transition versus temperature

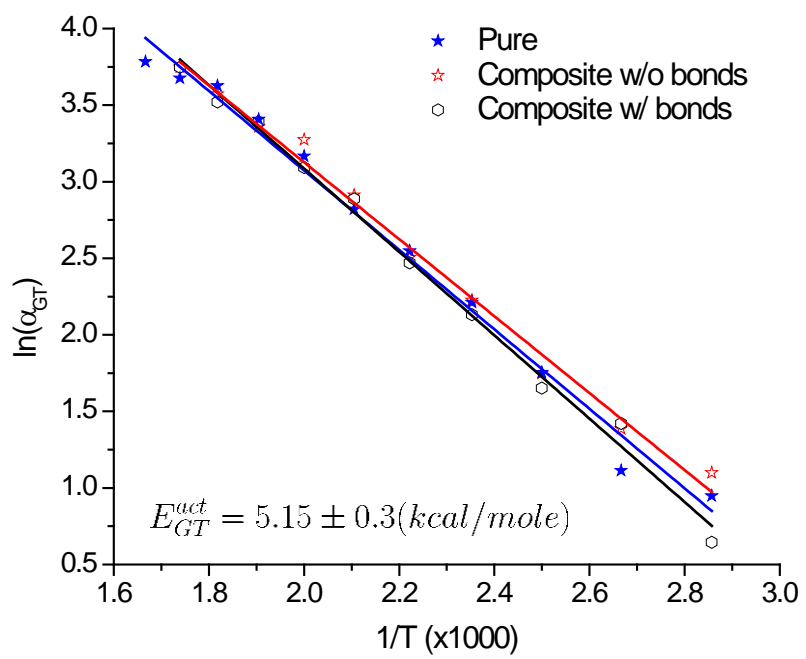


Figure 5.12 Activation energy of torsional rotation

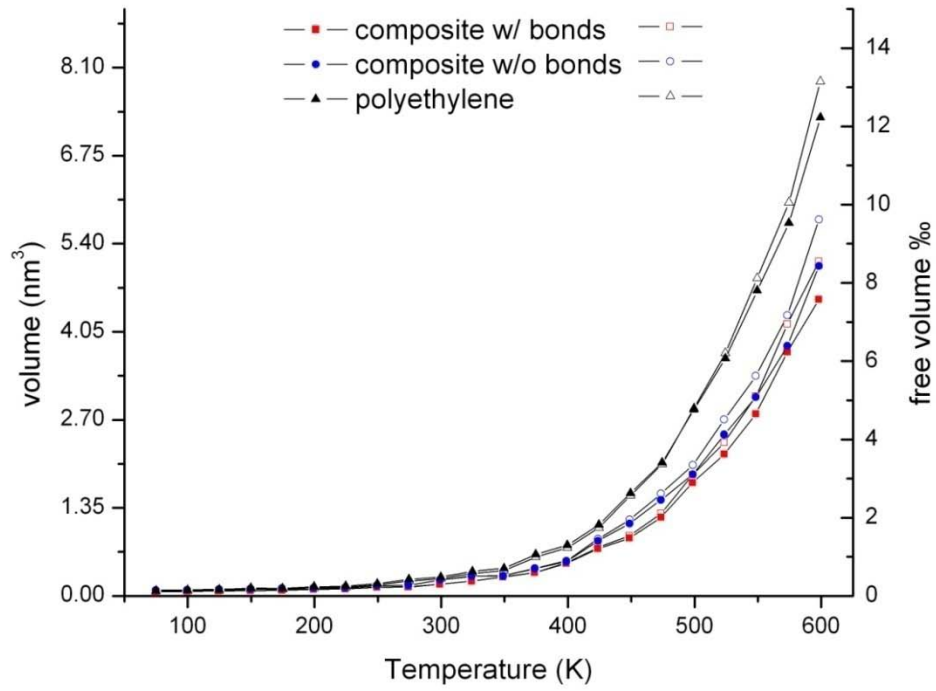


Figure 5.13 Available free volume in three samples at 1 bar.

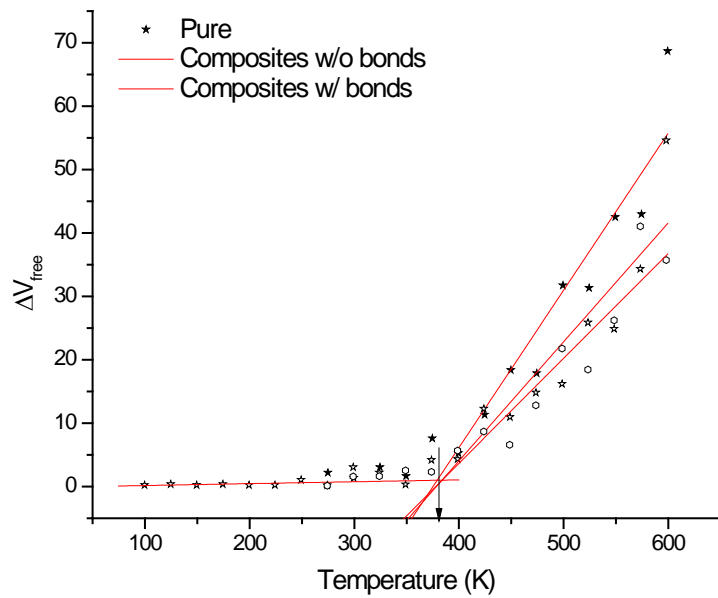


Figure 5.14 Difference hole volume ΔV_{free} as a function of the temperature.

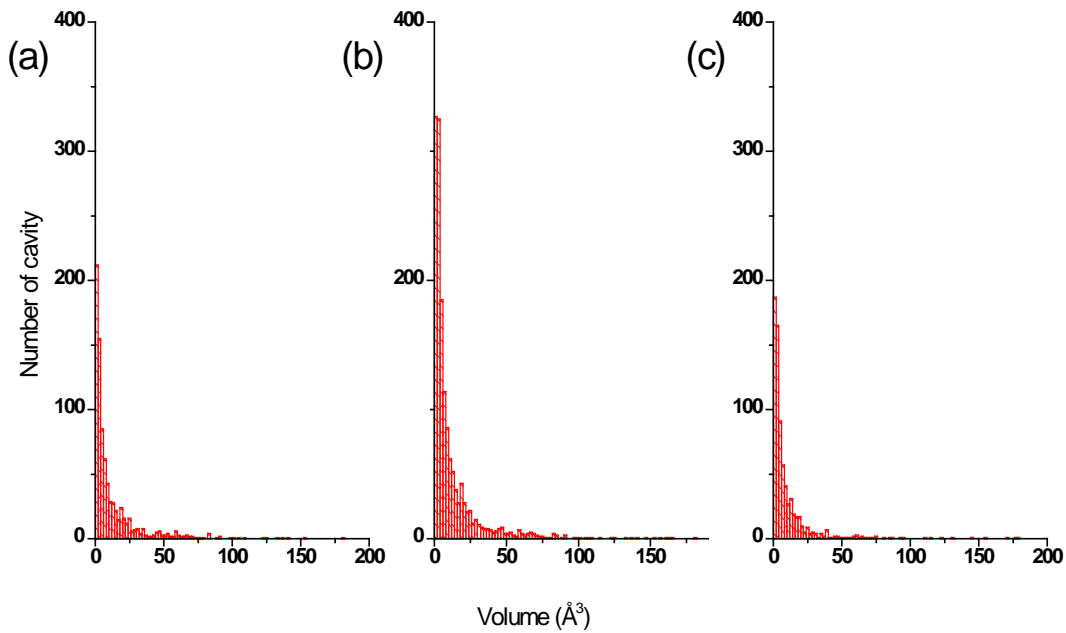


Figure 5.15 Number of cavities versus volume for composites w/o bonds at 100 bar and 600 K; (a) pure; (b) composites w/o bonds; (c) composite with bonds.

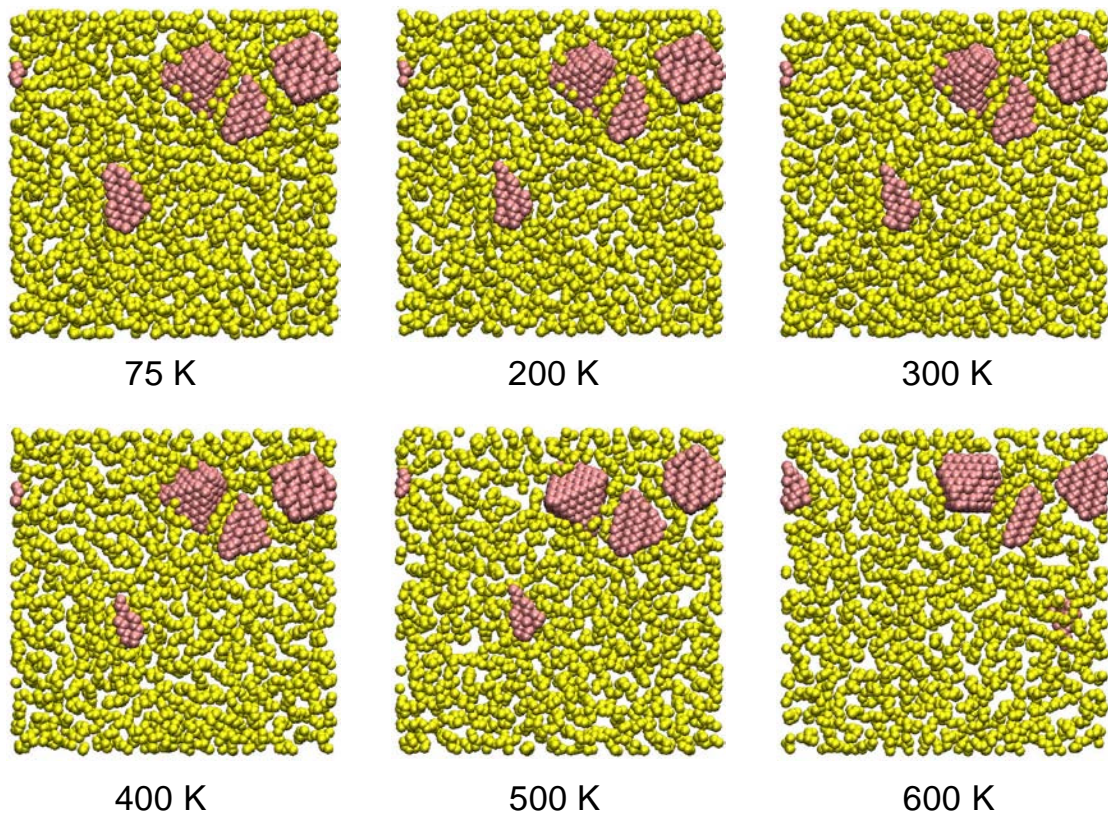


Figure 5.16 Snapshot of 1 nm slice of composites without bonds at 6 different temperatures.

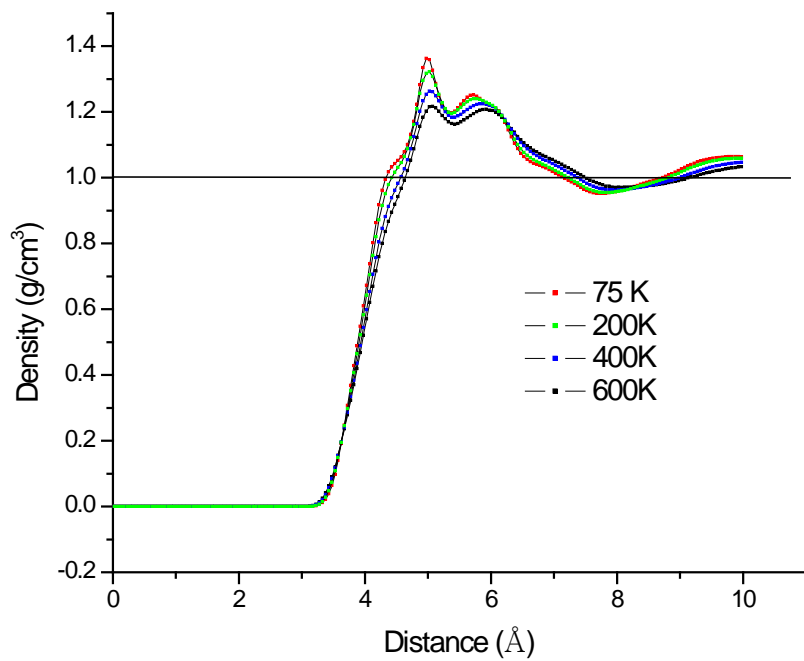


Figure 5.17 Radial distribution function of CH₂ units in a composite without crosslinks.

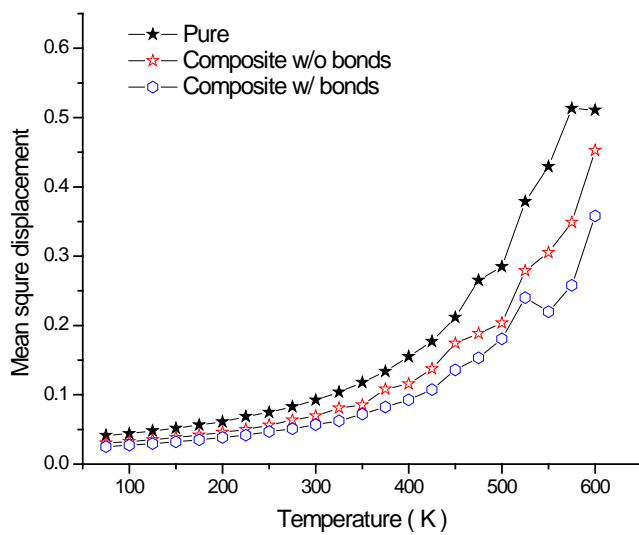


Figure 5.18 Mean square displacement versus temperature

TABLES

Table 6.1 Samples used in our studies

Pressure	Number of chains	Chain length	Number of NDs	Number of crosslinks	v% of ND	w% of NDs
1 bar	97	200	14	95	5.6%	22%
100 bar	97	200	14	95	5.6%	22%
1 bar	720	80	5	195	0.5%	5%
1 bar	1440	40	5	51	0.5%	5%
100 bar	1440	40	5	51	0.5%	5%
1 bar	97	40	14	87	21.9%	58.5%

Table 6.2 Parameters obtained from fitting the specific volume v vs T (see Figure 5.6) for the NPT ensemble cooling data at 1 bar.

System	$T < T_g$			T_g			$T > T_g$		
	Fitting Range (K)	$a_g \times 10^4$	b_g	T(K)	V_g	strength a_r/a_g	Fitting Range (K)	$a_r \times 10^4$	b_r
Pure	75-250	2.679±0.05	1.110±0.01	354.7	1.2050	3.203	450-600	8.824±0.12	0.892±0.006
w/o bonds	75-250	1.988±0.00	0.954±0.00	352.0	1.0243	3.081	450-600	6.124±0.01	0.808±0.007
w/ bonds	75-250	1.900±0.03	0.952±0.00	362.9	1.0223	3.187	450-600	6.247±0.01	0.792±0.005

Table 6.3 Parameters obtained from fitting the specific volume v vs T (see Figure 5.7) for the NPT ensemble cooling data at 100 bar.

System	$T < T_g$			T_g			$T > T_g$		
	Fitting Range (K)	$a_g \times 10^4$	b_g	T(K)	V_g	strength a_r/a_g	Fitting Range (K)	$a_r \times 10^4$	b_r
Pure	75-250	2.628±0.05	1.107±0.00	355.9	1.2010	3.3048	450-600	8.685±0.19	0.892±0.007
w/o bonds	75-250	1.957±0.03	0.953±0.01	356.2	1.0224	3.1067	450-600	6.079±0.07	0.806±0.004
w/ bonds	75-250	1.899±0.04	0.951±0.00	362.2	1.0149	3.1556	450-600	5.806±0.07	0.802±0.003

Table 6.4 Parameters obtained from fitting the specific volume v vs T (see Figure 5.8) for the NPT ensemble cooling data at 100 bar.

System	$T < T_g$			T_g			$T > T_g$		
	Fitting Range (K)	$a_g \times 10^4$	b_g	T(K)	V_g	strength a_r/a_g	Fitting Range (K)	$a_r \times 10^4$	b_r
Pure	50-250	2.7657 ± 0.00	1.110 ± 0.00	343.8	1.205	3.112	450-600	8.608 ± 0.01	0.909 ± 0.00
w/o bonds	50-250	2.544 ± 0.00	1.068 ± 0.00	344.8	1.156	3.106	450-600	7.903 ± 0.01	0.893 ± 0.001
w/ bonds	50-250	2.554 ± 0.03	1.067 ± 0.01	343.6	1.155	3.302	450-600	7.745 ± 0.01	0.889 ± 0.001

Table 6.5 Parameters obtained from fitting the specific volume v vs T (see Figure 5.9) for the NPT ensemble cooling data at 1 bar.

System	$T < T_g$			T_g			$T > T_g$		
	Fitting Range (K)	$a_g \times 10^4$	b_g	T(K)	V_g	strength a_r/a_g	Fitting Range (K)	$a_r \times 10^4$	b_r
Pure	50-250	2.593 ± 0.00	1.109 ± 0.00	313.4	1.174	2.385	450-600	6.18 ± 0.01	0.980 ± 0.002
w/o bonds	50-250	2.584 ± 0.00	1.090 ± 0.00	315.2	1.178	2.432	450-600	6.28 ± 0.01	0.980 ± 0.002
w/ bonds	50-250	2.592 ± 0.03	1.096 ± 0.01	319.8	1.179	2.404	450-600	6.23 ± 0.01	0.979 ± 0.001

Table 6.6 Parameters obtained from fitting the specific volume v vs T (see Figure 5.10) for the NPT ensemble cooling data at 1 bar.

System	$T < T_g$			T_g			$T > T_g$		
	Fitting Range (K)	$a_g \times 10^4$	b_g	T(K)	V_g	strength a_r/a_g	Fitting Range (K)	$a_r \times 10^4$	b_r
Pure	50-250	2.590 ± 0.00	1.007 ± 0.00	332.1	1.093	3.344	450-600	5.66 ± 0.01	0.905 ± 0.006
w/o bonds	50-250	2.570 ± 0.00	0.987 ± 0.00	327.3	1.071	3.315	450-600	5.809 ± 0.01	0.881 ± 0.008
w/ bonds	50-250	2.562 ± 0.03	0.989 ± 0.01	333.2	1.074	3.404	450-600	5.713 ± 0.01	0.884 ± 0.006

Table 6.7 Parameters obtained from fitting the specific volume v vs T (see Figure 5.11) for the NPT ensemble cooling data at 1bar.

System	$T < T_g$			T_g			$T > T_g$		
	Fitting Range (K)	$a_g \times 10^4$	b_g	T(K)	V_g	strength a_r/a_g	Fitting Range (K)	$a_r \times 10^4$	b_r
Pure	50-250	3.102 ±0.00	1.125 ±0.00	333.7	1.229	3.610	450-600	11.2 ±0.02	0.855±0.01
w/o bonds	50-250	1.019 ±0.00	0.768 ±0.00	348.7	0.804	3.335	450-600	3.400±0.01	0.685±0.001
w/ bonds	50-250	0.876±0.01	0.771 ±0.01	365.6	0.803	3.313	450-600	2.903 ±0.01	0.696±0.001

Table 6.8 The effect of nanodiamond on the diffusion coefficient of long/short chain polymer at 600 K (unit: $10^{-9} m^2/s$)

	Short chain	Long chain
Pure	1.7054	0.51055
w/o bonds	0.68576	0.47877
w/ bonds	0.11208	0.45670

CHAPTER 6. ELASTIC PROPERTIES OF POLYETHYLENE-NANODIAMOND COMPOSITES

6.1 INTRODUCTION

The addition of micrometer-size fillers to polymer matrices to form polymer composites typically improves their mechanical properties in the form of increased modulus, yield strength, and glass temperature[1, 2]. However, these improvements usually are accompanied by decreased ductility and toughness. In addition, a large amount of filler is often required to achieve the desired properties. Polymer nanocomposites have been shown to provide a unique combination of mechanical and thermal properties, often at very low filler weight fractions. Adding a few weight percent of nanoparticles into polymer matrix materials has the observed effect of improved mechanical properties, decreased permeability, increased electrical conductivity and heat distortion temperature, improved chemical resistance, and increased optical clarity, while preserving many advantages of the host polymer systems, such as low density and high processability[3-10]. For example, Shenderova et al. found improvements in thermal stability, thermal conductivity, and adhesion of the composites with 1-2% mass of nanodiamond particles in polyimide matrix[11]. Sumita et al. achieved dramatic improvements in the yield stress (30%) and Young's modulus (170%) in nanofilled polypropylene compared to micrometer-filled polypropylene[7]. Dolmatov filled the rubber with 2-4% mass detonation diamond and reported 1.35-1.7 times higher stress at 300 % elongation, 1.5 times the rebound elasticity,

twice the cohesive strength, and 30% lower maximum degree of swelling of isoprene rubbers in toluene[5]. Fielder et al. found a significant increase (45%) in the fracture toughness by adding only 0.3% of double walled carbon nanotube in epoxy[10]. Furthermore, the nanocomposites showed no reduction in transparency even at these relatively high loadings, unlike the micrometer-size filled systems. Such polymer nanocomposites are ideal candidate materials in many applications, including aerospace applications, automobile manufacturing, medical devices, and sporting goods.

The influence of nano-scale filler on elastic properties is, however, somewhat amazing, because it is not seen in traditional composite materials. It is not possible to explain this effect with the methods usually applied to analyze traditional composites, such as continuum mechanics[12-14]. Large efforts have been put forth to investigate the corrections between nanofiller and mechanical properties. Cho et al.[15] studied the effect of particle size on mechanical properties. They varied the particle size from the macro- (0.5 mm) to nanometer scale (15 nm) and found the particle size at the macroscale size has little influence on the Young's modulus of the composite, while the Young's modulus increases with decreasing particle size at the nanometer scale. The same results were observed by Chisholm et al.[16], who investigated the matrix properties by infusing micro- and nanosized SiC fillers into an epoxy matrix and found superior thermal and mechanical properties were attained in nanocomposites. Meanwhile, reports are also available which demonstrate that a decreasing nano-filler size has no effect[17], or even negative effects[18] on thermal and mechanical properties. It was reported that the reinforcing efficiency of nanoparticles heavily relates to

dispersion, interface adhesion, and particle aspect ratio[19]. The exact mechanism that could explain how the filler influences the elastic properties is still not identified. This is partly because of challenges in processing nanocomposites, and the unavailability of sophisticated tools to inspect closely their *in situ* manufacturing characterization processes. In this regard, several researchers have performed molecular dynamics simulations, which allow for parametric studies of the influence of nano-filler on the elastic properties of nanocomposites, to visualize the deep insight of mechanics of nanocomposites[9, 20-22]. However, the mechanism is yet to be addressed.

Nanodiamond, which usually has a polyhedral surface, is another attractive filler to fabricate advanced materials because of its extreme hardness and outstanding wear-resistance[23, 24]; however, the research on diamond-filled polymer composites is still very limited[8, 25-29] compared to the huge activities on polymer systems containing dispersed nanoparticles, such as layered silicates and carbon nanotubes. Zhang et al. tested the indentation behavior of synthesized polyimide/diamond nanocomposites and found that both the hardness and modulus of polyimide are steadily enhanced with increasing diamond loading. Though it is promising, the available conclusions based on the simulations on polymer nanocomposites are not yet ready to be applied to nanodiamond-polymer composites, because nanodiamond is a polyhedron. To the best of this author's knowledge, however, the particle shape in these simulations on polymer nanocomposites is usually nanotube, nanoplatelet, or spherical ball. Efforts to examine the reinforcing effort of

polyhedral nanoparticles on the polymer matrix with different chain lengths have not been reported.

In this study, molecular dynamics simulations were used to investigate the effect of octahedral nanodiamond particles on elastic properties of polymer composites. For this, molecular models of nanocomposites were constructed by reinforcing an amorphous polyethylene (PE) matrix with octahedral nanodiamond. Nanodiamonds of about 4 nm were randomly incorporated into polyethylene matrix with different chain length (40 and 200) to form nanocomposites. Molecular models of neat PE matrix were also developed for comparison. Elastic properties of the neat and nanocomposites were then evaluated using two different ensemble approaches, specifically NVT and NPT, with the modified DL_POLY (version 2.19) molecular simulation package, which is adapted to simulate the stretch process and injected with codes to calculate the local stress distribution, from Daresbury Laboratory[30].

6.2 SIMULATION DETAILS AND SAMPLE PREPARATION

In this section, we describe the modeling and implementational aspects of our approaches. First, we give a review on the potentials we used to model our nanocomposite systems and sample preparation. Then, we discuss the approach, NPT, in our studies. Finally, we describe the generation of curves and the computation of elastic moduli and constants.

6.2.1 POTENTIALS

A united-atom is a particle that incorporates a group of atoms, but can approximately

represent the molecular properties of the group on a scale larger than atomic size scale. The united-atom model is a good approximation to simulate molecular systems in which the intermolecular motion is much more important than the intramolecular motion, or the intramolecular motion is much less significant than the intermolecular motion. In our study, a united-atom model is used to describe individual polymer chains, in which each CH₂ or CH₃ group is considered as a single interaction unit to avoid high-frequency vibrations of the C-H bonds without losing the information of chain dynamics, since the intrachain covalent bond potential is, by far, the stiffest interaction in polymers. Individual chains are modeled as sequences of spherical “segments,” as illustrated in Figure 6.1.

The intra-polymer potential by Clarke et al.[31] has been used to describe interactions within a polymer chain. This potential has two components: a valence angle potential and torsion potential. The valence angle potential is described as

$$\Phi(\theta)/J \cdot \text{mol}^{-1} = \frac{1}{2}k_{\theta}(\cos \theta - \cos \theta_0)^2 \quad (6.2.1)$$

where $k_{\theta} = 520\text{J} \cdot \text{mol}^{-1}$, $\theta_0 = 112.813^\circ$, and the torsion potential is described as

$$\Phi(\alpha)/J \cdot \text{mol}^{-1} = C_0 + C_1 \cos \alpha + C_2 \cos^2 \alpha + C_4 \cos^3 \alpha \quad (6.2.2)$$

where $C_0=8832$, $C_1=18087$, $C_3=4880$, and $C_4=-31800$. In general, the C-C bonds in a polymer chain are typically kept rigid to allow large MD times steps during the simulations. However, we have allowed full dynamics of these bonds. A harmonic potential described as

$$\Phi(l)/J \cdot \text{mol}^{-1} = \frac{1}{2} (l - l_0)^2 \quad (6.2.3)$$

is used for the dynamics of C-C bonds within a chain, where $k_b = 346 \text{ J} \cdot \text{mol}^{-1} / \text{\AA}^2$, and $l_0 = 1.53 \text{ \AA}$ [32]. Truncated 6-12 LJ potentials as described in Eqn (6.2.4)

$$\Phi(r_{ij})/J \cdot \text{mol}^{-1} = \begin{cases} 4\varepsilon \left[\left(\frac{\sigma}{r_{ij}} \right)^{12} - \left(\frac{\sigma}{r_{ij}} \right)^6 \right] & \text{for } |r_{ij}| \leq r_{cutoff} \\ 0 & \text{for } |r_{ij}| \geq r_{cutoff} \end{cases} \quad (6.2.4)$$

are applied to pairs of units that are apart by more than three units with $\varepsilon_{CH_2-CH_2} = 0.498 \text{ KJ} \cdot \text{mol}^{-1}$ and $\sigma_{CH_2-CH_2} = 3.95 \text{ \AA}$. The interactions of the carbons within octahedral diamond particles are described with harmonic bond potential as in Eqn (6.2.3) with $k_l = 2848.879 \text{ KJ} \cdot \text{mol}^{-1}$, and $l_0 = 1.53 \text{ \AA}$, and harmonic angle potential as described in Eqn (6.2.1) with $k_\theta = 250.8 \text{ KJ} \cdot \text{mol}^{-1}$ and $\theta_0 = 109.4^\circ$. Truncated 6-12 LJ potentials are also applied to pairs of units that are apart by more than three units with $\varepsilon_{C-C} = 0.4255 \text{ KJ} \cdot \text{mol}^{-1}$ and $\sigma_{C-C} = 3.37 \text{ \AA}$.

For the bond connection between polymer chains and nanodiamond particles, the harmonic potential is used whose parameters are derived using the Lorentz-Berthelot mixing rules [33]

$$k_l^H = [k_l^P \cdot k_l^C]^{\frac{1}{2}} \quad (6.2.5)$$

$$l_0^H = \frac{1}{2} (l_0^P + l_0^C) \quad (6.2.6)$$

where k_l^P and l_0^P are the harmonic bond potential parameters for polymer and k_l^C and l_0^C are

the harmonic bond potential parameters for carbon nanodiamond. For the long distance interaction between the united atoms of polymer chain and the carbon atoms of nanodiamond, the Lorentz-Berthelot mixing rules[33] are again applied as

$$\sigma_{C-CH_2} = \frac{1}{2}[\sigma_{C-C} + \sigma_{CH_2-CH_2}] \quad (6.2.7)$$

$$\varepsilon_{C-CH_2} = [\varepsilon_{C-C} + \varepsilon_{CH_2-CH_2}]^{\frac{1}{2}} \quad (6.2.8)$$

For the composite systems, we have embedded 6 nano-diamond particles in the polyethylene matrix because of their potential promising reinforcement and/or toughening characteristics for the polymers. The cutoff radius $r_{cutoff}=12 \text{ \AA}$ is used in our simulation. The functional forms and parameters of the field are summarized in Table 6.1.

6.2.2 SAMPLE PREPARATION

Molecular models of nanocomposites were developed by randomly placing octahedral nanodiamonds in the neat PE matrix with the method described in Chapter 4. Three sample groups, namely 14 NDs and 97x200 polyethylenes, 14 NDs and 97x40 polyethylenes, and 5 NDs and 1440x40 polyethylenes, were prepared. Each sample group included three structures, neat polymer matrix (NP), nanocomposites without crosslinks between NDs and polymer chains, and nanocomposites with crosslinks between NDs and polymer chains. All the samples were prepared and equilibrated at 600 K and 1 bar, then cooled down within an NPT ensemble at a cooling rate $dT_{ext}/dt = -0.1K/ps$ to the desired temperature, which is 100 K and 300 K for the sample group with 14 NDs, and 300 K for the

sample group with 5 NDs. The samples were further equilibrated within canonical (constant-NVT) and microcanonical (constant-NVE) ensembles for 1 ns each. Further, the samples were adjusted to minimize the initial stress using isothermal-isobaric (constant-NPT) ensemble for 1 ns, and then equilibrated by NVE for another 1 ns. At the end of these steps, the molecular structures were believed to be relaxed at the desired temperature with minimum initial stress. The characteristic features of the polymer chains are summarized in Table 6.2, where the first row represents the name of the sample group. Snapshots of the initial structures are illustrated in Figure 6.2. Detailed descriptions of the ensembles referred above can be found in the DL_POLY manual[30].

6.2.3 SIMULATION DETAILS

The MD simulations were performed using the DL_POLY (version 2.19) simulation package obtained from Daresbury Laboratory[30]. The simulations were carried out at a temperature of 300 K or 100 K with 1 fs time steps. To eliminate the surface effects, periodical boundary conditions were used during the simulations. The elastic properties of neat polymer and nanocomposites were evaluated using an NPT ensemble in our study.

In the NPT approach, the applied external stress is considered as a control variable that produces a change in the strain, the response to which is the measured tension. In other words, both the strain and the tension in our study are dependent variables. This method is preferable to direct control of the strain (like NVE approach) since there is no way to predict

how the shape of the system will respond to the change of the external applied tension. The complete stretch process is:

1. Equilibrate the initial structure at a desired temperature for 1 ns within the NPT ensemble.
2. Gradually stretch the sample along the required direction, as shown schematically in Figure 6.3, using an NPT ensemble by applied external tension at a rate 1 bar /ps (equilibration run).
3. Measure the internal tension with 100 ps NPT run if the decrease of external tension reaches 0.2 kbar (production run).
4. Continue step 2 until the structure breaks down.

The definition of internal stress is, however, different from a continuum mechanics framework. According the manual of DL_POLY[30], the stress at atomic level is defined in the form of *virial stress* as

$$\sigma_{ij} = -\frac{1}{V} \sum_{\alpha} \left(m^{\alpha} v_i^{\alpha} v_j^{\alpha} + \frac{1}{2} \sum_{\alpha \neq \beta} F_i^{\alpha\beta} r_j^{\alpha\beta} \right) \quad (6.2.9)$$

where V is the volume of MD unit cell and $V = \sum_{\alpha} V^{\alpha}$, V^{α} is the atomic volume of atom α ; v_i^{α} is the i -component of the velocity of atom α , $F_i^{\alpha\beta}$ is the i -component of the force between atom α and atom β , and $r_j^{\alpha\beta}$ is the j -component of the separation distance between atom α and atom β . It can be seen that Eq. (1.2.9) represents average atomic stress for the volume of the periodic box. Here, the first term is related to the contribution from kinetic

energy due to the thermal vibration, and the second term is associated with the change in potential energy due to applied deformation. The negative sign is used to express tensile stress as a positive quantity (in MD, compression is generally expressed as positive).

6.3 LINEAR ELASTIC STRESS-STRAIN RELATION

In the NPT approach, the elasticity tensor was deduced from the generalized Hook's law[34]

$$\pi_{\alpha\beta} = \sum_{\gamma\delta} C_{\alpha\beta\gamma\delta} \varepsilon_{\gamma\delta}, \quad \alpha, \beta \in 1, 2, 3 \quad (6.2.10)$$

Here, we assume that $\pi_{\alpha\beta}$ are homogeneous linear functions of $\varepsilon_{\gamma\delta}$ and vice versa, and that C is a positive-definite fourth-order tensor which has major symmetry $C_{\alpha\beta\gamma\delta} = C_{\gamma\delta\alpha\beta}$. For most solid materials, such relations hold until the stress reaches the so-called proportional limit. If the stresses exceeds this limit, the deformation becomes nonlinear but the elastic behavior of the material continues until the stresses reach the so-called elastic limit. The general fourth-order tensor C has $3^4 = 81$ independent constants $C_{\alpha\beta\gamma\delta}$. But since π and ε are symmetric second-order tensors, the number of independent elastic moduli reduces to $6 \times 6 = 36$. Because of major symmetry it further reduces to $6(6 + 1)/2 = 21$. Then, we can write the stress-strain relation in Eqn (6.2.10) in matrix form

$$\begin{bmatrix} \pi_{11} \\ \pi_{22} \\ \pi_{33} \\ \pi_{12} \\ \pi_{13} \\ \pi_{23} \end{bmatrix} = \begin{bmatrix} C_{1111} & C_{1122} & C_{1133} & C_{1112} & C_{1113} & C_{1123} \\ C_{1122} & C_{2222} & C_{2233} & C_{2212} & C_{2213} & C_{2223} \\ C_{1133} & C_{2233} & C_{3333} & C_{3312} & C_{3313} & C_{3323} \\ C_{1112} & C_{2212} & C_{3312} & C_{1212} & C_{1213} & C_{1223} \\ C_{1113} & C_{2213} & C_{3313} & C_{1213} & C_{1313} & C_{1323} \\ C_{1123} & C_{2223} & C_{3323} & C_{1323} & C_{1323} & C_{2323} \end{bmatrix} \begin{bmatrix} \varepsilon_{11} \\ \varepsilon_{22} \\ \varepsilon_{33} \\ 2\varepsilon_{12} \\ 2\varepsilon_{13} \\ 2\varepsilon_{23} \end{bmatrix} \quad (6.2.11)$$

We can invert the stress-strain relations (Eqn (6.2.11)) by inverting the symmetric 6×6 elastic constant matrix C . This results in

$$\begin{bmatrix} \varepsilon_{11} \\ \varepsilon_{22} \\ \varepsilon_{33} \\ 2\varepsilon_{12} \\ 2\varepsilon_{13} \\ 2\varepsilon_{23} \end{bmatrix} = \begin{bmatrix} S_{1111} & S_{1122} & S_{1133} & S_{1112} & S_{1113} & S_{1123} \\ S_{1122} & S_{2222} & S_{2233} & S_{2212} & S_{2213} & S_{2223} \\ S_{1133} & S_{2233} & S_{3333} & S_{3312} & S_{3313} & S_{3323} \\ S_{1112} & S_{2212} & S_{3312} & S_{1212} & S_{1213} & S_{1223} \\ S_{1113} & S_{2213} & S_{3313} & S_{1213} & S_{1313} & S_{1323} \\ S_{1123} & S_{2223} & S_{3323} & S_{1323} & S_{1323} & S_{2323} \end{bmatrix} \begin{bmatrix} \pi_{11} \\ \pi_{22} \\ \pi_{33} \\ \pi_{12} \\ \pi_{13} \\ \pi_{23} \end{bmatrix} \quad (6.2.12)$$

where S is the compliance matrix. Suppose now that only one of the six independent components of the induced stress is nonzero, say $\pi_{\alpha\beta}$. Then the components

$$\begin{aligned} S_{11\alpha\beta} &= \frac{\varepsilon_{11}}{\pi_{\alpha\beta}}, & S_{22\alpha\beta} &= \frac{\varepsilon_{22}}{\pi_{\alpha\beta}}, & S_{33\alpha\beta} &= \frac{\varepsilon_{33}}{\pi_{\alpha\beta}}, \\ S_{12\alpha\beta} &= \frac{2\varepsilon_{12}}{\pi_{\alpha\beta}}, & S_{13\alpha\beta} &= \frac{2\varepsilon_{13}}{\pi_{\alpha\beta}}, & S_{23\alpha\beta} &= \frac{2\varepsilon_{23}}{\pi_{\alpha\beta}}, \end{aligned} \quad (6.2.13)$$

can be determined by calculating the slopes of the corresponding stress-strain curves. Then, we can subsequently determine the components $C_{\alpha\beta\gamma\delta}$ by inverting the $S_{\alpha\beta\gamma\delta}$.

There is a special elastic constant, the Young's modulus, E . If the stretching force is only applied in the uniaxial direction, for example, in longitudinal direction, the constant $E_{11} := \pi_{11}/\varepsilon_{11} = 1/S_{1111}$ represents the ratio of the longitudinal stress to the corresponding longitudinal strain. In other words, it is the slope of the stress-strain curve under uniaxial tension. Furthermore, the ratio of transverse contraction strain to longitudinal extension strain in the direction of the stretching force is known as the Poisson ratio, $\nu := -\varepsilon_{ii}/\varepsilon_{11}$, ($i \in 2, 3$).

The primary information that results from these tension experiments is the response of the h matrix, defining the size and shape of the primary cell, and that of the internal

pressure tensor, σ . These together enable us to evaluate the stress versus strain behavior in our simulation under NPT conditions. In general, the small system size usually means a relatively complex and fluctuating response of the shape and dimensions of the system to the applied tension. In our study, we use the average length of the primary cell l along the direction of applied tensor during a production run, and the cross-sectional area, A , perpendicular to it. From A , an effective width, W can also be defined

$$W = A^{1/2} \quad (6.2.14)$$

Using l and W , the effect of the applied tension can be resolved into the nominal strains parallel and perpendicular to the direction of applied tension as would happen in the

$$\text{lab} \quad \varepsilon_L = \frac{L - L_0}{L_0} \quad (6.2.15)$$

$$\varepsilon_W = \frac{W - W_0}{W_0} \quad (6.2.16)$$

Here the zero subscript denotes the equilibrium value and is defined in this case as the average over a time interval of about 200 ps just prior to the application of tension. In this way, the Poisson ratio is interpreted as

$$v := -\varepsilon_W / \varepsilon_L \quad (6.2.17)$$

For both approaches, the local stress tensor experienced by surrounding atoms was calculated during the production run. The calculation is based on an unpublished paper by Michael Falk[35]. The local stress is defined as

$$\sigma_{ij}(R, t) = \sum_{\alpha} \left\{ -m^{\alpha} v_i^{\alpha} v_j^{\alpha} \delta(R - r^{\alpha}) + \frac{1}{2} \sum_{\alpha \neq \beta} r_i^{\alpha\beta} F_j^{\alpha\beta} \int_0^1 d\lambda \delta(R - r_{\beta} - \lambda r_{\alpha\beta}) \right\} + \sigma_{ij}^0 \quad (6.2.18)$$

where R is the contribution region, m^{α} is the mass of atom α , r^{α} denotes the position of the i^{th} atom, $r_i^{\alpha\beta}$ represents the i -component of the vector between atoms α and β , while $F_j^{\alpha\beta}$ is the j -component of the force between atoms α and β , $\delta(x)$ is a Dirichlet function, the term σ_{ij}^0 is an integration constant which is defined to insure that the expression is translationally and rotationally invariant. In the Eq. (1.2.18), the first term represents the kinetic contribution, and the second term describes the potential contribution where there is an integral over bonds which can be written as

$$B(r^{\alpha}, r^{\beta}, R) \equiv \int_0^1 d\lambda \delta(R - r_{\beta} - \lambda r_{\alpha\beta}) \quad (6.2.19)$$

where we call B the bond function. In our simulation, the bond functions are counted to the extent they cross the area of interest as illustrated in Figure 6.4.

After the forgoing procedures, polymer densities for all models were calculated using the building statistics function in DL_POLY. The radial distribution function (RDF) $g(r)$ was also calculated for all non-bonded VDW atom pairs which comprise atoms that contribute to non-bonded energy. These $g(r)$ functions were then utilized to estimate VDW separation distance or gap (h) between polymer and embedded nanodiamond for all nanocomposite models.

6.4 RESULTS AND DISCUSSIONS

Some linear elastic stress-strain relations of the neat PE and ND-reinforced nanocomposites obtained from the MD simulation are presented in Figs 6.5- 6.7. The calculated Young's moduli of the four sample groups are shown in Table 6.3 to Table 6.6, respectively, determined using the molecular modeling procedure discussed in previous sections. It is seen from the Table 6.3 and Table 6.4 that the Young's modulus of neat polymer increases with the increasing polymer chain length when the test temperature is constant. In view of the density, the commercially available linear low density polyethylene (LLDPE) closely matches our simulated amorphous polyethylene. The reported elastic modulus of LLDPE lies between 262 and 896 MPa[36], values close to our results. The difference may be due to the structures and that the polyethylene chain length doesn't match that for LLDPE.

Table 6.3-Table 6.6 shows the Young's modulus and fracture strength for the four sample groups studied. The fracture strength in the tables is defined by the maximum strength before the simulation failure. It is clear that the presence of the ND improved the Young's modulus of nanocomposites composed of short chain polyethylene. It also improved the Young's modulus of the composite system with long chains when its density was low; however, it adversely affected the elastic properties if its density was high. This agrees with simulation results by Gersappe[37], who employed a MD simulation to probe the molecular mechanisms by which nanofillers reinforce a polymer matrix, and found that the ability of nanofillers to increase the toughness of the material results from equivalent time scale in

movement of nanofiller and polymer chain, since it leads to the equivalence of size scales of the polymer and the filler. The radius of gyration for the samples in our study at 1 bar is listed in Table 6.8. The presence of crosslinks increased the fracture strength of the nanocomposite system, because covalent bonds at the interface slow down the separation of these two phases. It is also interesting to note that the presence of crosslinks did enhance the elastic properties of all four composite systems, and this effect increases with increasing number of crosslinks. This observation is consistent with recent MD simulations by Frankland[9], who simulated nanotube-polymer system reinforced by covalently bonding between nanotube and polymer matrix, and found Young's modulus to be increased by over an order of magnitude even with relatively low density of chemical bonds. Furthermore, both Young's modulus and yield stress decrease with increasing temperature for the same system as the materials become more solid-like at the lower temperature.

It is natural for the density of a composite to be higher than the density for a pure polymer system, because the inclusions usually have much higher density than the polymer. This was found to be true with the systems in our study, as shown in Table 6.2. The density increased, as expected, as the filler content increased. However, the effect of fillers on the density of the polymer matrix is different.

In Table 6.7, the densities of polyethylene in neat polymer and the nanocomposite systems are listed. It can be seen that the density of long chain polyethylene is larger than that of short chain polyethylene for more percentage of free volume in short chain polyethylene, as analyzed in the previous chapter. It is also interesting to note that the density

of polyethylene in nanocomposites without crosslinks is somewhat less than in nanocomposites with crosslinks, and both are less than their neat counterpart. A decreasing trend in bulk density is also observed with increasing nano-filler density. It can be concluded from this observation that the number of NDs and crosslinks in composites has considerable influence on polymer density. The effect can be well understood from the radial density distribution of PE for both neat and nanocomposites, as shown in Figure 6.8, in which the distribution is constructed by measuring local densities of PE at various radial distances starting from the center of ND to half-length of the periodic box, with a step of 1.0 angstrom. The density is especially low at a distance close to the nanoparticle, though the distribution fluctuates in a similar manner as in the neat polymer, and has a similar density profile in the composite. The collective contributions of these two factors yielded the low density in the nanocomposites. The discernible contribution from the crosslinks can be realized from the radial distribution plot as showed in Figure 6.9.

It is known that the radial distribution function is a measurement of the distribution of corresponding atom pairs in three-dimensional space due to VDW interactions[38]. Hence , $g(r)_{C-PE}$ refers to the radial distribution of PE atoms with respect to carbon atoms in NDs, and a plot of $g(r)_{C-PE}$ would provide information about the polymer distribution due to interaction with NDs. Figure 6.10 reveals that the crosslinks have a strong influence on the $g(r)$ plot. This figure shows that more atoms are tending to disseminate across the polymer-nanoparticle interface due to the crosslinks at the interface, and this effect increases with increasing crosslinks.

Figure 6.11 shows the local stress experienced by each atom and the local stress distribution of $\bar{\sigma}_{11}$ with respect to the distance r from the center of NDS for the system with 14 NDs and 40 polyethylene chains (200 united atoms per chain), namely SG-IV. It is clear that the NDs experience more stress than polymer chains. More detailed analysis showed that the stress in the immediate vicinity of the NDs is more negative than those away from NDs. Away from NDs, the local stress becomes equal to the external stress. These also show that the density near a particle is lower than bulk density.

6.5 SUMMARY

MD stress-strain simulations for four group samples indicated that the effect of nanofillers on Young's modulus depends on the size of polyethylene chains. However, the presence of crosslinks increased the fracture strength of nanocomposites. The addition of nanoparticles increases the system density; however, it doesn't necessarily increase the density of the polymer matrix. In our study, the presence of nanoparticles decreases the polymer density near the surface, and becomes equal to the bulk density away from the nanoparticle. The local stress analysis showed that the nanoparticle and the atoms near the ND surface experienced more stress than those away from the center of the nanoparticles, which, on the other hand, also demonstrated that the density near surface is low.

6.6 REFERENCES

1. Sumita, M., et al., *TENSILE YIELD STRESS OF POLYPROPYLENE COMPOSITES FILLED WITH ULTRAFINE PARTICLES*. Journal of Materials Science, 1983. **18**(6): p. 1758-1764.
2. Hussain, M., et al., *Fracture behavior and fracture toughness of particulate filled epoxy composites*. Materials Letters, 1996. **27**(1-2): p. 21-25.
3. Rong, M.Z., et al., *Improvement of tensile properties of nano-SiO₂/PP composites in relation to percolation mechanism*. Polymer, 2001. **42**(7): p. 3301-3304.
4. Dolmatov, V.Y., *Polymer-diamond composites from detonation-derived nanodiamonds. Part 1*. Sverkhverdye Materialy, 2007. **1**: p. 15.
5. Dolmatov, V.Y., *Polymer-diamond composites based on detonation nanodiamonds. Part 2*. Sverkhverdye Materialy, 2007. **2**: p. 15.
6. Dolmatov, V.Y., *Polymer-diamond composites based on detonation nanodiamonds. Report 3*. Sverkhverdye Materialy, 2007. **4**: p. 10.
7. Sumita, M., et al., *DYNAMIC MECHANICAL-PROPERTIES OF POLYPROPYLENE COMPOSITES FILLED WITH ULTRAFINE PARTICLES*. Journal of applied polymer science, 1984. **29**(5): p. 1523-1530.
8. Shenderova, O., et al., *Nanodiamond and onion-like carbon polymer nanocomposites*. Diamond and Related Materials, 2007. **16**(4-7): p. 1213-1217.
9. Frankland, S.J.V., et al., *The stress-strain behavior of polymer-nanotube composites from molecular dynamics simulation*. Composites Science and Technology, 2003. **63**(11): p. 1655-1661.
10. Fiedler, B., et al., *Fundamental aspects of nano-reinforced composites*. Composites Science and Technology, 2006. **66**(16): p. 3115-3125.
11. Shenderova, O., et al., *Detonation nanodiamond and onion-like carbon: applications in composites*. Physica Status Solidi a-Applications and Materials Science, 2008. **205**(9): p. 2245-2251.
12. Benveniste, Y., *A NEW APPROACH TO THE APPLICATION OF MORI-TANAKA THEORY IN COMPOSITE-MATERIALS*. Mechanics of Materials, 1987. **6**(2): p. 147-157.

13. Mori, T. and K. Tanaka, *AVERAGE STRESS IN MATRIX AND AVERAGE ELASTIC ENERGY OF MATERIALS WITH MISFITTING INCLUSIONS*. Acta Metallurgica, 1973. **21**(5): p. 571-574.
14. Eshelby, J.D., *THE DETERMINATION OF THE ELASTIC FIELD OF AN ELLIPSOIDAL INCLUSION, AND RELATED PROBLEMS*. Proceedings of the Royal Society of London Series a-Mathematical and Physical Sciences, 1957. **241**(1226): p. 376-396.
15. Cho, J., M.S. Joshi, and C.T. Sun, *Effect of inclusion size on mechanical properties of polymeric composites with micro and nano particles*. Composites Science and Technology, 2006. **66**(13): p. 1941-1952.
16. Chisholm, N., et al., *Fabrication and mechanical characterization of carbon/SiC-epoxy nanocomposites*. Composite Structures, 2005. **67**(1): p. 115-124.
17. Reynaud, E., et al., *Nanofillers in polymeric matrix: a study on silica reinforced PA6*. Polymer, 2001. **42**(21): p. 8759-8768.
18. Jiang, L., et al., *Strengthening acrylonitrile-butadiene-styrene (ABS) with nano-sized and micron-sized calcium carbonate*. Polymer, 2005. **46**(1): p. 243-252.
19. Buryachenko, V.A., et al., *Multi-scale mechanics of nanocomposites including interface: Experimental and numerical investigation*. Composites Science and Technology, 2005. **65**(15-16): p. 2435-2465.
20. Smith, J.S., D. Bedrov, and G.D. Smith, *A molecular dynamics simulation study of nanoparticle interactions in a model polymer-nanoparticle composite*. Composites Science and Technology, 2003. **63**(11): p. 1599-1605.
21. Odegard, G.M., et al., *Constitutive modeling of nanotube-reinforced polymer composites*. Composites Science and Technology, 2003. **63**(11): p. 1671-1687.
22. Vacatello, M., *Monte Carlo simulations of polymer melts filled with solid nanoparticles*. Macromolecules, 2001. **34**(6): p. 1946-1952.
23. *Synthesis, Properties And Applications of Ultrananocrystalline Diamond*. 2005: Kluwer Academic Pub.
24. Barnard, A.S., S.P. Russo, and I.K. Snook, *First Principles Investigations of Diamond Ultrananocrystals*. International Journal of Modern Physics B: Condensed Matter Physics; Statistical Physics; Applied Physics, 2003. **17**(21): p. 3865.

25. Zhang, Q., et al., *Polyimide/Diamond nanocomposites: Microstructure and indentation Behavior*. Macromolecular Rapid Communications, 2007. **28**(21): p. 2069-2073.
26. d'Almeida, J.R.M., et al., *Diamond-epoxy composites*. Journal of Reinforced Plastics and Composites, 2007. **26**(3): p. 321-330.
27. Dolmatov, V., *Polymer—diamond composites based on detonation nanodiamonds. Part 3*. Journal of Superhard Materials, 2007. **29**(4): p. 199-205.
28. Dolmatov, V., *Polymer-diamond composites based on detonation nanodiamonds. Part 1*. Journal of Superhard Materials, 2007. **29**(1): p. 1-11.
29. Dolmatov, V., *Polymer-diamond composites based on detonation nanodiamonds. Part 2*. Journal of Superhard Materials, 2007. **29**(2): p. 65-75.
30. Smith, W. and T.R. Forester, *The DL_POLY_2 USER MANUAL*. 2008.
31. Brown, D., et al., *THE PREPARATION OF POLYMER MELT SAMPLES FOR COMPUTER-SIMULATION STUDIES*. Journal of Chemical Physics, 1994. **100**(8): p. 6011-6018.
32. Rigby, D. and R.J. Roe, *MOLECULAR-DYNAMICS SIMULATION OF POLYMER LIQUID AND GLASS .I. GLASS-TRANSITION*. Journal of Chemical Physics, 1987. **87**(12): p. 7285-7292.
33. M. P. Allen, D.J.T., *Computer Simulations of Liquids*. 1987: Clarendon Press: Oxford.
34. Chandrasekharaiah, D.S., *Continuum mechanics*, ed. L. Debnath. 1994, Academic Press: Boston .:
35. Falk, M., *Local Stress Calculation in Molecular Dynamics*. 1999, Harvard University: Cambridge. p. 8.
36. Peacock, A., *Handbook of Polyethylene Structures: Properties, and Applications*. 2000: Routledge.
37. Gersappe, D., *Molecular mechanisms of failure in polymer nanocomposites*. Physical Review Letters, 2002. **89**(5): p. 4.
38. Allen, M.P. and D.J. Tildesley, *Computer simulation of liquids*. Oxford science publications. 1989, Oxford England; New York: Clarendon Press; Oxford University Press. 385.

FIGURES

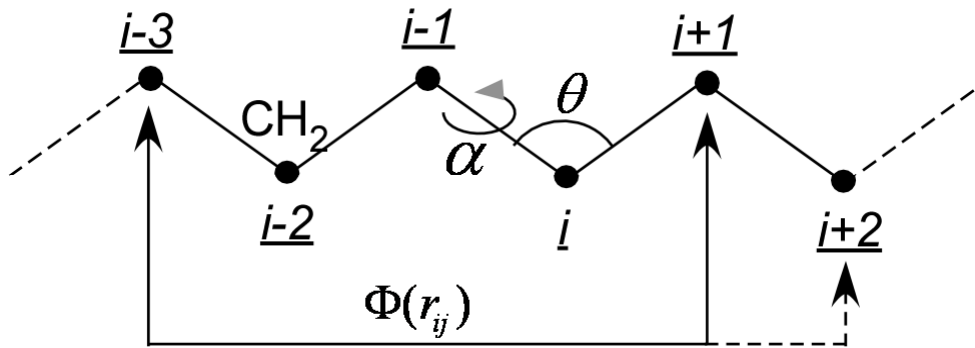


Figure 6.1 Individual chain model. The spherical “segment” simulates a CH_2 or CH_3 unit. A harmonic force constrains the bond length l around the equilibrium length l_0 . The bond angle θ is likewise constrained around the tetrahedral angle. The torsional angle ϕ , given by the angle between the plane containing segments $i-2$, $i-1$ and i and that containing segments $i-1$, i , and $i+1$, is subject to a threefold potential having *trans* and *gauche* minima. Segments separated by more than three bonds along the chain (for example $i-3$ and $i+1$), as well as segments which belong to different chains, interact according to a truncated Lennard-Jones potential.

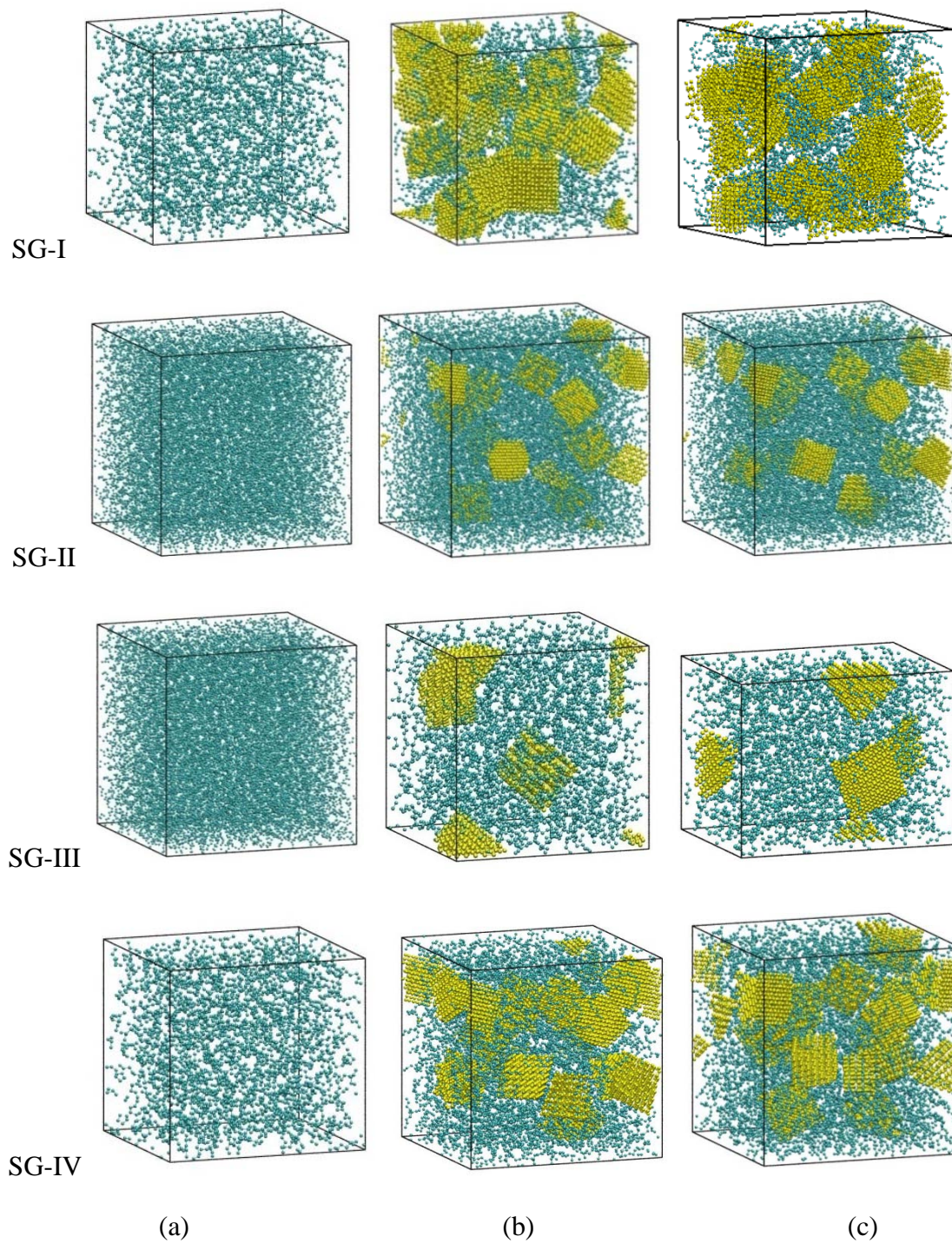


Figure 6.2 Periodic box of different neat and nanocomposite models (see Table 6.2) used in the simulations. Note the size of the box obtained after complete equilibration. (a) neat polyethylene; (b) composites w/o chemical bonds; (c) composites w/ chemical bonds.

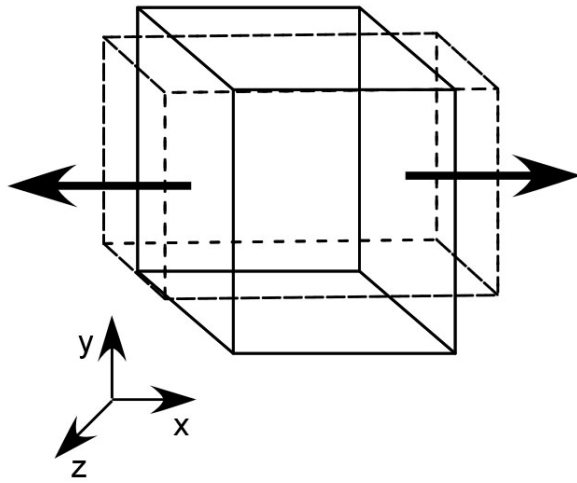


Figure 6.3 Schematic diagram of deformed (dashed line) and un-deformed (solid line) shape of the unit showing unidirectional tension (NST approach).

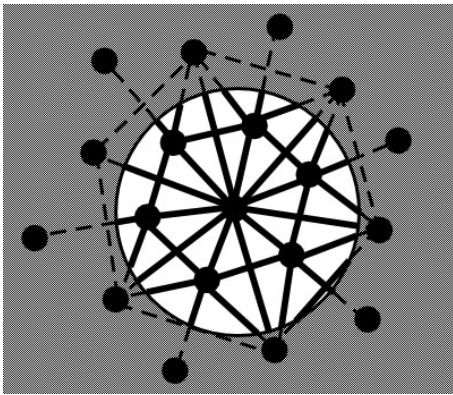


Figure 6.4 In the full expression, the bonds are counted to the extent that they cross the area of interest. Dark segments of bonds contribute; dotted segments do not.

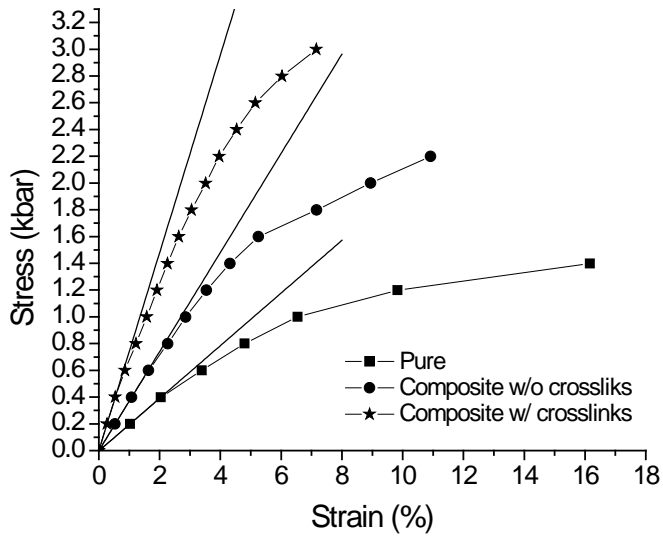


Figure 6.5 Measured tension ($-\sigma_{x,x}$) as a function of percentage extension $\gamma_L \times 100$ for tension applied at 1 bar/ps under 100 K for the sample group containing 14 NDs and 97x40 polyethylene.

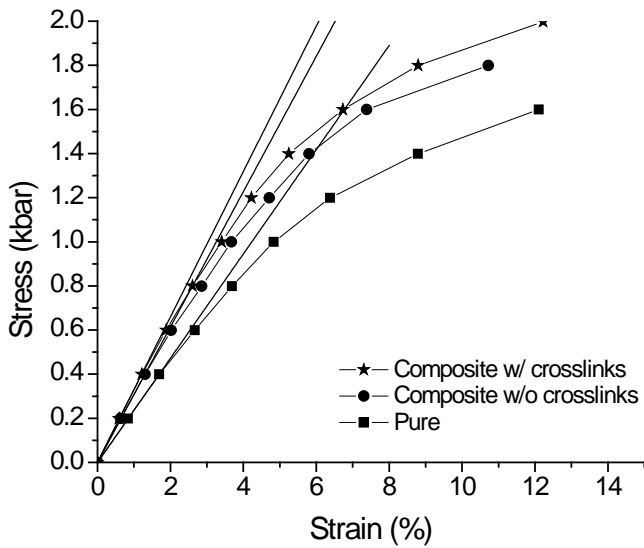


Figure 6.6 Measured tension ($-\sigma_{x,x}$) as a function of percentage extension $\gamma_L \times 100$ for tension applied at 1 bar/ps under 100 K for the sample group containing 14 NDs and 97x200 polyethylene.

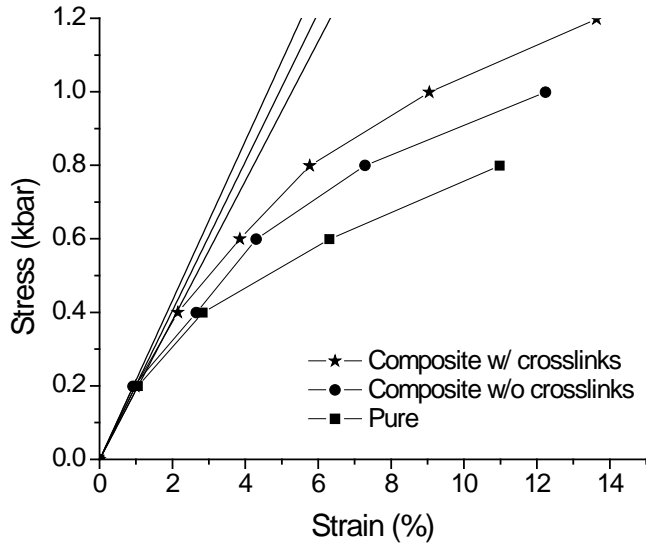


Figure 6.7 Measured tension ($-\sigma_{xx}$) as a function of percentage extension $\gamma_L \times 100$ for tension applied at 1 bar/ps under 300 K for the sample group containing 14 NDs and 97x200 polyethylene.

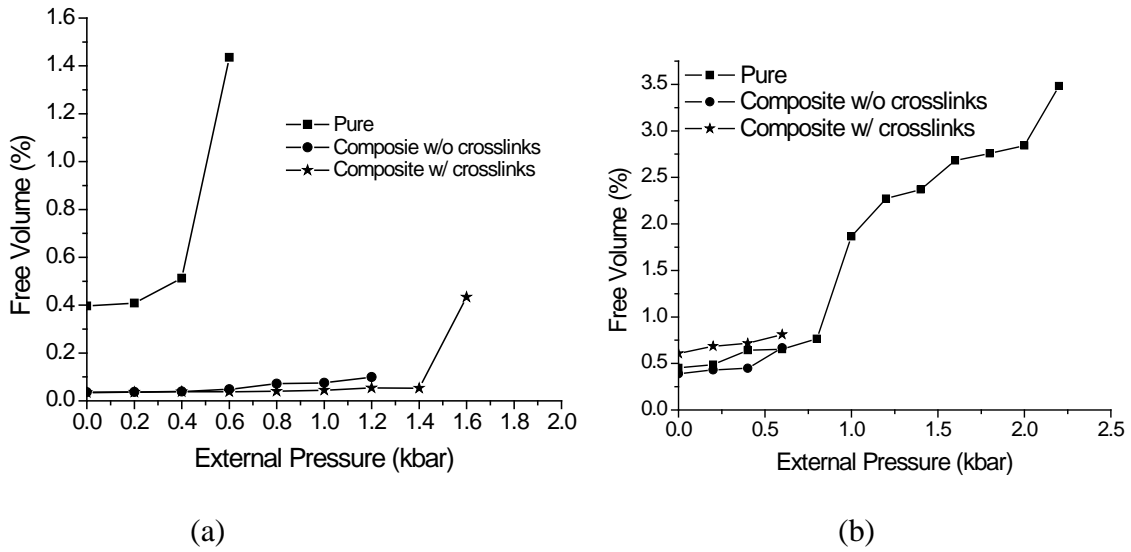
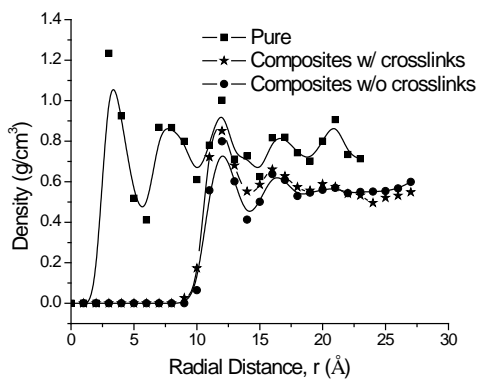
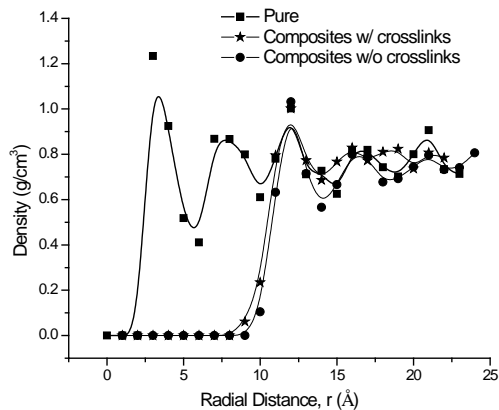


Figure 6.8 Free volume vs. external pressure for (a) SG-I and (b) SG-II at 300 K.

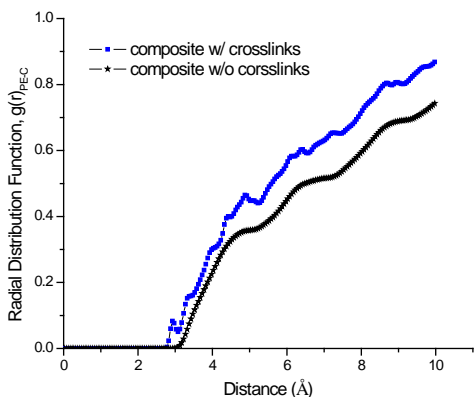


(a)

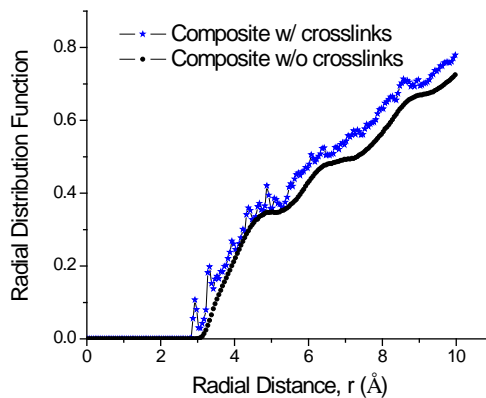


(b)

Figure 6.9 Radial density distribution of various for (a) SG-I and (b) SG-III at 300 K and atmospheric pressure.



(a)



(b)

Figure 6.10 PE-C radial distribution function (RDF) of (a) SG-I and (b) SG-III at 300 K and atmospheric pressure.

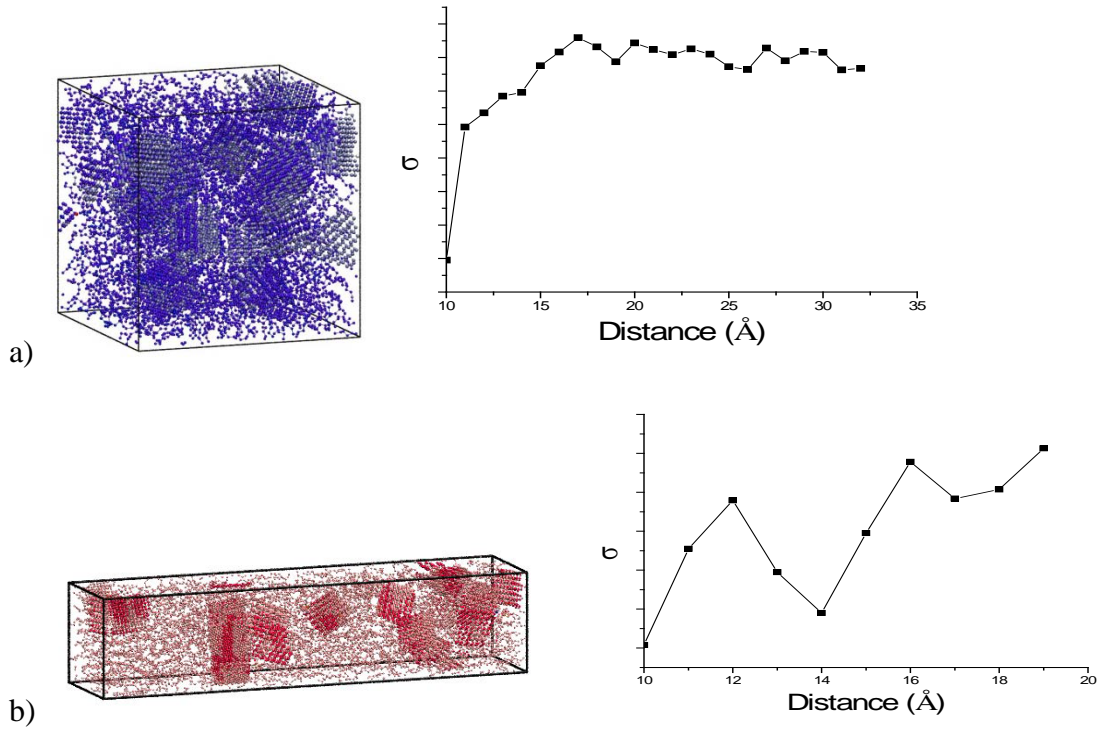


Figure 6.11 The distribution of the local stress (σ_{11}) and the distribution of the local stress $\bar{\sigma}_{11}$ with respect to the distance r from the center of the NDs for the system 14 NDs and 40x200 polyethylene with crosslinks at 300 K and external stress a) 0 and b) 0.2 GPa.

TABLES

Table 6.1 Functional form and parameters for force field model of polyethylene and nano-diamond.

Interaction type	Potential type	Functional form	Parameters
Bond	Harmonic	$U(r) = \frac{1}{2}k_r(r - r_0)^2$	PE-PE
			$k_r = 346.00$ kJ/mole
			$r_0 = 1.53$ Å
Bond	Harmonic	$U(r) = \frac{1}{2}k_r(r - r_0)^2$	ND-ND
			$k_r = 2848.879$ kJ/mole
			$r_0 = 1.53$ Å
Bond	Harmonic	$U(r) = \frac{1}{2}k_r(r - r_0)^2$	ND-PE
			$k_r = 992.83$ kJ/mole
			$r_0 = 1.53$ Å
Angle	Harmonic cosine	$U(\theta) = \frac{1}{2}k_\theta(\cos(\theta) - \cos(\theta_0))^2$	PE-PE
			$k_\theta = 520.0$ kJ/mole
			$\theta = 112.00^\circ$
Angle	Harmonic cosine	$U(\theta) = \frac{1}{2}k_\theta(\cos(\theta) - \cos(\theta_0))^2$	ND-ND
			$k_\theta = 250.8$ kJ/mole
			$\theta = 109.4^\circ$
Dihedral	Clark	$U(\phi) = C_0 + C_1 \cos \phi + C_2 \cos^2 \phi + C_3 \cos^3 \phi$	PE-PE
			$C_0 = 8.832$ kJ/mole
			$C_1 = 18.087$ kJ/mole
Dihedral	Clark	$U(\phi) = C_0 + C_1 \cos \phi + C_2 \cos^2 \phi + C_3 \cos^3 \phi$	$C_2 = 4.88$ kJ/mole
			$C_3 = -31.800$ kJ/mole
Non-bond	Lennard-Jones	$U(r) = \begin{cases} 4\varepsilon \left[\left(\frac{\sigma}{r}\right)^{12} - \left(\frac{\sigma}{r}\right)^6 \right] & r < r_{cut} \\ 0 & r \geq r_{cut} \end{cases}$	PE-PE
			$\varepsilon = 0.4980$ kJ/mole
			$\sigma = 3.95$ Å
Non-bond	Lennard-Jones	$U(r) = \begin{cases} 4\varepsilon \left[\left(\frac{\sigma}{r}\right)^{12} - \left(\frac{\sigma}{r}\right)^6 \right] & r < r_{cut} \\ 0 & r \geq r_{cut} \end{cases}$	PE-ND
			$\varepsilon = 0.4610$ kJ/mole
			$\sigma = 3.65$ Å
Non-bond	Lennard-Jones	$U(r) = \begin{cases} 4\varepsilon \left[\left(\frac{\sigma}{r}\right)^{12} - \left(\frac{\sigma}{r}\right)^6 \right] & r < r_{cut} \\ 0 & r \geq r_{cut} \end{cases}$	ND-ND
			$\varepsilon = 0.4255$ kJ/mole
			$\sigma = 3.37$ Å

Table 6.2 Characteristics of polyethylene chains in various nanocomposites and neat systems

	SG-I	SG-II	SG-III	SG-IV
Number of chains in PE	97	97	97	40
Number of UA units	40	200	40	200
Number of NDs	14	14	3	14
ND weight density (%)	58.50	22.00	23.17	40.56
ND volume density (%) at 100K	24.57	6.80	6.85	14.19
Number of crosslinks	87	95	33	36

Table 6.3 The Young's modulus (GPa) for the sample group containing 14 NDs and 97x40 polyethylene (SG-I).

	Pure		Composite w/o Crosslinks		Composites w/ crosslinks	
	Modulus	Fracture	Modulus	Fracture	Modulus	Fracture
100 K	0.197	0.139	0.371	0.22	0.739	0.30
300 K	0.0577	0.06	0.144	0.14	0.308	0.20

Table 6.4 The Young's modulus (GPa) for the sample group containing 14 NDs and 97x200 polyethylene (SG-II).

	Pure		Composite w/o Crosslinks		Composites w/ crosslinks	
	Modulus	Fracture	Modulus	Fracture	Modulus	Fracture
100 K	0.236	0.316	0.307	0.314	0.330	0.580
300 K	0.190	0.240	0.217	0.258	0.203	0.580

Table 6.5 The Young's modulus (GPa) for the sample group containing 3 NDs and 97x40 polyethylene (SG-III).

	Pure	Composite w/o Crosslinks	Composites w/ crosslinks
100 K	0.197	0.228	0.261
300 K	0.0577	0.197	0.246

Table 6.6 The Young's modulus (GPa) for the sample group containing 14 NDs and 40x200 polyethylene (SG-IV).

	Pure	Composite w/o Crosslinks	Composites w/ crosslinks
100 K	0.236	0.177	0.262
300 K	0.190	0.122	0.213

Table 6.7 Bulk densities of polyethylene in neat PE and in nanocomposites (g/cm³).

System	Model	100K	300K
14 NDs and 97x40 polyethylene	PE (CL=40)	0.8652	0.8152
	Nanocomposite w/o bonds	0.7717	0.7440
	Nanocomposite w/ bonds	0.7718	0.7480
14 NDs and 97x200 polyethylene	PE(CL=200)	0.8796	0.8378
	Nanocomposite w/o bonds	0.8592	0.8222
	Nanocomposite w/ bonds	0.8621	0.8267
3 NDs and 97x40 polyethylene	PE (CL=40)	0.8652	0.8152
	Nanocomposite w/o bonds	0.8115	0.7992
	Nanocomposite w/ bonds	0.8311	0.8244
14 NDs and 40x200 polyethylene	PE(CL=200)	0.8796	0.8378
	Nanocomposite w/o bonds	0.8115	0.7907
	Nanocomposite w/ bonds	0.7950	0.7948

Table 6.8 Radius of gyration of polyethylene chains (unit Å)

		Pure	Composite w/o Crosslinks	Composites w/ crosslinks
SG-I	100 K	11.55	11.78	11.90
	300 K	11.60	11.98	11.96
SG-II	100 K	26.95	28.60	28.10
	300 K	27.40	28.98	28.53
SG-III	100 K	11.55	11.53	11.10
	300 K	11.60	11.54	11.65
SG-IV	100 K	26.95	23.15	24.10
	300 K	27.40	23.62	24.00

CHAPTER 7. CONCLUSIONS AND FUTURE WORK

The molecular dynamics simulations using a heat of formation model with the REBO potential were carried out to investigate the size and surface orientation and principal axis dependent thermal stability of several series of nanodiamonds and nanorods. The simulation results showed that the nanodiamonds and nanorods are more energetically stable structures than graphite at nanoscale (about 2 to 5.5 nm). In all but this range, the nanodiamonds and nanorods are metastable. For the nanodiamond with (111) surface, the structure will transform to fullerence-like structure through surface buckification when the diameter decreases to less than 2 nm. For the nanorods with (001) surface, the surface carbon will form dimer to reduce the system energy. The heats of formation for the 6 ND particle clusters and 6 NR clusters with different surface orientation and principal axis by REBO suggested that octahedra is the most stable structure at nanoscale although there may be many more morphologies of nanodiamond and the NDs with the combination of $\langle 001 \rangle$ and (011), $\langle 011 \rangle$ and (111), $\langle 011 \rangle$ and (001)/(111) are the stable structures at nanoscale.

MD simulations were also carried out to investigate the glass transition and elastic properties of the polyethylene and nanodiamond composites. The results on the free volume and conformational state transition showed that the glass transition phenomenon is a second order phase transition associated with the frozen conformational state change under glass transition temperature. The glass transition temperature increases with increasing pressure and nano filler density in short chain polymer composites. The nonbonded LJ potential energy and torsional energy decrease linearly with decreasing temperature both above and

below T_g , with an abrupt change in slope at T_g . The results on elastic properties indicated that the effect of nanoparticles on polymer systems mainly determined by the equivalent time scale movement of nanoparticles and polymer chains, which can be improved by either equivalent size scale nanoparticles or increasing interface interaction. The addition of nanoparticles usually increases the composite density, however, it doesn't necessarily increase the density of polymer matrix.

For the future work, the simulations for different type polymer with different chain length and different size of nanodiamonds or nanorods to form different surface interaction environment, such high VDW interaction, low VDW interaction, neutral VDW interaction and functional groups at ND surface etc since the most important factor affecting the elastic and thermal properties of the composites is the equivalence of time scales of mobility of the polymer and the filler, rather than nanoparticle surface area. However, the equivalence of mobility is mainly determined by the interaction between the filler and the polymer besides the size of the filler particle. We also can expect from our simulation result that the differences between fillers of different size would reduce if the interaction between filler and the polymer increases because the filler are constrained to move along with the polymer matrix in this situation.